MITOCHONDRIAL FUNCTION AND DYNAMICS IN DEMYELINATED AXONS

Fabian Peters

Supervisor: Professor Kenneth J Smith

Submitted for the degree of Doctor of Philosophy in Neuroscience

Department of Neuroinflammation

Institute of Neurology

University College London

June 2017

DISCLAIMER

I, Fabian Peters, confirm that the work presented in this thesis is my own, unless stated otherwise.

Where information has been derived from other sources, I confirm that this has been indicated in the thesis.

During some of the calcium imaging experiments described in chapter 6, I supervised and was assisted by Caroline Casey, who was a first year Welcome Trust PhD candidate at the time.

Signature

Date

ACKNOWLEDGEMENTS

First and foremost, I would like to thank my supervisor, Ken Smith, for his guidance and encouragement from when we first met until long after I had left the lab. Even as it became clear that my path was going to lead me away from academia he was nothing but kind and supportive. I am truly grateful for his help.

I am also thankful to Marija Sajic for kick-starting the project that forms the core of this thesis and teaching me most of what I know about surgery and imaging.

Thank you to all the members of the Smith lab, in particular Alexandra Phillips, Andrew Davies, Claudio Villegas Llerena, Dimitra Schiza, Gregory Delattre, Keila Ida, Kim Chisholm, Mario Amatruda, Radha Desai, and Roshni Desai. Science can be a solitary pursuit at times and it helps to know that you have other players on your team. Thank you also to Charlotte Burt and Sharmeen Haque who helped with all the administrative bits without which nothing would ever get done.

Lastly, I want to thank my family. My mum and dad for being relentless supporters of my ambitions even if it meant that they got to see less of me, and for believing in me even when I didn't. And Nina who still gets me like no one else does and always has the best advice.

Most importantly, I would like to thank Charlotte for being my home, my best friend, and greatest source of strength. Thank you for all that you are.

ABSTRACT

Demyelination is a pathological process which causes profound changes in the physiology of axons. *Post mortem* evidence suggests that mitochondrial content is increased in demyelinated axons which has led to the widely accepted theory that loss of myelin causes an increase in axonal energy demand which in turn can be satisfied by a larger number of mitochondria. However, demyelinated axons are known to undergo a series of changes from conduction block early on in demyelination to altered modes of conduction and finally remyelination and return of normal conduction. Little is known about how these different states influence axonal mitochondria.

In this thesis, mitochondrial function and dynamics were investigated throughout the time course of lysolecithin-mediated de- and remyelination in the saphenous nerve *in vivo*. First, the time course of anatomical and electrophysiological changes after application of lysolecithin was mapped out using semi-thin resin sections and recordings of compound action potentials. Then, mitochondrial dynamics and membrane potential were measured at various time points during the onset and resolution of demyelination. Mitochondrial transport was significantly reduced during the first week of demyelination, preceding the accumulation of stationary mitochondria in the axon. At the same time, mitochondrial membrane potential was significantly increased, particularly at the earliest time points investigated (days 2 and 4). Interestingly, all changes including the above-mentioned accumulation of mitochondria took place before the return of conduction and putative increase in energy demand.

In order to understand better the processes underlying these changes, the role of two known modifiers of mitochondrial dynamics were investigated: action potential conduction and intra-axonal calcium. A 6h conduction block was induced using bupivacaine and confirmed using electrophysiological stimulation but did not lead to any of the changes seen in the early phases of demyelination. On the other hand, calcium

imaging using the genetically encoded calcium sensor Tn-XXL revealed a slight but consistent increase in intra-axonal calcium in demyelinated axons, both at the time point with the highest increase in mitochondrial membrane potential (day 2) and at the time point with the highest mitochondrial density (day 8).

Taken together, these findings point to impaired axonal calcium homeostasis, rather than changes in energy demand, as the main driving force behind mitochondrial changes in demyelination. The fact that mitochondrial transport remained impaired until later in the remyelination process may have implications for the long term survival of chronically demyelinated axons.

TABLE OF CONTENTS

ABBREVIATIONS

AC	Alternating current
ACSF	Artificial cerebrospinal fluid
ADP	Adenosine diphosphate
AIC	Akaike Information Criterion
ALS	Amyotrophic lateral sclerosis
ANOVA	Analysis of variance
AP	Action Potential
ATP	Adenosine triphosphate
AU	Arbitrary Units
βAPP	Amyloid beta peptide
BDNF	Brain-derived neurotrophic factor
CAP	Compound Action Potential
CFP	Cyan fluorescent protein
CI	Confidence interval
CMT	Charcot–Marie–Tooth disease
CNS	Central nervous system
DNA	Deoxyribonucleic acid
DRG	Dorsal root ganglion
DT	Difference Tracker
EAE	Experimental autoimmune encephalomyelitis
EB	Ethidium bromide
ER	endoplasmic reticulum
FAD	Flavin adenine dinucleotide
FCCP	Carbonyl cyanide-4-(trifluoromethoxy)phenylhydrazone
FRET	Fluorescence (or Förster) resonance energy transfer
GDNF	Glial cell-derived neurotrophic factor
GFP	Green-fluorescent protein
HLM	Hierarchical linear model
IGF-1	Insulin-like growth factor 1
ISI	inter-stimulus-interval
LD-50	Lethal dose
LPC	lysolecithin
MAP	Mitogen-activated protein
MCU	Mitochondrial calcium uniporter
MHT	Multiple Hypothesis Tracking
ML	maximum likelihood
mtDNA	mitochondrial DNA
MS	Multiple sclerosis
NA	Numerical aperture

NAD	Nicotinamide adenine dinucleotide
NCLX	Ca2+Na+ exchanger molecule
NGF	Nerve growth factor
NO	Nitric oxide
PBS	Phosphate-buffered saline
PFA	Paraformaldehyde
PNS	Peripheral nervous system
PSF	Point spread function
RC	Respiratory chain
REML	restricted maximum likelihood
RNA	Ribonucleic acid
ROS	Reactive oxygen species
RPT	Refractory periods of transmission
SE	Standard error
SR	sarcoplasmic reticulum
TMRE	Tetramethylrhodamine, ethyl ester
TMRM	Tetramethylrhodamine, methyl ester
TTX	Tetrodotoxin
$\Delta\psi m$	Mitochondrial membrane potential
$\Delta\psi p$	Axonal membrane potential

LIST OF FIGURES

LIST OF TABLES

CHAPTER 1: INTRODUCTION

STUDYING MITOCHONDRIA IN VIVO

In the introduction to his 2005 book *Power, Sex, Suicide – Mitochondria and the Meaning of Life*, Nick Lane describes mitochondria as a badly kept secret: more and more people have heard of them, yet many details of their origin and life cycle are only partially understood. Whilst this certainly still holds true in 2016, considerable efforts are being undertaken to study these fascinating organelles. A quick pubmed search for 'mitochondria' brings up more than 26,000 hits in the last three years alone (Figure 1.1).

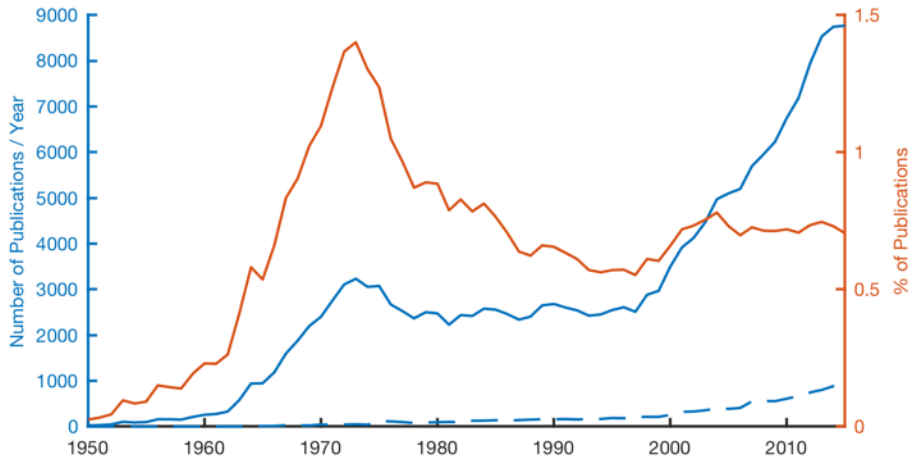

Figure 1.1: **PubMed search results for "mitochondria" by year**. The dashed line shows results with the addition of "*in vivo*".

It is interesting to view the evolution of mitochondrial research from a techniques perspective (Ernster & Schatz 1981). The classic image of a mitochondrion as an oval shaped, striped organelle, for example was a result of the invention of the electron micrograph in the early 1950s. Our understanding of the function of these organelles was made possible by the development of cell fractionation techniques a few years earlier

(Hogeboom et al. 1948). Interest in mitochondria peaked in late 1960s and early 1970s, beginning with the reconstruction of the mitochondrial respiratory chain (Keilin & King 1958; Hatefi et al. 1962). Finally, it was advances in cell culturing which provided the basis for understanding how mitochondria interact with their surroundings, and how they shape, and are shaped by, their host cell's physiology. This tightly controlled environment made it possible to block the expression of proteins or alter mitochondrial function through the precise application of drugs, revealing the function of the mitochondrial machinery piece by piece. The vast majority of what we know about mitochondrial function, dynamics, and life cycle is based on decades of important *in vitro* research. However, despites their success, cell culture studies have clear limitations. Perhaps the most obvious factors are space and time. Axons in the human sciatic nerve, for example, can extend to a length of over one meter and have to be maintained for decades. In contrast, cultured neurons are typically young and have axons which are still growing. This difference is important as growing and regenerating axons are believed to have significantly increased mitochondrial transport (Misgeld et al. 2007; Mar et al. 2014; Lewis et al. 2016) and fission and fusion compared with mature, resting axons (Jendrach et al. 2005; Arnold et al. 2011; Figge et al. 2012). Similar limitations exist with respect to energy supply and demand. The concentration of key factors such as oxygen or glucose in the body varies significantly and dynamically in a way which is difficult to simulate in culture (Chisholm et al. 2016). The same holds for energy demand which in vivo changes constantly depending, for example, on an animal's behaviour. Finally, many physiological and pathophysiological processes which influence mitochondria involve a multitude of cell types and signalling cascades which cannot always be accurately recreated *in vitro*. Inflammation, for example, is a complex interaction of many different cells which has been shown to affect both mitochondrial membrane potential and transport (Nikić et al. 2011; Sorbara et al. 2014).

In order to understand the role of mitochondria in such scenarios, it is necessary to study them in the living animal. Fortunately, the last decades have seen significant advances in microscope technology (Chisholm et al. 2016), leading to a small but increasing number of publications on mitochondrial function *in vivo* (see dashed line in Figure 1.1). This

thesis deals with a number of topics such as changes in energy demand, calcium homeostasis, and destruction and regeneration of the myelin sheath, all of which I believe are best studied *in vivo*.

MITOCHONDRIA AS SUPPLIERS OF NEURONAL ENERGY

The famous description of mitochondria as "powerhouse[s] of the cell" was popularised in an article in Scientific American in 1957 (Siekevitz 1957), almost a decade after Kennedy and Lehninger first discovered that mitochondria are the site of oxidative phosphorylation (Kennedy & Lehninger 1949). The title is particularly apt in neurons which rely on them for an estimated 95% of their ATP supply (Ames 2000) and largely lack the ability to up-regulate glycolysis (Erecińska & Dagani 1990; Erecińska et al. 1993; Bolaños et al. 2010), which means that any increase in energy demand can only be counteracted by increasing mitochondrial ATP supply.

Given the above it is hardly surprising that damage to mitochondria has devastating consequences for nerve cells in general and axons in particular. Blocking mitochondrial complexes using either nitric oxide (NO) donors (Smith et al. 2001; Nikić et al. 2011) or the mitochondrial poison rotenone (Persson et al. 2013) has been shown to provoke rapid swelling of axons followed by degeneration. The underlying mechanism appears to be that mitochondrial dysfunction quickly leads to a local ATP deficit which prevents the Na^+/K^+ ATPase from operating properly. This, especially in combination with neuronal activity (Smith et al. 2001; Persson et al. 2013) leads to the accumulation of sodium in the axoplasm. Once a critical concentration is reached, the Na^+ / Ca^{2+} exchanger begins to work in reverse mode, shuttling Na^+ out of the axoplasm and in turn increasing the concentration of Ca^{2+} (Lehning et al. 1996; Waxman 2008; Witte et al. 2013). Excessive intracellular calcium is a cell death signal which leads, among other things, to the

activation of the axonal protease calpain, and the dissolving of axonal proteins (George et al. 1995).[1]

Mitochondria produce ATP via a process known as oxidative phosphorylation. Briefly, substrates are transported through the inner membrane of the mitochondrion and converted into acetyl CoA which is subsequently fed into the citric acid cycle. In a chain of 8 chemical reactions, the carbon from acetyl CoA is reduced to CO_2 and the electrons gained in the process are stored in the form of NADH, which subsequently interacts with complex I of the respiratory chain (RC), and FADH2, which is part of complex II. The RC is a series of more than 20 different electron carriers organised in four major complexes which are linked by the molecules ubiquinone and cytochrome c. The protein complexes and linkage proteins along the RC have an ascending affinity for electrons which enables mitochondria to pass on electrons from NADH and $FADH_2$ along the RC and onto the strong electron acceptor O_2 (Alberts et al. 2008). The energy which is released in the process powers proton pumps located in complexes I, III, and IV which transport H^+ ions from the inside of the inner membrane to the outside. This leads to the build-up of both a proton gradient (commonly denoted $\Delta\psi m$) and a pH gradient over the inner membrane, resulting in a proton-motive force of approximately 200mV (Nicholls & Ferguson 2013). Not unlike a battery, this gradient serves as an energy storage mechanism. If ATP/ADP levels in the mitochondrial matrix fall below a certain level, the protons flow back into the mitochondrion through a protein called the ATP synthase or F_oF_1 ATPase (Walker 2012). This remarkable protein is closely related to bacterial flagella motors and one of only very few examples of rotary mechanisms found in nature (Nicholls & Ferguson 2013). It consists of two molecular rotary motors: F_o which is embedded in the inner membrane, and F_1 which resides within the matrix (Okuno et al. 2011). In isolation, F_1 acts as an ATP consuming motor. It consists of a

[1] Whilst both NO and rotenone block the mitochondrial transport chain, they may not damage the axon via precisely the same pathway: As opposed to rotenone, NO is also involved in the opening of the mitochondrial transition permeability pore and may cause degeneration via the release of cytochrome C from mitochondria in the presence of Ca^{2+}(see e.g. Martin et al. 2011). NO has many effects, including impairing the function of the sodium pump and making sodium channels open for longer, both of which also promote intracellular Na. Nevertheless, ATP deficiency and Ca^{2+} influx are important steps involved in both mechanisms.

pole-like γ-subunit that is surrounded by a cylinder made of 3 α and 3 β subunits. Upon binding of ATP to the β-subunits and its subsequent cleaving by interaction with H_2O, these undergo a conformational change that translates into a counterclockwise rotation of a γ-pole (Masaike et al. 2008). However, this ATP consuming process is reversible. Forced clockwise rotation of γ-unit using magnetic beads has been shown to be sufficient to generate ATP from ADP and Phosphate (Itoh et al. 2004; Rondelez et al. 2005). In the mitochondrion, this forced rotation of γ is realized through the F_0 motor. This outer part of the protein consists of a ring of c subunits as well as an ab_2 strator. While the strator connects to the $\alpha_3\beta_3$-cylinder of the F_1 unit and keeps it in place, the c ring forms an ion channel that connects to the F_1 γ-subunit. As H^+ ions pass through the channel into the matrix, the c ring and the connected γ-pole turn clockwise (Okuno et al. 2011). This way F_oF_1 acts as an ATP synthase as long as it is driven by the proton-motive force[2].

In addition to ADP-ATP conversion, other essential mitochondrial processes are driven by $\Delta\psi m$, too. Pyruvate and inorganic phosphate, for example, need to be co-transported into the matrix along with H^+ (Alberts 2008). Similarly, the exchange of ADP and ATP utilizes the voltage difference across the membrane. Here, a protein called adenine nucleotide translocase shuttles ATP into the cytosol and ADP into the matrix.

All this makes the mitochondrial membrane potential the basis of neuronal energy production and thus neuronal survival. However, there are downsides to this way of producing and storing energy: as they build up a protonmotive force over their inner membrane, mitochondria produce superoxide (O_2^-), a reactive species of oxygen (Murphy 2009). Most superoxide is quickly turned into hydrogen peroxide, both spontaneously and

[2] Interestingly, F_1 retains its ability to act as an ATPase persists even in connection with F_o. If the voltage difference over the IM drops below a certain reversal potential, F_oF_1 reverses its function and consumes ATP while pumping cations out of the matrix (Chinopoulos 2011). ADP/ATP and pyruvate transport are also reversible. It follows that strongly depolarized mitochondria do not only cease to produce ATP but start to actually take it up from the cytosol and consume it (Chinopoulos et al. 2010; Chinopoulos 2011).

through the protective enzyme superoxide dismutase (Bedard & Krause 2007). However, due to its proximity to mitochondrial proteins and genome (see below) some oxidative damage is unavoidable. Furthermore, NO and superoxide can combine to the very powerful oxidizing agent peroxynitrite ($ONOO^-$) which is believed to cause significant damage in inflammatory conditions such as multiple sclerosis (Cross et al. 1998).

In isolated mitochondria and permeabilised cells, both the rate of ATP production and the production of reactive oxygen species raise exponentially with the increase in membrane potential (Starkov & Fiskum 2003; Chinopoulos et al. 2009; Kawamata et al. 2010). Furthermore, O_2^- production has been shown to increase if ATP levels are high and mitochondria sit idle (Murphy 2009). This trade-off between ATP produced by mitochondria and damaged caused in the process together with the high complexity of mitochondria (and therefore high cost of producing and maintaining them, see below) likely explains why mitochondria are not found in superabundance but rather constantly relocated to where they are most needed (MacAskill et al. 2010; Sajic et al. 2013).

MITOCHONDRIAL MAINTENANCE

Mitochondria are very complex organelles containing an estimated 1500 different proteins (Calvo et al. 2006), as well as copies of their own genome (mtDNA), all of which are stored in a very small space. mtDNA only encodes a small set of proteins (13 polypeptides out of a total of 37 genes) which fulfil essential functions in the respiratory chain (Chinnery & Hudson 2013). These 13 proteins are only encoded in mtDNA while all other mitochondrial proteins are encoded in nuclear DNA. This puts mitochondria in a special position: In order to maintain their function, they are dependent on two distinct sets of DNA stored in different locations. As a result, mitochondria have evolved a set of 'on board' repair mechanisms which are able to ameliorate some of the damage caused by reactive oxygen species (Kazak et al. 2012). However, this does not fully prevent the accumulation of damage over time which is believed to eventually lead to a reduction in mitochondrial function. In addition to the damage accumulated by single mitochondria,

the health of the mitochondrial population as a whole has also come into focus. This is driven by evidence from live cell imaging showing that mitochondria in the same cell exchange proteins and DNA through fission and fusion (Legros et al. 2002; Malka et al. 2005; Ma & O'Farrell 2015). This can lead to damage to mtDNA (usually in the form of deletions) being spread throughout the mitochondrial population of a cell, ultimately rendering the host cell respiratory deficient (Krishnan et al. 2008; de Grey 2009; Fukui & Moraes 2009). Hence, maintenance of a healthy population of mitochondria is only possible through continuous rejuvenation of the mitochondrial population by creating new mitochondria (mitochondrial biogenesis) and removing old specimens (mitophagy) (Liesa & Shirihai 2013). In axons and dendrites, mitochondria are known to exist in two different states: The majority of them are elongated and stationary, while a smaller number of shorter mitochondria can be seen moving in either direction (Misgeld et al. 2007; Sajic et al. 2013; Sorbara et al. 2014). Computer simulations suggest that the stationary population needs to undergo repeated selective fusion with new, healthy organelles followed by fission to keep the spread of damaged mtDNA under control and that small drops in the rate of such exchanges can significantly increase the chance of a cell becoming respiratory deficient (Elson et al. 2001; Twig et al. 2008; Mouli et al. 2009)[3].

As mentioned previously, the vast majority of mitochondrial proteins are encoded by the nuclear genome. There is some controversy about whether it follows that synthesis of said proteins is therefore restricted to the proximity of the nucleus. Some evidence suggests that axonal synthesis of mitochondrial proteins occurs and is of functional importance (Amiri & Hollenbeck 2008; Kaplan et al. 2009). However, there is a disconnect

[3] Computer simulation of the spread of ΔmtDNA through random drift is a fascinating tool for understanding the consequences of mtDNA damage. It is my belief, however, that current simulations do not accurately reflect the consequences of mtDNA deletions in neurons: to the best of my knowledge, all publications to date employ a simplified model of mtDNA exchange in which every mitochondrion within a cell can fuse with every other one. This is far from the reality in a highly polarized cell such as a neuron where mitochondria at the axon terminal and near the nucleus can be as much as a meter apart. Since decreasing the total amount of exchangeable mtDNA in a cell has been shown to accelerate the spread of ΔmtDNA (Payne et al. 2011), modifying the existing models to incorporate neuronal cell architecture might result in (locally) higher estimates of ΔmtDNA.

between findings *in vitro*, where evidence of axonal translation is abundant and *in vivo*, particularly in adult animals, where the importance of such mechanisms is less clear (Jung et al. 2012). A similar picture emerges with respect to mitochondrial DNA: while a study of cultured sensory neurons of chick embryos suggested that mtDNA does replicate in axons, even if they are separated from their nucleus (Amiri & Hollenbeck 2008), research carried out in our lab using a similar technique failed to show the same effect in adult mice *in vivo*, indicating instead that mitochondrial biogenesis is largely, if not exclusively, confined to the soma (Radha Desai, unpublished research). Finally, it has been argued that degradation of mitochondria (mitophagy) through fusion of the organelles with lysosomes is largely confined to the cell body (Cai et al. 2012).

Taken together, these findings indicate that providing new mitochondria within axons or removing old ones requires transporting them to and from the soma respectively. The importance of this process is clearly demonstrated in conditions of impaired mitochondrial transport. Most prominently, Charcot–Marie–Tooth type 2A is an inherited form of peripheral neuropathy caused by mutations of the mitochondrial motor protein KIF1B β (type 2A1) (Zhao et al. 2001) or of the mitochondrial fusion protein MFN2 (type 2A2) (Baloh et al. 2007; Misko et al. 2010), both of which cause significant impairment of mitochondrial movement. Beginning in early adulthood, this impairment leads to the degeneration of peripheral nerves, starting with the longest axons. Similarly, impairment of mitochondrial dynamics has been shown in animal models of amyotrophic lateral sclerosis (ALS) which, in humans, is characterized by the degeneration of motor neurons (De Vos et al. 2007; Bilsland et al. 2010).

While these examples show that mitochondrial transport is critical to guarantee the survival of neurons over their decades-long lifetimes, it also comes with a cost. Diana Zala and colleagues elegantly demonstrate that an ATP decrease of approximately 20% within the axons of cultured neurons is sufficient to bring axonal transport of mitochondria to a near-complete stop (Zala et al. 2013). Mitochondrial transport may also compromise ATP production as mitochondria appear to be most energetically efficient when they are (hyper-) fused to form a single, long organelle (Liesa & Shirihai 2013; Rolland et al. 2013), whereas transported mitochondria are generally much smaller

in size (e.g. Sajic et al. 2013) and preventing the fission of large mitochondria leads to a breakdown of transport (Li et al. 2004). Neurons thus need to balance the risk of a temporary energy failure against the cost of maintaining a larger pool of mitochondria.

In summary, two opposing forces shape the number and distribution of mitochondria in cells in general and neurons with long processes in particular: the need to guarantee adequate, local supply of ATP at all times and the complicated process of maintaining a healthy mitochondrial population. In the next section, I will look at the mechanisms behind mitochondrial transport in more detail before coming back to axonal energy demand and its connection to myelination.

MECHANISMS AND CONTROL OF MITOCHONDRIAL TRANSPORT

Most mitochondrial movement is carried out along microtubules which, in axons, are arranged with their (+) ends facing towards axon terminals and (-) ends towards the soma (Baas et al. 1989). As seen in other kinds of axonal transport, anterograde movement of mitochondria along these structures is driven by kinesin, whereas retrograde transport is controlled by dynein. However, a significant amount of complexity is introduced by different adaptor proteins connecting the motors with the mitochondrial membrane (Saxton & Hollenbeck 2012). The best understood mitochondrial transport complex is the one which appears to account for most of the anterograde movement of mitochondria: here, the mitochondria outer membrane receptor Miro (MacAskill et al. 2009; Chen & Sheng 2013) is coupled to the adaptor protein Trak1 (Koutsopoulos et al. 2010; Brickley & Stephenson 2011) which, in turn, binds to kinesin (more precisely, kinesin-1, or KIF5B) (Tanaka et al. 1998). However, alternative adaptor proteins have also been proposed. Syntabulin appears to be able to link the mitochondrial outer membrane directly to the kinesin motor (Cai et al. 2005), as do the proteins FEZ1 and RANBP2 (Fujita et al. 2007; Cho et al. 2007). The retrograde transport machine is somewhat less understood but a recent study showed that dynein, together with its

auxiliary complex dynactin, can also be linked to mitochondria via the Trak isoforms 1 and 2 (van Spronsen et al. 2013). It is thus possible that mitochondria simultaneously bind motor proteins for both anterograde and retrograde movement. In fact, such a setup is supported by experiments carried out in Drosophila which demonstrate that disturbing the function of either kinesin or dynactin impedes transport in both directions, suggesting an interaction between the two motor complexes (Pilling et al. 2006; Haghnia et al. 2007).

What is not yet well understood is precisely how mitochondrial transport is controlled. Some factors have been identified which are involved in the arrest of mitochondrial movement. An early report suggested that increases in local ADP attract and arrest mitochondria (Mironov 2007) but a mechanism explaining how the transport machinery might sense this increase was never found (Lovas & Wang 2013). Instead, calcium has emerged as potentially the most important stop signal for mitochondria. While mitochondrial movement is commonly seen in axons at baseline Ca^{2+}, increasing its concentration using calcium ionophores arrests mitochondrial movement in primary neuron cultures (Saotome et al. 2008) and excised frog nerves (Zhang et al. 2010). Conversely, using calcium chelators or calcium free media has been shown to increase mitochondrial movement in neurites (Zhang et al. 2010; Ohno et al. 2011).

Two different aspects of Ca^{2+} dependent mitochondrial arrest in axons have been described and likely act together to stop mitochondria in what has been called 'engine switch and break' (Sheng 2014). The mitochondrial membrane protein Miro contains calcium binding sites. As these are activated, Miro undergoes a conformation change and appears to bind directly to kinesin, dissociating it from microtubules (Wang & Schwarz 2009). In addition to this 'stepping off the gas pedal', mitochondria also become anchored to microtubules by a protein called syntaphilin. Syntaphilin is likely present in the axon independently of mitochondria (Kang et al. 2008; Sheng 2014) but can be translocated to mitochondria where, in the presence of calcium, it disrupts the Trak-kinesin complex, binds KIF5 and inhibits the molecular motor's ATPase (Chen & Sheng 2013; Sheng 2014). Importantly, syntaphilin was found to arrest mitochondrial movement independently of the direction of movement, thus representing a mechanism by which calcium can lead to a complete arrest of axonal mitochondria.

In neurons, sites with high calcium influx are also often the sites with the highest energy demand. Chemical synapses, for example, have been estimated to account for nearly half of a grey matter neuron's ATP demand (Howarth et al. 2012, see also below) and because vesicle release is driven by calcium influx, Ca^{2+} serves as a good indicator of activity and thus energy demand. Of course this doesn't exclude the possibility that mitochondria can directly sense and accumulate in areas of high energy demand. But to our current knowledge, calcium signalling may be both necessary and sufficient to control local energy supply in neuronal processes (Macaskill et al. 2009; MacAskill et al. 2010). However, in addition to being controlled by it, mitochondria also actively influence the cell's calcium household by ingesting, buffering and releasing calcium. This process is discussed below.

MITOCHONDRIAL CALCIUM BUFFERING

Mitochondria have been shown to store impressive calcium concentrations of up to 1000 nmol per mg mitochondrial protein (Nicholls 2005). Like so many other mitochondrial processes, the influx of calcium is largely driven by the membrane potential which moves Ca^{2+} anions through the membrane into the inner matrix. Interestingly, even though mitochondria have been known for over 50 years to accumulate calcium (Deluca & Engstrom 1961; Vasington & Murphy 1962), it was not until 2011 that the molecular identity of the main inward bound calcium channel, the mitochondrial calcium uniporter (MCU), was revealed (De Stefani et al. 2011; Baughman et al. 2011). Efflux of Ca^{2+} happens in exchange for Na^{+} through the $Ca^{2+}Na^{+}$ exchanger molecule NCLX (Palty et al. 2010)[4]. It is driven both by free Ca^{2+} and a low concentration of Na^{+} in the inner

[4] In addition to NCLX, a non-specific channel named the mitochondrial permeability transition pore (MPTP) can facilitate rapid release of mitochondrial calcium (Haworth & Hunter 1979). This appears to happen mainly upon mitochondrial depolarisation or extreme calcium overload, and under conditions of oxidative stress (Hunter & Haworth 1979; Halestrap et al. 1997; Martin et al. 2011) and has been shown to play an important role in cardiac reperfusion injury (Nakagawa et al. 2005). Because mice lacking the protein cyclophilin D which is necessary for MPTP opening develop normally (Baines et al. 2005; Nakagawa et al. 2005), MTPT opening is generally seen as a catastrophic event, although a role in normal physiology cannot be excluded (see e.g. Barsukova et al. 2011).

mitochondrial matrix which in turn is a consequence of sodium leaving the mitochondrion in exchange for H^+ pumped out by the respiratory chain. On the surface, this seems like an expensive and fairly circular system. However, as Nichols et al showed in an important series of experiments on isolated mitochondria (summarised in Nicholls 2005), it makes perfect sense when considering the different changes in kinetics of influx and efflux in reaction to changing external calcium concentrations. The MCU is highly specific for Ca^{2+} and has a relatively low affinity at low external Ca^{2+} concentrations, but its throughput increases significantly as $[Ca^{2+}]_e$ increases (Nicholls suggests an increase as a 3.5 power function of $[Ca^{2+}]_e$ in brain mitochondria). Calcium efflux, on the other hand, is remarkably stable over a wide range of $[Ca^{2+}]_e$, both due to the rate limit of the Na^+ Ca^{2+} exchanger and because much of the Ca^{2+} in the mitochondrial matrix is buffered by phosphate, keeping the concentration of free calcium stable and relatively independent of the extra-mitochondrial concentration. These "scale-able" calcium dynamics enable mitochondria to clamp the intracellular calcium in their surroundings to a relatively stable level. The effect is strong enough so that in pancreatic acinar cells and perhaps also in neurons mitochondria are able to form "belts" around areas of high calcium influx which stop Ca^{2+} waves from spreading through the cell (Tinel et al. 1999; reviewed in Rizzuto et al. 2012).

Some discussion remains about the speed at which mitochondria take up calcium. Some have argued that the low affinity prohibits mitochondria from influencing fast, calcium-driven cellular processes (Williams et al. 2013), while others have pointed out that local levels of Ca^{2+}, for example in synapses or near the ER / SR can get extremely high compared with the average level of intracellular calcium, thus driving the V_{max} of mitochondrial calcium intake to levels significantly above even what is seen in isolated mitochondria *in vitro* (Nicholls 2005; Rizzuto et al. 2012). But irrespective of whether mitochondrial calcium buffering can influence the fastest of calcium driven events there is experimental evidence that suggests that it does influence the host cell's calcium signalling. In neurons, mitochondria have been shown to aid the recovery from high frequency stimulation-based synaptic depression (Billups & Forsythe 2002); knocking out syntaphilin and thus reducing the number of stationary mitochondria in post-synaptic

boutons was reported to change the synaptic response to high frequency stimulation by causing short-term facilitation (Kang et al. 2008); and inhibiting mitochondrial calcium uptake was shown to narrow the dynamic response of olfactory sensory neurons during odour stimulation (Fluegge et al. 2012). All of this suggests that mitochondrial calcium buffering plays a role in normal neuronal, and particularly synaptic, function[5].

NEURONAL ENERGY DEMAND AND MYELINATION

It is widely agreed that brains as a whole and neurons in particular have a high energy demand compared with other cell types (Rolfe & Brown 1997). However, relating this demand to different cellular processes is a challenging task. Broadly speaking, neuronal energy demand can be broken down into an active and a passive component. Passive (that is, activity independent) energy demand is cause by general housekeeping activity such as protein turnover, cellular transport, and the upkeep of the cell's membrane potential. Active demand, on the other hand, is cause by the firing of action potentials as well as synaptic transmission and depends directly on the cell's signalling activity. The balance between these factors differs significantly between white and grey matter regions of the brain. Using extensive simulations of cerebellar neurons, Attwell, Laughlin, Howarth, and Gleeson estimated that in the grey matter passive processes account for about 40% of a neuron's total ATP demand (25% for non-signalling related activity and 15% for the upkeep of membrane potentials), action potentials make up 16%, and at 44% synaptic transmission consumes the biggest chunk of energy (Attwell & Laughlin 2001; Howarth et al. 2012). The white matter presents a different distribution of energy demand. Here, only very few synapses can be found, reducing the proportion of total energy demand due to synaptic transmission almost to zero. The proportion of

[5] It is worth pointing out, however, that MCU knockouts are nonetheless viable and, apart from weaknesses during prolonged physical activity, appear relatively normal (Pan et al. 2013) which suggests that at least under physiological conditions neurons may be able to compensate for reduced mitochondrial calcium buffering.

housekeeping and maintenance of the cell's membrane potential, in turn, are increased to 56% and 44% of the local energy demand (Harris & Attwell 2012).

Perhaps surprisingly, the relative cost of action potential conduction in the mature white matter is estimated to be very low ($< 1\%$). This is largely due to myelination. In myelinated axons (as in demyelinated ones) the action potential itself is actually "free" as it is powered by the potential and concentration gradient already established across the cell membrane. ATP consumption only occurs after the action potential as the gradient is restored by pumping Na^+ out of the cell and K^+ in (Debanne et al. 2011). This is done by the Na^+/K^+ exchanger at a rate of 1 ATP per 3 Na^+ and 2 K^+. The ATP cost per action potential is therefore proportional to the amount of sodium which enters the cell. Myelin, whether produced centrally by oligodendrocytes or peripherally by Schwann cells, significantly reduces the capacitance of the axon membrane. Instead of a widespread exchange of K^+ and Na^+ along a leaky axon membrane, ion channels are arranged such that Na^+ and K^+ exchange is restricted to the centre of the node of Ranvier and the juxta-paranode, respectively, while the internodes are comparatively impenetrable for both ions. This setup significantly lowers the amount of sodium influx necessary for action potential propagation and consequently the amount of ATP necessary to restore the membrane potential.

The reduction in capacitance, and therefore reduction in energy demand depends on the thickness of the myelin sheath and the total axonal surface area. Both are often combined into the so-called g-ratio, that is the axonal diameter to the total outer diameter including myelin (an increase in this ratio therefore means a relative decrease in myelin thickness). In adult mammals, the g-ratio was found to be fairly constant for axons of the same type and has been shown to be close to the theoretical optimum for high speed conduction (Rushton 1951; Chomiak & Hu 2009). Assuming a g-ratio of 0.81 (a common value in the CNS) Harris and Attwell estimate that myelination reduces the cost of every single AP (or rather every restoration of the membrane potential) by about two orders of

magnitude compared with unmyelinated grey matter (Harris & Attwell 2012)[6]. This difference is likely even higher in the PNS, where g-ratios are lower (Arbuthnott et al. 1980).

The mammalian optic nerve provides a well-known real-world example of this difference. Fibres in the adult optic nerve head contain both myelinated and unmyelinated regions which are subjected to the same levels of activity. Intriguingly, multiple lines of evidence suggesting that the energy demand due to neuronal activity is indeed higher in the unmyelinated parts of the nerve. Compared with the myelinated sections, it is surrounded by a denser network of capillaries and astrocytic processes and it is more vulnerable to ischaemia (Balaratnasingam et al. 2010; Chan et al. 2012). Furthermore, there is histochemical and immunochemical evidence of stronger activity of cytochrome c oxidase (Yu et al. 2013). Finally, and perhaps most importantly, mitochondrial density was found to be significantly larger in the unmyelinated part relative to the myelinated part of the axons (Barron et al. 2004) which, in agreement with the theory laid out above, correlated with a larger number of sodium channels.

The optic nerve also demonstrates another important quality of axonal bioenergetics: energy supply and demand are highly local. ATP is a very unstable molecule and its diffusion through the dense intracellular environment is believed to be limited (Clegg 1984; Jones 1986; Ames 2000). Therefore, energy needs to be supplied very close to where it is consumed, a fact that is also demonstrated by the high density of mitochondria at synapses (which are areas of high energy demand, as discussed above) (MacAskill et al. 2010).

This leads to the interesting question of how an adult neuron can cope with the focal loss of myelin. Based on the above, if the cell is active, this should lead to an increase in local energy demand which requires a local increase in energy supply. On the other hand,

[6] Interestingly, it does not follow that myelination conserves energy overall. While AP propagation is made significantly cheaper, this is likely outweighed by the energy needed to maintain the myelinating cells (Harris & Attwell 2012). Instead, it is factors such as speed of conduction and the axon diameter necessary to guarantee it or reliability of action potentials which explain the evolutionary advantage of myelination (Faisal & Laughlin 2007; Hartline & Colman 2007; Neishabouri & Faisal 2014).

neurons which do not fire may undergo a (small) decrease in energy demand. Since axons in the spinal cord or the peripheral nervous system can grow to a length of more than a metre, any adaptation needs to happen far from the cell body and possibly without orchestration.

THE PATHOLOGY OF DEMYELINATION AND ITS CONNECTION TO MITOCHONDRIA

Demyelination is a hallmark of multiple debilitating neurological diseases including multiple sclerosis (MS), optic neuritis, Guillain–Barré syndrome, inherited leukodystrophies, and most forms of Charcot–Marie–Tooth disease (CTM). All of these conditions cause disability, which is highly correlated with axonal loss (Davie et al. 1995; De Stefano et al. 1998; Rudick et al. 1999; Garbern et al. 2002; Pareyson et al. 2006). This has led to considerable interest in the link between demyelination and axonal degeneration.

Acute demyelination is usually not a catastrophic event. Despite the aggressive nature of its relapses, demyelinated but intact axons are commonly found in both active (inflamed) and inactive lesions in multiple sclerosis (e.g. Lassmann et al. 2012). Similarly, in animal models of transitory demyelination induced by toxins such as lysolecithin (Hall & Gregson 1971), ethidium bromide (Blakemore 1982), or cuprizone (Blakemore 1973), most axons survive the demyelinating event and regain function. Instead, demyelination appears to cause a vulnerability which leads to axonal loss over time even in the absence of inflammation. Irvine and Blakemore demonstrated that delaying remyelination in cuprizone-treated mice through radiation (Irvine & Blakemore 2008) or simply increased age of the animal (Irvine & Blakemore 2006) leads to increased axonal loss after 16 weeks. The effect can also be observed in human pathology studies of MS where axons in chronically demyelinated, inactive lesions show significantly more signs of degeneration compared to those in remyelinated lesions (Trapp et al. 1998; Kornek et al. 2000). It is also not clear, whether remyelination can fully stop the degeneration. In the above-

mentioned paper by Kornek *et al.*, remyelinated axons were still 1.4x as likely to show βAPP-positivity (a common marker of axonal degeneration) as normal white matter. Similarly, Manrique-Hoyos *et al.* describe a second wave of motor axon degeneration six months after cuprizone-induced demyelination, following an initial recovery (Manrique-Hoyos et al. 2012).

Over the last decades, a number of theories have been proposed which link demyelination to axonal decline. Demyelinated axons undergo a number of changes in their physiology and composition of ion channels which are believed to increase their energy demand (see below as well as the introduction to chapter 4 for details). If this increased demand cannot be met with sufficient supply, the cell is believed to enter a state termed "virtual hypoxia" (Trapp & Stys 2009). As described above, a lack of ATP needed to drive the Na^+/K^+ exchanger leads to the accumulation of sodium in the axoplasm which leaves the cell in exchange for Ca^{2+} through reverse-operation of the Na^+/Ca^{2+} exchanger, ultimately causing Ca^{2+} triggered cell death. This process is likely exasperated in inflammatory environments, where healthy myelin acts as a protective barrier against damaging molecules such as nitric oxide (NO) (Redford et al. 1997), which can lead to the degeneration of electrically active axons (Smith et al. 2001; Kapoor et al. 2003). Finally, studies in mice (Griffiths et al. 1998) and humans (Garbern et al. 2002) with genetic defects that produce oligodendrocytes which lack proteolipid protein 1 but nevertheless form compact myelin have shown that myelinating cells supply not just the myelin itself but also trophic support in the form of neurotrophic factors. Subsequent experiments have revealed a list of such factors supplied by oligodendrocytes, including IGF-1 (Wilkins et al. 2001), and GDNF (Wilkins et al. 2003; Nave 2010 for a review).

Intriguingly, the first two mechanisms are directly connected to the axon's pool of mitochondria. As laid out above, mitochondria supply virtually all ATP of a neuron and buffer its calcium. Furthermore, high concentrations of NO disturb mitochondrial ATP production by interfering with electron transfer at cytochrome oxidase (Brookes et al. 1999; Pacher et al. 2007) and increase the formation of peroxynitrate, which causes lasting damage to mitochondrial proteins and DNA (Campbell et al. 2011).

One particularly interesting indication of a link between demyelination, axonal degeneration, and mitochondria can be found in the different forms of Charcot–Marie–Tooth disease (CMT). CMT is an inheritable neuropathy characterised by the degeneration of long peripheral axons with minimal inflammation and which leads to the progressive loss of muscle mass and sensation (Vallat et al. 2013). Most subtypes of CMT affect Schwann cells and cause demyelination (Bouhy & Timmerman 2013). However, one particular sub-family of the disease, type 2A, leads to axonal loss by impairing the transport of axonal mitochondria through a defect in the motor protein KIF1B β (Zhao et al. 2001) or the mitochondrial fusion protein MFN2 (Baloh et al. 2007). Intriguingly, the clinical outcome – progressive loss of peripheral axons starting with the longest – is remarkably similar in both cases (Krajewski et al. 2000; Vallat et al. 2013). This similarity could be explained if demyelination lead to a decrease in mitochondrial transport.

Studying the role of mitochondria in demyelination, therefore, can lead to a better understanding of the "slow burning" degeneration of chronically demyelinated axons in CMT and other diseases.

DEMYELINATION AND MITOCHONDRIA: PREVIOUS WORK AND OPEN QUESTIONS

Both the physiology of demyelinated axons, and the relationship between demyelination and mitochondrial density have been studied in some detail. Much of our understanding of the physiology of demyelinated axon stems from a series of experiments by Smith, Bostock, Hall *et al.* in the early 1980s. Using toxin-induced demyelination in the rat and mouse saphenous nerve, and later the spinal cord, the authors showed that following acute loss of myelin, axons undergo a phase of conduction-block and complete loss of excitability, which persists for a few days (Felts et al. 1997; Smith & Hall 1980). After this initial period, axons regain the ability to be excited and propagate currents over small distances, albeit in a very different manner to normal conduction: in the case of lysolecithin (LPC)-mediated demyelination (see chapter 2), conduction was shown to

return in a micro-saltatory fashion with novel foci of inward currents at short intervals found along the still naked axon (Smith et al. 1982). At a similar time point, axons demyelinated using diphtheria toxin were shown to conduct in a continuous fashion (Bostock & Sears 1978). Robust propagation of action potentials did not occur until later when axons were again surrounded by a thin sheet of myelin. Even then, however, action potentials were found to be elongated, slower, and with significantly prolonged refractory periods (Smith & Hall 1980). At this point in the demyelination – remyelination cycle, demyelination of the saphenous nerve has also been reported to lead to spontaneous action potential firing (Smith & McDonald 1980; Kapoor et al. 1997; Wallace et al. 2003). Normal conduction returned only much later after the myelin sheaths surrounding axons had returned to their maximal remyelinated thickness (Smith et al. 1979; Smith & Hall 1980). Others soon contributed potential cellular correlates of these effects: both sodium (Shrager 1989; Black et al. 1991; Novakovic et al. 1996; Craner et al. 2003) and potassium (Rasband et al. 1998) channels, which are usually confined to the nodes of Ranvier were found to be redistributed along demyelinated axon. Additionally, accumulation of calcium channel subunits (Kornek et al. 2001) and acid sensing calcium channels (Vergo et al. 2011) have been reported in inflammatory demyelination, suggesting potential changes in axonal calcium homeostasis. In fact, increased axoplasmic Ca^{2+} is widely regarded as a consequence of demyelination (Waxman 2006; Trapp & Nave 2008), although to my knowledge this has never been experimentally confirmed.

These alterations in axonal physiology, particularly in the phase of returning micro-saltatory conduction, could be predicted to have an effect on axonal energy consumption and therefore mitochondria. And, indeed, there have been a number of investigations corroborating this theory. *Post mortem* studies of both animal models of demyelination (Mutsaers & Carroll 1998; Hogan et al. 2009) and brains of patients with the demyelinating disease multiple sclerosis (Zambonin et al. 2011; Campbell & Mahad 2011) have consistently shown an increase in both the size and number of mitochondria in the region of demyelination. Similarly, mitochondrial activity (measured via cytochrome c histochemistry) was found to be significantly increased in mice carrying the dysmyelinating shiverer mutation (Andrews 2006). These findings have had a strong

influence on theories of axon degeneration in chronic demyelination (Trapp & Nave 2008; Lassmann & van Horssen 2011; Campbell et al. 2012) where the observed accumulation of mitochondria is commonly interpreted as a physiological (and healthy) reaction which ultimately preserves the axon.

Mitochondrial dynamics and function in demyelination have been investigated to a lesser extent. Most of what we know about mitochondrial transport in demyelinated axons stems a series of *in vitro* experiments from Bruce Trapp's lab. Using co-cultures of DRG neurons and Schwann cells, the authors report significantly increased mitochondrial transport 48h after LPC induced demyelination which returns to baseline levels after remyelination 15 days later (Kiryu-Seo et al. 2010). They demonstrate that this change is not caused by LPC itself and they suggest the neuronal transcription factor ATF3, which is known to play a role in regeneration, is required for the observed increase of transport. Though a later study involving the same authors and using the same method failed to show the same effect (Zambonin et al. 2011), it was recently replicated successfully in cultured slices (Ohno et al. 2014) which were treated with LPC for 26h and imaged after another 24h. These studies suggest that the cell might compensate for the putative increase in energy demand by increasing the production and trafficking of mitochondria which, given the constraints above, seems like an appropriate reaction. There are, however, some caveats which make it hard to extrapolate these findings to the living animal. The studies are restricted to early time points at which, at least *in vivo*, the axon could be expected to experience conduction block (Smith & Hall 1980). One could therefore argue that the reported increase in transport is in line with findings of increased axonal transport in axons blocked with TTX (Ohno et al. 2011; Obashi & Okabe 2013). If the increase in transport is indeed a direct effect of conduction block, it would be interesting to observe whether a return of conduction in a more energetically expensive, micro-saltatory fashion has the opposite effect (although this might be difficult to achieve *in vitro*). Activity aside it is interesting to speculate what effect such a lesion might have if it was focal and far enough removed from the cell body. *In vitro* demyelination is spread across the whole culture with the same dose of LPC reaching the somata as reaches the axons. Since LPC interacts with both G-protein coupled receptors

and MAP kinase pathways (Bassa et al. 1999; Jing et al. 2000; Xu 2002) this kind of application is likely to have significant effects on the soma. If demyelination occurred away from the cell body, might it cause the same kind of increased transport but without the increased supply from the soma, thereby draining mitochondria from the axon and leaving it exposed to the increase in energy demand after remyelination?

Another observation with potential effects on mitochondrial trafficking is that the diameters of demyelinated axons both after treatment with LPC and in experimental autoimmune encephalitis were reported to be smaller than those of myelinated ones (Raine et al. 1969; Hall & Gregson 1971). The changes were found to correspond well with the time course of demyelination and were largely reversed by remyelination (Hall & Gregson 1971). Furthermore, it was found that the axonal cytoskeleton undergoes reversible changes in LPC demyelination and that these changes are likely secondary to the demyelination rather than a direct effect of the LPC (Jean et al. 2002). Both changes may be highly relevant for mitochondrial transport as axons are spatially very restricted environments (Wortman et al. 2014), particularly given the high density of stationary mitochondria in demyelinated axons. Experiments in *Drosophila* have suggested that accumulation of mitochondria can impose enough of a spatial constraint to impair axonal trafficking (Narayanareddy et al. 2014) and cell culture experiments suggest that axonal transport slows down in the vicinity of stationary organelles (Che et al. 2016). It is therefore at least conceivable that an increase in mitochondrial density, particularly combined with a decrease in intra-axonal volume could lead to further impairment of mitochondrial trafficking.

Finally, there is the question of mitochondrial function / activity. Kiryu-Seo *et al.* convincingly demonstrate that knockout of the mitochondrial anchoring protein syntaphilin in combination with demyelinating treatments leads to axonal death both *in vivo* and *in vitro* (Kiryu-Seo et al. 2010). This strongly suggests that the increased mitochondrial content in demyelinated axons is necessary for axonal survival. However, it is not entirely clear what function the additional mitochondria fulfil. The early time

point indicates that their main function is not to balance out increased energy demand. However, the other common explanation, that they might buffer increased intracellular calcium, seems at odds with the observed increase in transport (compare e.g. Saotome et al. 2008; Zhang et al. 2010).

In summary, whilst a link between demyelination and mitochondria is well established, many of the details are still unknown. In particular, it would be desirable to understand mitochondrial function and dynamics at different time points during de- and remyelination as these are characterised by vastly different activity patterns of the axon.

STRUCTURE, AIMS AND OBJECTIVES

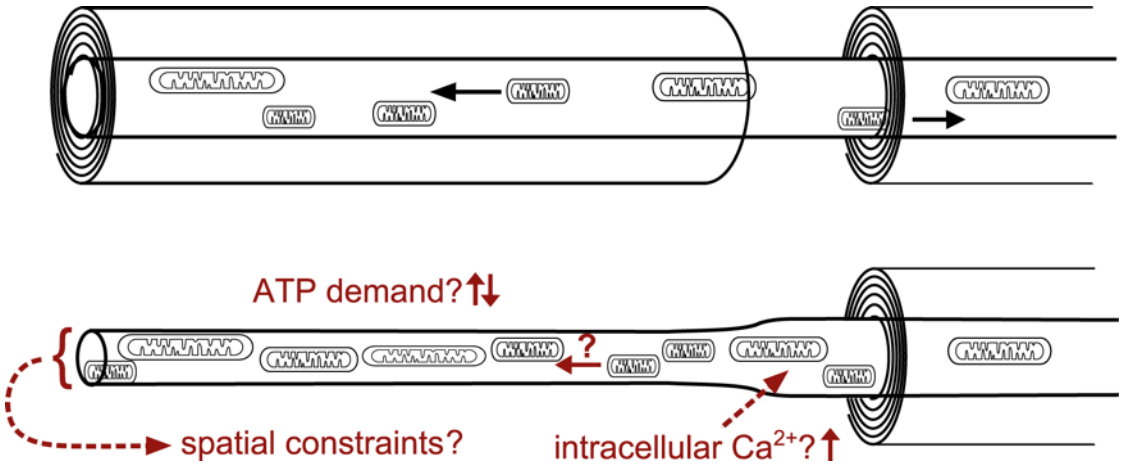

Figure 1.2: **Potential influences on mitochondrial function and dynamics in demyelination**. Factors include changes in energy demand (both increasing and decreasing), calcium homeostasis, and spatial constraints. See text for details.

The aim of this PhD project is to investigate changes in mitochondrial dynamics in demyelinated axons under conditions of realistic energy demand *in vivo*. Chapter 2 begins with a pilot study during which the well-established lysolecithin model of demyelination is replicated in the saphenous nerve and mitochondrial dynamics in myelinated and demyelinated axons are assessed at a single time point. Chapter 3 describes the methods

for quantifying mitochondrial function and dynamics in more detail and contains my findings about mitochondria in the saphenous nerve of naïve animals. In Chapter 4, the same methods are applied to quantify mitochondrial membrane potential and trafficking throughout the whole time course of de- and remyelination, capturing states of conduction block, early micro-saltatory conduction, and return to normal conduction. In order to embed the finding in the context of earlier work, the time course of de- and remyelination in the saphenous nerve is mapped out both anatomically using semi-thin resin sections and functionally via electrophysiological recordings of evoked compound action potentials. Chapters 5 and 6 investigate potential mechanisms underlying the findings in chapter 4: the effects of drug-induced conduction block are measured and intra-axonal calcium is quantified and compared between myelinated and demyelinated axons. Chapter 7 concludes with a general discussion of all findings.

It is my hope that taken together, these experiments help tease apart and better understand the different aspects of demyelination and their effects on mitochondria.

CHAPTER 2: PILOT STUDY - MITOCHONDRIAL DYNAMICS IN LYSOLECITHIN-MEDIATED DEMYELINATION ON DAY 7

INTRODUCTION

I began the investigation of mitochondrial dynamics in demyelination by conducting a pilot study. The goal of this preliminary investigation was to establish a demyelination protocol, develop an initial version of the tools needed to quantify mitochondrial trafficking, and investigate mitochondrial dynamics at a single time point during demyelination to establish whether it was affected by demyelination at all. Many aspects of this pilot study were improved and elaborated upon later (see especially chapters 3 and 4). Where this is the case I will limit myself to a short description here and refer to later chapters for more detail.

CHOICE OF DEMYELINATING AGENT

The first step in any study of demyelination is to choose an appropriate method of demyelination. Broadly, there are three ways of inducing demyelination: inflammation, genetic manipulations which cause demyelination and the application of demyelinating agents.

Inflammation-induced demyelination plays an important role in diseases such as multiple sclerosis or Guillain-Barré syndrome. However, inflammation is a complex process with wide-ranging effects from changes in local blood flow and oxygen supply (e.g. Andrew L Davies et al. 2013) to the release of cytokines and reactive oxygen species (Cross et al. 1998) by immune cells. The latter have been shown to have a direct effect on mitochondrial function (Nikić et al. 2011) and trafficking (Rintoul et al. 2006; Sorbara et al. 2014), as well at axonal integrity (Kapoor et al. 2003). This makes it hard to untangle inflammation-mediated mitochondrial changes from those caused by demyelination.

Genetic methods can be used to specifically mimic human diseases (see e.g. Fledrich et al. 2012 for an overview of the many available mouse models of the demyelinating form of Charcot-Marie-Tooth) or to very specifically target a single cell type. Two examples of the latter are the expression of the diphtheria toxin receptor in oligodendrocytes followed by the injection of small doses of the toxin (Buch et al. 2005; Locatelli et al. 2012) and even the direct expression of the diphtheria toxin A subunit controlled by tamoxifen injection (Traka et al. 2010; Traka et al. 2016). These approaches enable "clean" demyelination with little damage to other cell types and have been successfully used to study e.g. the effect of myelin debris on the acquired immune system. However, they are also expensive and difficult to combine with other genetic tools such as labelling of mitochondria or calcium indicators.

Alternatively, there is a collection of toxins which have been used to induce demyelination. Examples include the copper chelator cuprizone (Matsushima & Morell 2001), ethidium bromide (Black et al. 2006), anti-galactocerebroside antibody and complement (Mutsaers & Carroll 1998), the calcium ionophore ionomycin (Smith & Hall 1988), and lysolecithin (Hall & Gregson 1971). Of these, ethidium bromide and lysolecithin seem most appropriate for the purposes of this study, as they can both be topically applied to nerves and can cause reliable demyelination without overt damage to axons (Woodruff & Franklin 1999).

Ethidium bromide (EB) is a DNA chelator which binds to both DNA and RNA and thereby disrupts protein synthesis. It has been used extensively in studies of demyelination where it was reported to cause less axonal damage than LPC (Blakemore 1982; Woodruff & Franklin 1999). However, very early on the were reports of mitochondria abnormalities in the affected cells (Yajima & Suzuki 1979; Blakemore 1982). Since then, EB has been shown to reduce drastically the content of mitochondrial DNA in cells (Leibowitz 1971; Desjardins et al. 1985) and interfere with oxidative phosphorylation (Hayashi et al. 1990), which complicates any subsequent measurements of mitochondrial function.

Lysolecithin (LPC) is a lipid with detergent properties which has been used extensively both *in vivo* (Hall & Gregson 1971; Smith & Hall 1980; Bieber et al. 2002) and *in vitro* (Birgbauer et al. 2004). The exact mechanism by which LPC induces demyelination is not known. It has been suggested that it damages myelin as well as other lipid membranes because of its detergent properties (Hall & Gregson 1971; Birgbauer et al. 2004), however stronger detergents were found to cause no demyelination (Low et al. 1983). Instead, the effects of LPC on myelin may be more specific, for example through binding to myelin basic protein (Hughes et al. 1982; Smith 1982) which would also explain why axons and Schwann cell somata in LPC lesions do not to take up the tracer ferritin and are therefore believed to have an intact cell membrane (Hall & Gregson 1971). Alternatively, it has been suggested that lysolecithin and its conversion product lysophosphatidic acid activate G-protein coupled receptors (Xu 2002) and MAP kinase pathways (Bassa et al. 1999; Jing et al. 2000) and thereby induce apoptosis. However, this theory is at odds with multiple findings of low doses of LPC destroying the myelin surrounding axons while leaving cell bodies - including those of the myelinating cells - intact (Hall & Gregson 1971; Griffin et al. 1990; Woodruff & Franklin 1999). Cell bodies might also be protected from excessive damage because of their ability to break down LPC via the enzymes lysophospholipase and LPC-acyltransferase (Low et al. 1983). This theory is also supported by findings by Hall and Gregson showing that inhibition of the oxidative metabolism through cyanide and therefore cessation of enzymatic activity including (but obviously not limited to) acylation of LPC leads to widespread damage of Schwann cells and axons by LPC which is not seen in the absence of cyanide (Gregson & Hall 1973). Because of these enzymatic reactions, the biological half-life of LPC *in vivo* is believed to be very short.

Due to the interference of EB with mitochondrial function, LPC was chosen as the demyelinating agent for most experiments in this thesis, with the exception of an EB control experiment (see Appendix C).

Axonal damage in LPC mediated demyelination was repeatedly found to be low (Hall & Gregson 1971; Smith & Hall 1980; Woodruff & Franklin 1999; Wallace et al. 2003) but increasing with concentration. At the same time, the length of the demyelinated section

increases with higher concentrations. Hence, an appropriate dose was established in the pilot study.

In order to avoid injecting LPC solution into the small saphenous nerve, the agent was applied topically as described previously (Griffin et al. 1990; Wallace et al. 2003). The resulting demyelination was assessed in two different ways: firstly, by using the lipophilic fluorescent dye FluoroMyelin (Monsma & Brown 2012) for its ease of use and in the hope that it might be applicable later during *in vivo* imaging, and secondly in a more traditional fashion using toluidine-blue stained semi-thin resin sections.

DEMYELINATION AND AXON PHYSIOLOGY ON DAY 7

The cycle of de- and remyelination after lysolecithin application in the peripheral nervous system is quite fast with remyelination of virtually every affected axon after three weeks (Hall & Gregson 1971; Smith & Hall 1980). Along with the changes in myelination, axons in LPC lesions undergo changes in physiology from (in order of time) conduction block to abnormal, micro-saltatory conduction, to restored near-normal conduction (Smith et al. 1979; Smith & Hall 1980; Smith et al. 1982). For the pilot study, day 7 after the surgery to induce demyelination was chosen since at this time point demyelination is well established and the myelin debris has been largely cleared (Hall & Gregson 1971), but axons are still in the phase of conduction block (Smith & Hall 1980). For a detailed discussion of the time course of demyelination, see Chapter 4.

ANIMALS

Ex vivo assessment of demyelination was carried out using male C57Bl/6J wildtype mice. The animals were acquired from Charles River at an age of 6 to 8 weeks and left to acclimatise to their new environments for at least 7 days after arrival.

Mice used for mitochondrial imaging were male, heterozygous, Thy1-CFP-S positive (main study) or Thy1-CFP-S positive and negative (pilot study) littermates (Jackson laboratories strain designation: B6.Cg-Tg(Thy1-CFP/COX8A)S2Lich/J) (Mito-S). Mice were bred in-house and had been back-crossed to C57Bl/6J for at least three generations. Mito-S mice selectively express cyan fluorescent protein (CFP) under the mouse thymus cell antigen 1, theta (Thy1) promotor which is localized to the mitochondrial inner membrane by a human cytochrome c oxidase subunit 8A targeting signal (Misgeld et al. 2007). Mitochondrial physiology and morphology were reported to be normal in heterozygous animals (Misgeld et al. 2007) which has led to a widespread use of this mouse line in mitochondrial research (e.g. Bilsland et al. 2010; Nikić et al. 2011; Sajic et al. 2013; Sorbara et al. 2014). However, it should be noted that some homozygotes develop a tremor in adult life (Misgeld et al. 2007, supplementary). We found that CFP is expressed in approximately 30-50% of all myelinated saphenous nerve axons where it can be detected with roughly equal intensity in all mitochondria. Unmyelinated C-fibres, in contrast, do not appear to express CFP.

The age of all mice commonly ranged from 8 to 12 weeks, never exceeding 16, and care was taken to ensure that treatment and control groups were age-matched and wherever possible litter mates.

All animal experiments were carried out according to the 1986 Animals (Scientific Procedures) Act, UK, and were approved by the institutional ethics committee.

DEMYELINATION PROCEDURE

Animals were anaesthetized using isoflurane (5% induction, 1-2% during surgery) and placed on a heating mat connected to a temperature control unit. At the beginning of the surgery they were injected with 10µl Vetergesic s.c. (0.3mg/ml, Alstoe Animal Health) to ensure adequate analgesia after recovery. Subsequently, the hair was removed from the inside of the leg using clippers and hair removal cream, and the skin was sterilized with iodine and sterile ethanol wipes. An incision was made at the thigh, exposing approximately 1 cm of the saphenous nerve. Connective tissue and fat were carefully removed from the top of the nerve without damaging the perineurium. Lysolecithin (L4129, Sigma) was diluted in sterile physiological saline (0.5%, 1%, 2% for dose assessment, 1% or pure saline for all subsequent experiments), vortexed for at least 20 minutes, and applied topically to the nerve, using the surrounding skin as a well. It was held in place for 20 minutes and topped up if necessary to keep the tissue from drying (usually one top-up of 1-2 drops, never more than two top-ups). For control animals, the same procedure was conducted with sterile saline instead of LPC. After 20 min, the opening was washed thoroughly with saline and the skin sutured shut with 2-4 sutures of 6-0 polypropylene thread (Ethicon). Animals were observed for at least 1h post-surgery and daily afterwards. The surgery was well tolerated and complete recovery was seen within a couple of hours. Where necessary, sutures were removed after seven days.

SEMI-THIN RESIN SECTIONS

At the desired time points after treatment, animals were anaesthetized using isoflurane (3%) and euthanized via cardiac perfusion with heparinised buffered saline followed by a mixture of 4% paraformaldehyde (PFA) and 2% glutaraldehyde in phosphate buffered saline (PBS). Approximately 5mm of each nerve (two per animal) was harvested and post fixed overnight in 4% glutaraldehyde. Afterwards, the tissue was washed (3x10 min; 0.1 M PO4 buffer; pH 7.4), post-fixed in osmium tetroxide (1.5%) for 1h, washed again (3x10 min; 0.1 M PO4 buffer; pH 7.4), dehydrated in an ascending series of ethanol (30%, 50%, 70%, 90%, 3x100%; 20min each) and passed via propylene oxide into resin (TAAB

Laboratories, Aldermaston, UK) where it was left overnight. Subsequently, the nerve fragments were embedded in coffin moulds in fresh resin and heated at 60^{o}C for 48 hours. 0.7μm thick transverse sections were cut from the middle part of each specimen using an ultramicrotome (Reichert Ultracut S, Leica), stained with toluidine blue and examined and photographed using a Zeiss Axiophot microscope equipped with a Nikon D300 camera (Nikon, USA).

Images were processed using Fiji/ImageJ Version 1.48. Photographs of resin sections were converted to grayscale and contrast was optimised for each image such that the image's histogram covered the whole range of grey levels.

ASSESSMENT OF DEMYELINATION

Animals and treatments per experiment were as follows: first, mice (n=2 per group, n=8 total) were treated with 0.5%, 1%, or 2% LPC or saline applied to the saphenous nerve of their left leg and prepared for imaging as described below 7 days later. The lipophilic fluorescent dye FluoroMyelin Green (FlM, life technologies) was diluted 1:25 in physiological saline and applied to the desheathed nerve either on its own for 30 min or in combination with 0.5μM TMRM for 45 min. Residual dye was washed off. A well made of petroleum jelly was formed around the surgical opening, and the opening was covered with a glass coverslip. Imaging was performed using an LSM Pascal 5.0 confocal microscope (Zeiss) and a Zeiss Appochromat Plan 63x oil objective (NA 1.4).

Subsequently, 4 animals (n=2 per group) were treated with either 1% or 2% LPC applied to their left saphenous nerve, with saline applied to the right nerve as a control. The animals were perfused and nerves were harvested after 7 days and processed into resin as described above.

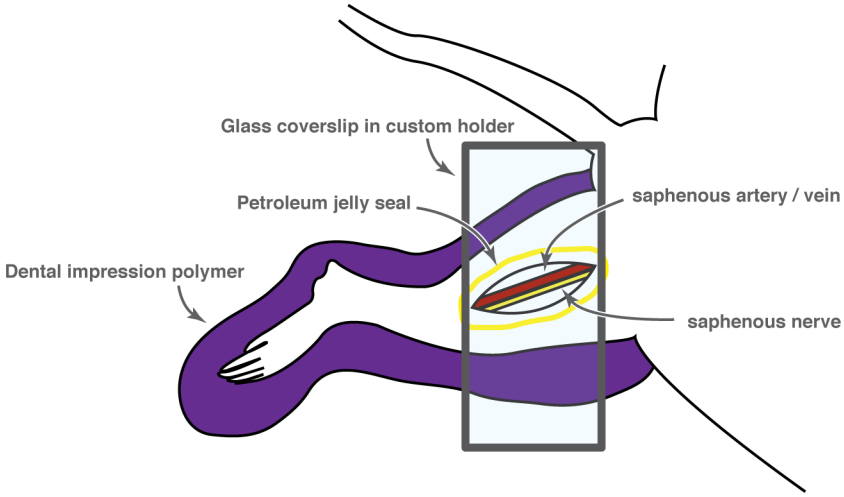

Figure 2.1: **Sketch of the imaging setup**. Animal placed in supine position and viewed from above.

Mito-S mice underwent demyelination or control treatment (n=4 sham surgery, n=5 LPC treatment) and after 7 days were prepared for imaging as described above. In addition, another n=4 naïve animals were imaged without any treatment.

Animals were injected with 2g/kg urethane (Sigma, diluted 20% w/v in sterile saline) and, 10 minutes later, with a small dose of 20mg/kg ketamine (Ketaset, Fort Dodge, diluted to 10mg/ml). This anaesthetic combination enabled stable, long term anaesthesia with a significantly accelerated onset compared with urethane alone (see also: Klausberger et al. 2003; Moldestad et al. 2009; Molden et al. 2013). Toe pinch reflexes were checked regularly and, if necessary, additional urethane was added. Surgical depth of anaesthesia was reached after about 15 minutes at which point the hair was removed from the inside of the leg using clippers and hair removal cream. Mice were placed in a supine position on a heating mat connected to a temperature control unit and mounted on a customized stage. Additional heating was provided via an electrically grounded heating lamp.

The left leg was immobilized using a dental impression polymer (Examix NDS Monophase Purple, GC America) (Misgeld et al. 2007; Haney et al. 2008). An incision was made at

the thigh, exposing approximately 1 cm of the saphenous nerve. Connective tissue and fat were carefully removed from the top of the nerve. Using a tungsten needle, a small hole was produced in the perineurium, following which the nerve was desheathed carefully using Vannas scissors. In order to keep the tissue from drying, sterile saline was applied whenever necessary. After the surgery was completed, TMRM was applied at a concentration of 0.5μM in sterile saline for 45 minutes after which the residual dye was washed off (Sajic et al. 2013). Subsequently, a well made of petroleum jelly was formed around the surgical opening, fresh saline was applied, and the leg was covered with a glass coverslip. The animal was transferred to the custom made stage of an LSM Pascal 5.0 confocal microscope (Zeiss). Images were taken using either a Zeiss Appochromat 10x objective (NA 0.3; overview tiles only) or a Zeiss Appochromat Plan 63x oil objective (NA 1.4).

A pixel size of 0.16μm was chosen to satisfy the Nyquist sampling criterion for small particles (Petty 2007) and to improve segmentation performance (Jaqaman & Danuser 2009). The pinhole size was set to 1.2 AU and time lapses were recorded at 1 frame/sec for 65 seconds. Successive dual colour CFP / TMRM images were taken to help distinguish axonal mitochondria from mitochondria found in other cells. However, time lapses were based on the TMRM signal alone because of its superior contrast and prohibitive bleaching caused by repeated CFP imaging.

FluoroMyelin, while useful to assess demyelination in LPC dose calibration, was found to have a very broad emission spectrum which overlapped with both CFP and TMRM and which rendered it unsuitable for use in mitochondrial imaging. For time lapse recordings, myelination was thus assessed via the presence or absence of a red 'border' around axons caused by TMRM in the myelin layers.

IMAGE ANALYSIS AND STATISTICS

Recordings of mitochondrial movement were originally analysed using an early version of the methods described in chapter 3. For consistency, and because the latest version of

the analysis scripts has been more stringently tested, results presented here have been re-analysed using the same methods as described in chapter 3. Briefly, videos were segmented frame by frame using the Squassh algorithm (Rizk et al. 2014) in combination with point spread functions acquired using the same settings as during recording. Particles were then split and classified as either static or moving using custom made Matlab scripts, and tracked using the Matlab package uTrack 2.1.3 (Jaqaman et al. 2008) with custom cost matrices. Note that in contrast to all subsequent experiments, CFP fluorescence was not recorded and thus no relative TMRM intensity was measured.

Similarly, statistical analysis, which was originally done using a naïve approach (see Appendix A) was re-done using a nested approach. Where possible, conditions were compared on an axon-by-axon basis. Using the *nlme* package for R, a two-level linear model with a fixed slope and random intercepts was fitted to the data. The variable of interest (e.g. average speed of mitochondria) per axon was used as the response variable, treatment/day as a fixed effect, and animal ID as a random effect. Multiple comparisons were corrected using Tukey correction. Probability density estimates were calculated using Matlab's ksdensity function with a normal kernel. Corresponding confidence intervals were estimated via Bootstrapping using 10,000 repeated draws of the same sample size as the original distribution. The 95% confidence interval for cumulative distribution functions was estimated using Greenwood's Formula.

RESULTS

LYSOLECITHIN DOSE ASSESSMENT

The use of FluoroMyelin green resulted in crisp images of myelinated axons with the nodes of Ranvier clearly visible. The pathology appeared comparable to pictures taken using incident light microscopy (for comparison, see e.g. Hall & Gregson 1971 figures 2,3), and the quality approached that of longitudinal resin sections.

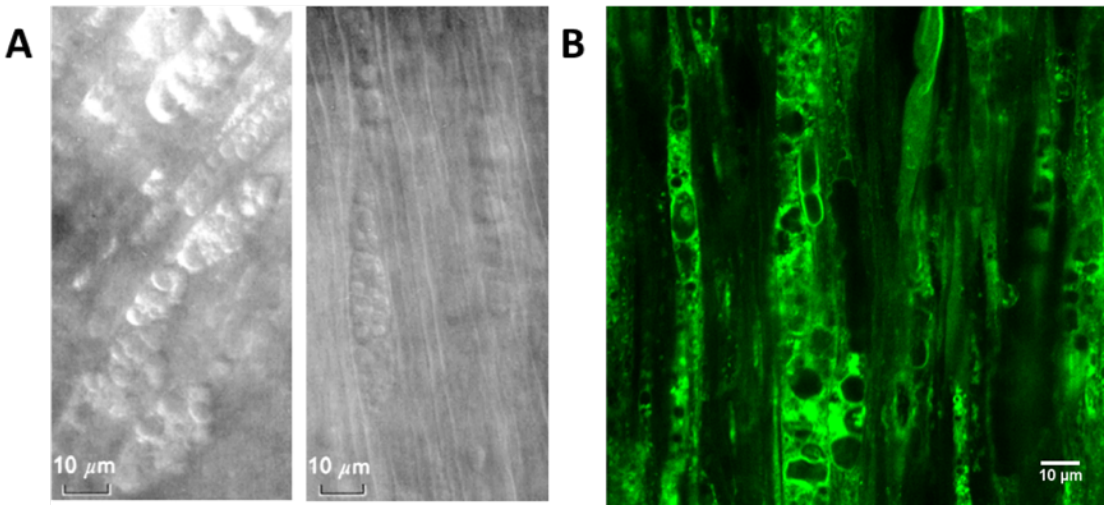

Figure 2.2: **Comparison of incident light microscopy and confocal imaging using FluoroMyelin Green in vivo**. **A**: Incident light images taken 6 days after injection of 1% LPC into the mouse sciatic nerve (Hall & Gregson 1971 figures 2,3) **B**: Saphenous nerve stained with FluoroMyelin Green and imaged on a confocal microscope 7 days after topical application of 2% LPC.

In saline-treated animals, axons lay in parallel and they were close to each other. A few severed axons could be seen, but they were found mostly where the perineurium was first opened, suggesting damage during the imaging surgery rather than during treatment. Where TMRM was used, mitochondria were found to be restricted largely to the axoplasm with some TMRM positive particles found in the myelin close to the nodes. Overall, the nerve fibres took up the vast majority of space and only remarkably few other cells were visible in any given field of view (Figure 2.3). Rarely, this included mobile macrophages which were usually clearly identifiable in experiments involving TMRM due to their cell shape, bright mitochondria and movement patterns, but were usually absent from preparations, including those with clear signs of demyelination.

Nerves treated with LPC reliably showed signs of myelin disturbance which increased in a dose-dependent manner (Figure 2.4). In the case of 0.5% LPC the disturbance was largely restricted to a less-smooth appearance of the sheath. Axons still lay in parallel and in close proximity to one another. Nerves treated with 1% or 2% LPC showed much stronger signs of myelin damage with fewer axons visible per field of view. Instead, long, oval fields of debris very similar to the ones described by Hall and Gregson using incident

light microscopy could be seen between axons (Figure 2.2). The fluorescent signal appeared less crisp, individual axons were harder to make out, and nodes of Ranvier were rarely, if ever, seen. Importantly, where demyelination was visible it appeared to extend deeper into the nerve than was possible to image using the available confocal setup, suggesting that doses higher than 2% or a treatment for longer than 20min were not necessary for *in vivo* imaging. Based on these observations 1% and 2% LPC were selected as doses for a more detailed investigation using transverse resin sections.

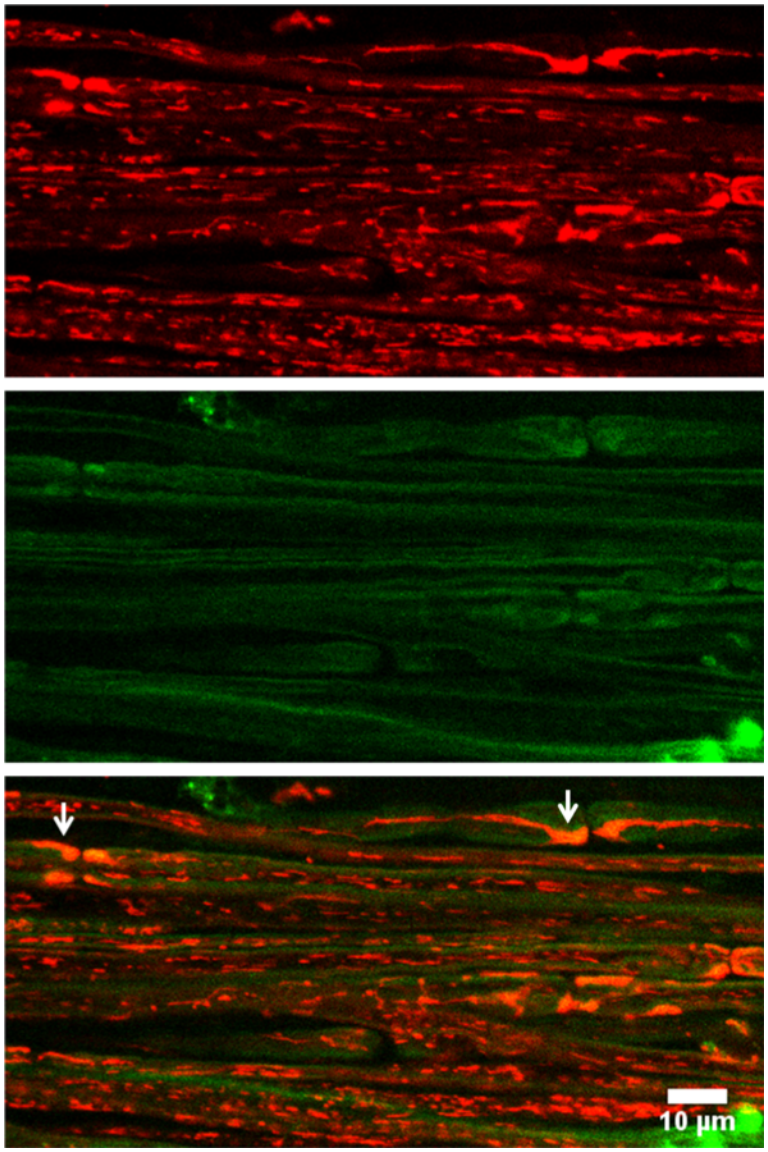

Figure 2.3: **Dual colour *in vivo* imaging of FluoroMyelin (green) and TMRM in a saline treated animal**. **Top**: Mitochondria indicated by TMRM. **Middle**: FluoroMyelin Green signal. **Bottom**: Merged. Note the accumulation of non-axonal mitochondria near the nodes (**arrows**).

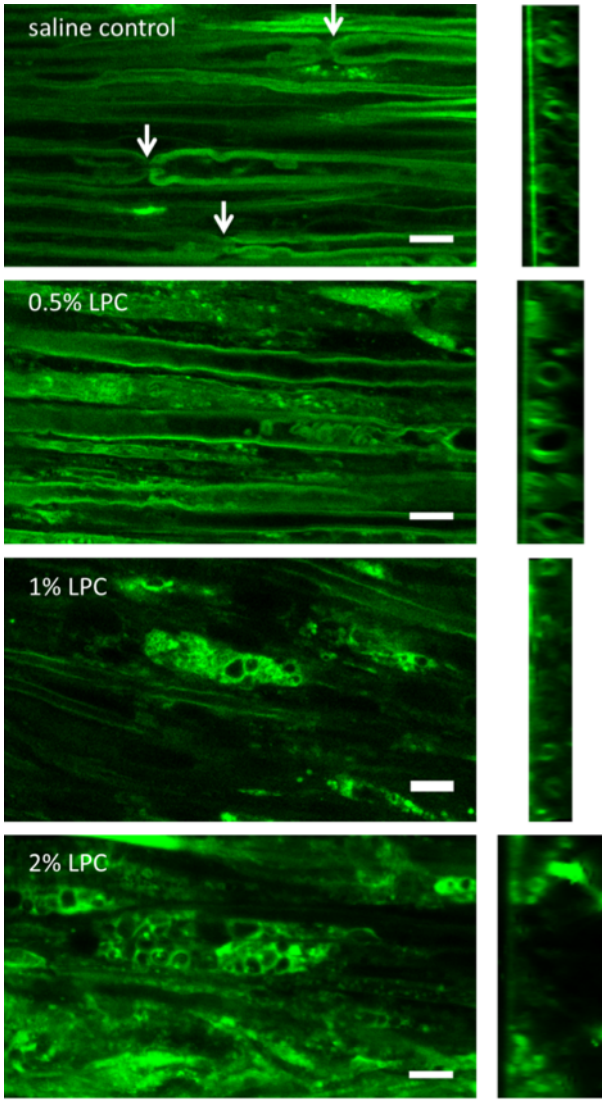

Figure 2.4: **Examples of FluoroMyelin imaging after application of LPC**. **Left side**: Saphenous nerve imaged from above 7 days after topical application of different doses of LPC. **Right side**: Corresponding transverse sections recreated from Z stacks. **Arrows** indicate nodes of Ranvier.

The first important histological finding was that sham procedures did not cause any signs of demyelination or damage to the axons (Figure 2.5). Application of LPC produced signs of demyelination in three out of four nerves (2x 1%, 1x 2%). In all cases, axons could be found near the top of the nerve which appeared to be surrounded by very little or no myelin. Many of them were associated with cells. Very rarely, dystrophic axons (characterized by dark, granular appearing axoplasm) could be spotted. The area in which these changes could be observed covered approximately 10%-30% of the nerve's cross section. While the previous set of FluoroMyelin experiments suggested increased demyelination in 2% LPC treated animals compared with 1% LPC treated animals, this relationship was not replicated histologically. The two nerves treated with 1% LPC showed at least as many signs of demyelination as the first animal treated with 2% LPC.

No demyelination was found in the second nerve treated with 2% LPC. However, the corresponding control nerve was damaged during processing, and it is possible that the two pieces of tissue were swapped. Given that the experiment revealed no obvious reason to favour 2% LPC over 1% LPC, I decided to use the lower concentration for all subsequent experiments.

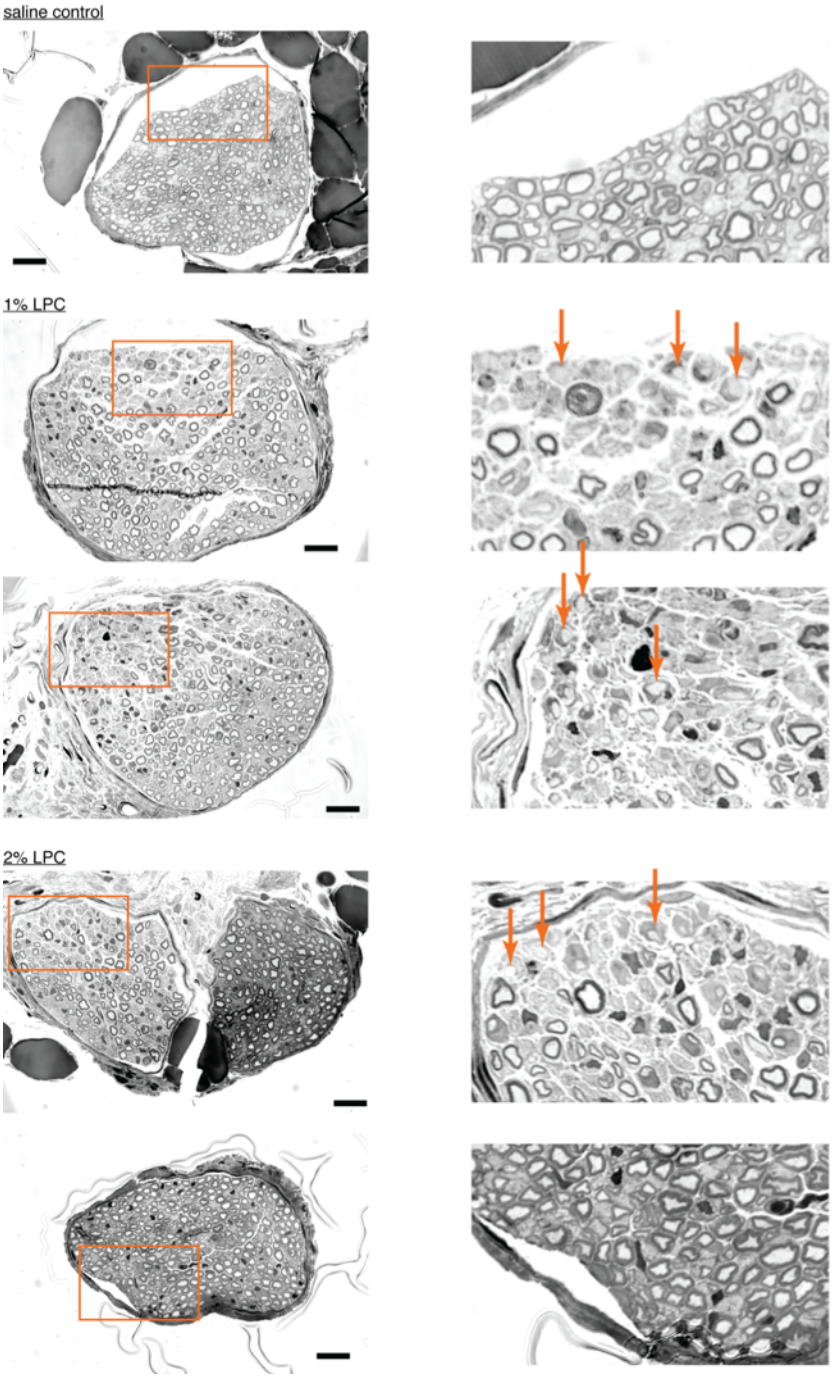

Figure 2.5: **Semi-thin transverse resin sections of the saphenous nerve on d7 after topical application of 1% LPC, 2% LPC or saline**. Scale bars on the left indicate 20μM; orange rectangles indicate the original locations of the magnification seen on the right. Arrows indicate demyelinated axons, often with associated cells. See text for details and Figure 4.2 for comparison.

MITOCHONDRIAL DYNAMICS IN MYELINATED AND DEMYELINATED AXONS

Myelinated and demyelinated axons could be clearly distinguished even though FluoroMyelin was not used in this series of experiments because of bleed-through into the TMRM signal. While myelinated axons were surrounded by thin, visible borders (likely due to some TMRM uptake into the myelin), the only visible part of demyelinated fibres was often a string of mitochondria. The genetically encoded CFP signal was helpful in revealing axonal damage which appeared more widespread than suggested by the transverse resin sections: about one in ten axons on the nerve surface presented with TMRM negative mitochondria, indicating a lack of $\Delta\psi m$ and/or $\Delta\psi p$ (Figure 2.6). Such damage was very rarely seen in naïve or sham operated animals. Mitochondrial polarisation appeared uniform within axons, that is either all or none of the mitochondria of a given axon seemed to be polarised. No movement of CFP-positive, TMRM-negative mitochondria was observed and axons with depolarised mitochondria were discarded from further analysis.

As reported above, few cells could be seen between the axons in naïve and sham-treated animals. In LPC preparations, non-neuronal cells associated with axons could be seen as well as large, debris-laden cells in between nerve fibres. Here, the CFP signal was useful for telling axonal and non-axonal mitochondria apart. Mobile macrophages were virtually absent from all preparations.

Of all data collected during the pilot study, 270 recordings of individual axons were found to be stable enough for analysis: 84 axons from naive animals, 119 axons from sham treated nerves and 67 demyelinated axons.

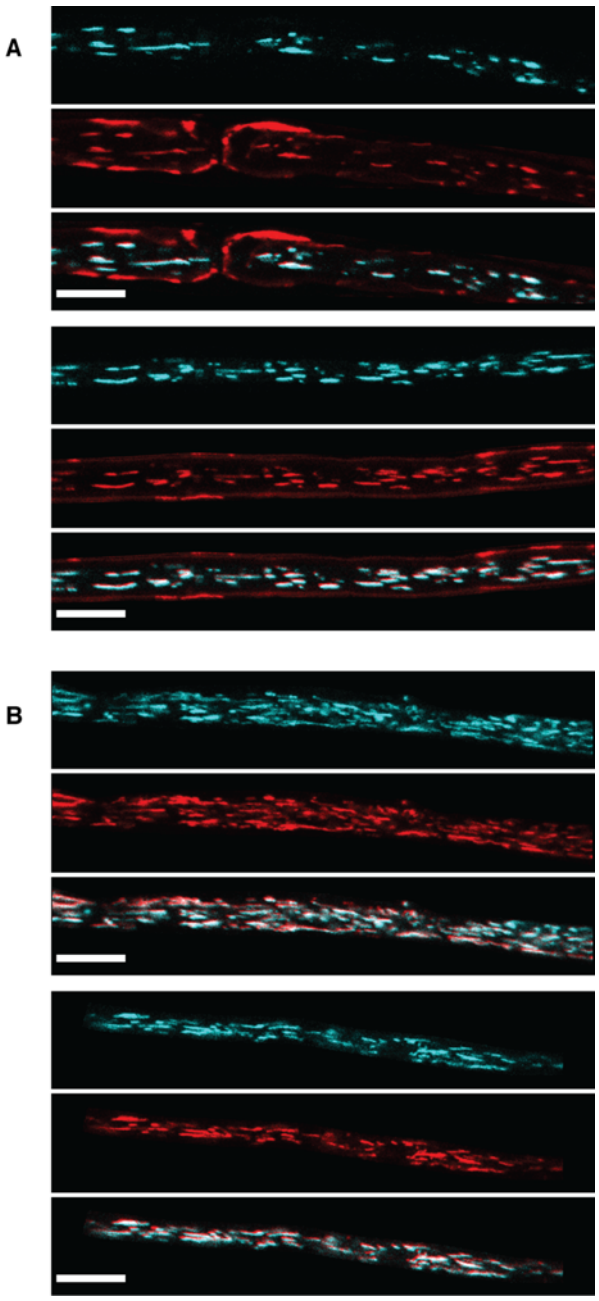

Figure 2.6: Examples of mitochondria in saphenous nerve axons, imaged *in vivo*: Genetically encoded CFP is shown in cyan, TMRM signal in red. Signal overlap appears white. **A**: Myelinated axons. Note the node of Ranvier in the top image and the red outline of the axons indicating the presence of myelin. **B**: Demyelinated axons 7 days after LPC treatment. Note the lack of a myelin border around the axons and the high density of mitochondria. Bars indicate 10μm.

Axon width was estimated as the width of the smallest rectangle around the straightened axon that could contain 98% of all mitochondrial pixels. Surprisingly, by this definition, demyelinated axons were found to be significantly wider than both naïve and sham

treated axons (mean width of naïve axons: 3.99µm ± 0.174µm SE; sham treated axons: 4.11µm ± 0.29µm, n.s.; demyelinated axons: 4.80µm ± 0.30µm, $p<0.01$ for both comparisons). Visual inspection showed that this was not caused by axonal swelling or beading; the demyelinated axons in question appeared straight and with a constant diameter. Nevertheless, mitochondrial density measured as percentage of the axoplasm slice covered by mitochondria was significantly increased from 11.25% ± 0.52% and 11.22% ± 0.87% for naives and sham treated animals, respectively to 17.39% ± 0.91% in demyelinated axons ($p<0.001$). This increase could be explained by both a larger number of stationary particles and a significantly increased size (see Figure 2.7 C). In contrast, moving particles were found to have comparable sizes in all three conditions (Figure 2.7 D). There was no difference in the size of anterogradely and retrogradely moving particles.

The main objective of the pilot study was to establish whether demyelination would cause a change in mitochondrial dynamics. Total transport was calculated as the average sum of all particle speeds in either direction. In order to account for differences in the number of frames (e.g. due to removal of frames where focus on the axon was lost) and length of the recorded axon, this value was normalised to an axon length of 100µm and a recording of 60 frames (= 60 seconds). Demyelinated axons showed a significant decrease in mitochondrial transport in both anterograde and retrograde direction. Anterograde transport fell by 74.0% (± 16.2% SE) compared with naives and 74.3% (± 16.0%) compared with sham treated animals ($p < 0.001$ for both). Retrograde transport was reduced by 68.4% ± 26.0% ($p < 0.05$) and 76.7% ± 19.2% ($p < 0.001$), respectively (Figure 2.8 A). A more detailed analysis revealed that this decrease in transport was due to both a lower speed of moving mitochondria (Figure 2.8 B), and a smaller number of mitochondria being transported (anterograde: on average 3.97 ± 0.43 tracks per frame vs 3.880 ± 0.711 tracks in saline treated axons and 1.30 ± 0.75 tracks per frame in demyelinated axons; retrograde: 0.52 ± 0.09 tracks per frame in naïve axons vs 0.71 ± 0.15 in saline treated axons and 0.17 ± 0.16 in demyelinated axons). Moving mitochondria were detected in all but 10 axons, nine of which were demyelinated, and one of which had undergone control treatment.

An interesting observation was that in all three conditions, retrograde transport was significantly lower than anterograde transport. In untreated axons, for example, anterograde transport on average accounted for 79% of all mitochondrial movement, which seemed to be largely due to a lower number of moving particles (see next chapter for a more detailed discussion of this phenomenon).

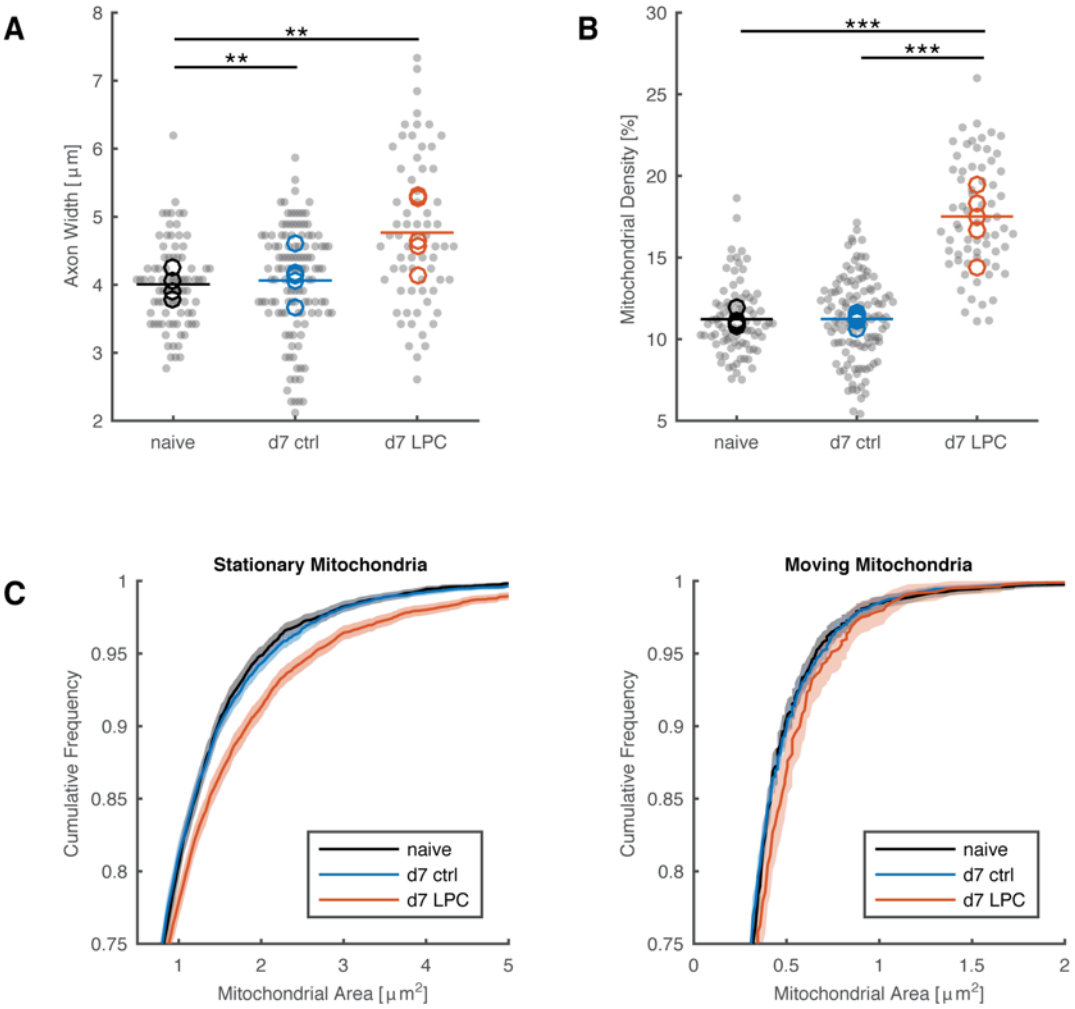

Figure 2.7: **Anatomical changes in demyelinated axons and their mitochondria**. **A**: Demyelinated axons were significantly wider. Grey dots indicate individual axons, lines indicate population means, and circles show the means of different animals. **B**: Mitochondrial density was significantly increased in demyelinated axons. **C**: Cumulative frequency plots of mitochondrial sizes. Both graphs show the largest 25% of all particles and their 95% confidence intervals.

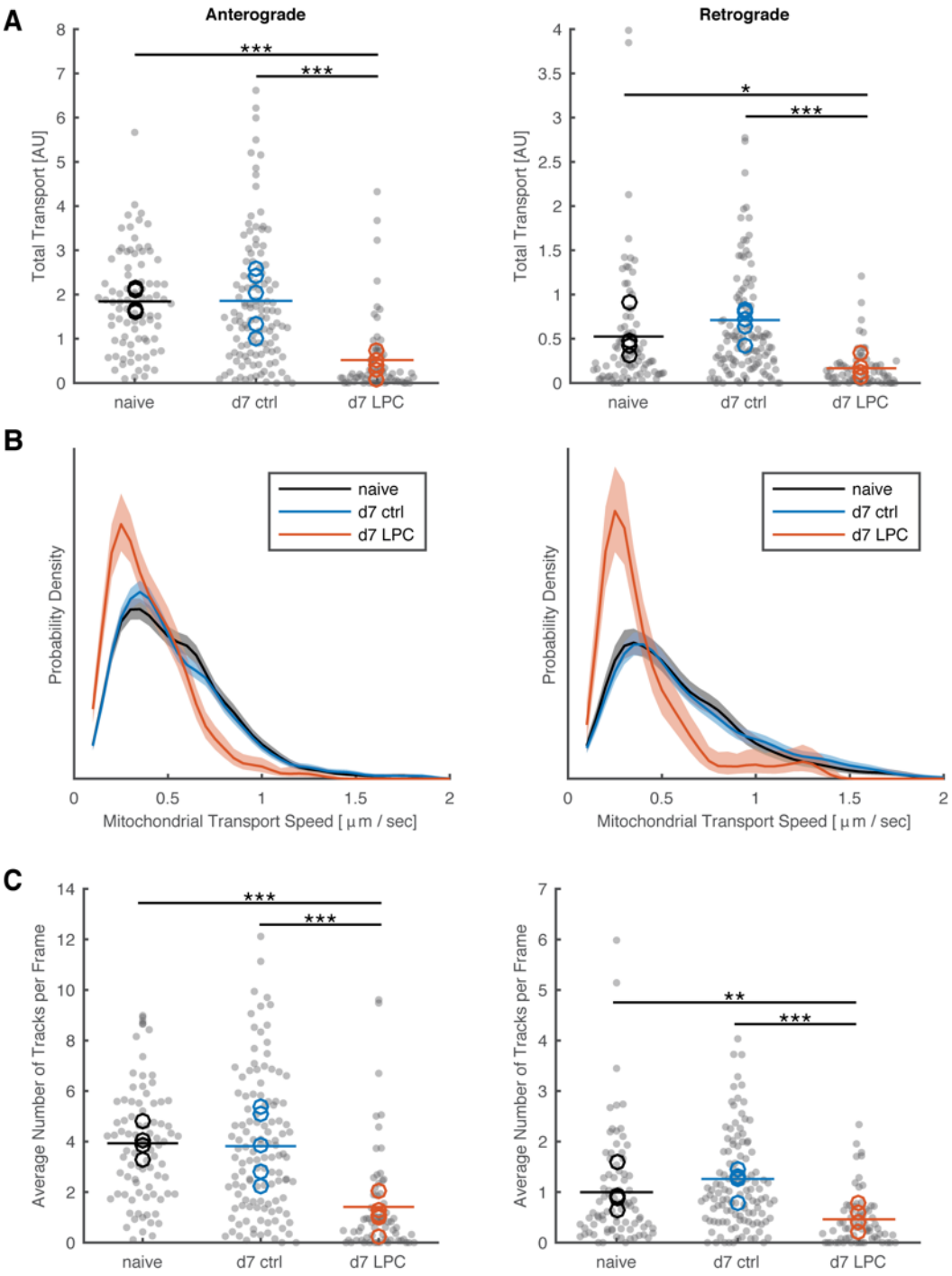

Figure 2.8: **Mitochondrial dynamics in demyelinated axons on day 7**. **A**: Total transport - average particle speed in either direction normalised to an axon of 100µm length and 60 seconds. Demyelinated axons present significantly decreased transport in both directions. Note the difference between anterograde and retrograde transport. Grey dots indicate individual axons, lines indicate population means, and circles show the means of different animals. **B**: Distribution of transport speeds for anterogradely and retrogradely moving mitochondria. Distributions for naïve and control treatment are nearly identical; mitochondria in demyelinated axons have reduced transport speeds. **C**: Average number of simultaneous tracks in either direction normalised to 100µm axon length. Fewer moving mitochondria are observed in demyelinated axons.

This pilot study yielded interesting results, encouraging further investigation of mitochondrial dynamics in demyelination.

A model of saphenous nerve demyelination by topical application of lysolecithin was successfully established and characterized. Care was taken to use the lowest LPC concentration possible in order to minimize axonal damage. I found that the application of 1% LPC for 20 minutes was sufficient for the purposes of this study, creating demyelination of the uppermost axons. This dose is slightly lower than doses used for topical application by other groups (Griffin et al. 1990; Wallace et al. 2003) but results appear similar. Wallace and colleagues, for example, describe demyelination of a maximum of 40% of axons in the saphenous nerve 13 days after topical application of 1.5% LPC (Wallace et al. 2003). Note that the efficacy of this method of demyelination significantly improved with practise, leading to a much larger number of demyelinated fibres (see chapter 4).

The naïve saphenous nerve contains a mixture of myelinated A fibres and unmyelinated C fibres with unmyelinated fibres outnumbering myelinated ones at a ratio of approximately 4:1 (Carter & Lisney 1987) which raises the question whether some of the observations may have been confounded by naturally unmyelinated fibres. However, I believe that this is unlikely for several reasons. The diameters of C fibres tend to be smaller than the diameter of A fibres by about an order of magnitude (Stucky et al. 2002) which makes it impossible to make out individual C fibre axoplasms *in vivo*. Furthermore, whilst myelinated fibres are evenly spaced across the nerve, C fibres are held closely together in so-called Remak bundles of usually >20 axons (Murinson & Griffin 2004) which branch and recombine regularly and contain large cell bodies between the individual axons. This gives them a foamy appearance in resin section as well as very distinct look *in vivo* (see Figure 2.9). Most importantly, C fibres do not seem to express the mitochondrially targeted CFP and were thus not selected for analysis.

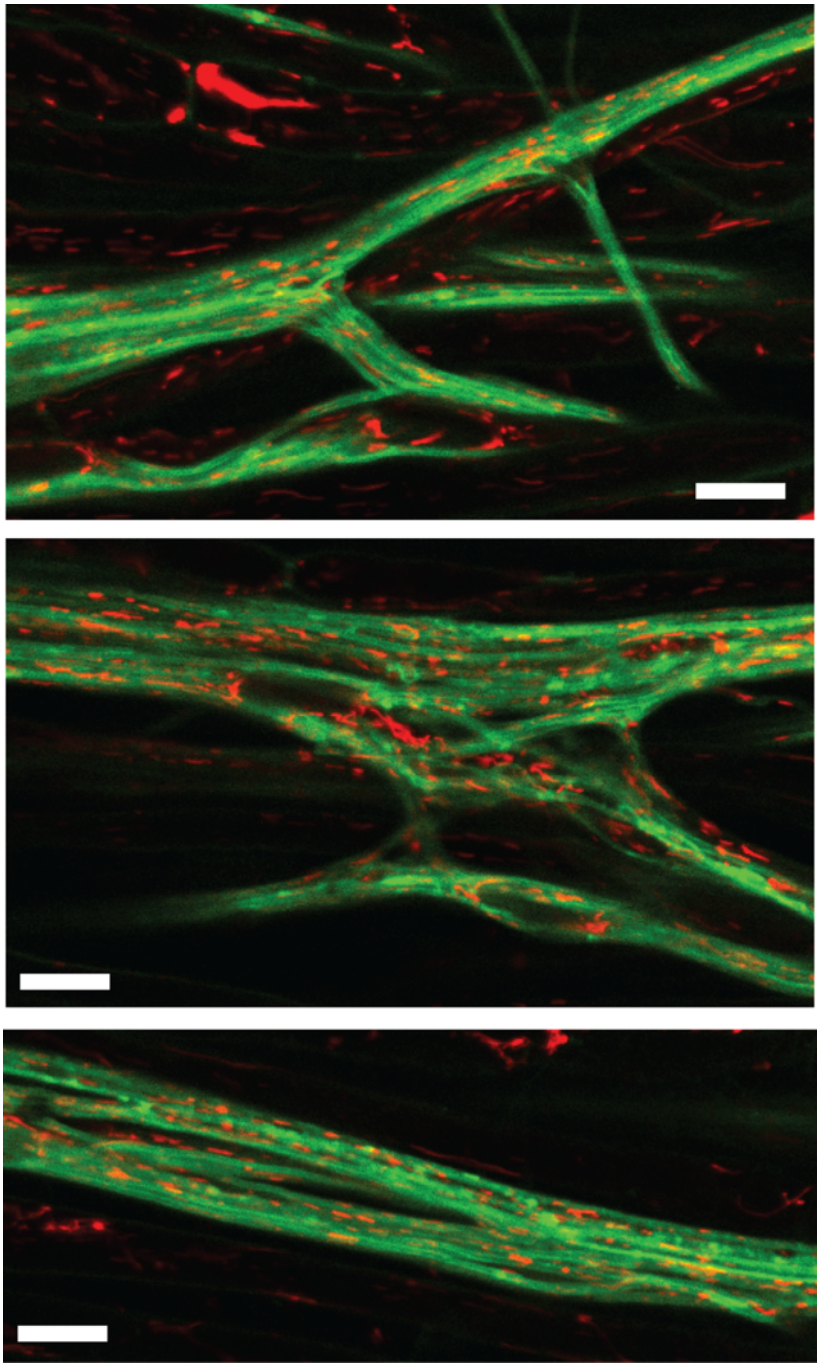

Figure 2.9: **C-Fibre bundles imaged *in vivo***. Bars indicate 10µm. See text for details.

In agreement with earlier reports of LPC-treated nerves (Hall & Gregson 1971) and demyelinating EAE (Raine et al. 1969), demyelinated axons appeared rounder and with a seemingly smaller diameter when looking at resin sections. However, this finding could not be replicated *in vivo* where, instead, axon diameter seemed significantly increased.

Whilst it is possible that this result was exacerbated by the way I estimated axon width *in vivo* (in naïve axons there is usually some space between mitochondria and the surrounding myelin which might get filled up with additional mitochondria in demyelinated axons) it nevertheless seems incompatible with the notion of a smaller diameter. This suggests that the decreased diameter reported previously might be a fixation artefact.

Using live imaging and semi-automated quantification of movement the consequences of demyelination on mitochondrial transport were successfully investigated. In agreement with earlier studies (Mutsaers & Carroll 1998; Hogan et al. 2009), a significant increase in mitochondrial density was found. While a direct comparison with the two studies is complicated (both authors look at nerve cross-sections using electron microscopy), the 1.55-fold increase in density found here lies slightly below the density increases found by Hogan et al. (1.7x) and Mutsaers & Carroll (2.36x). However, this discrepancy might be explained by two factors. Firstly, when looking at the axon *in vivo*, distinct mitochondria may overlap, making their cumulative area seam smaller than is really appropriate. Secondly, since measurements in the pilot study were performed based on TMRM images, it is possible that some of the mitochondria identified in untreated axons were in fact located in the myelin sheath (see also Gonzalez et al. 2015 in which only mitochondria in the myelin sheaths surrounding the saphenous nerve are visualised). This could have led to an overestimation of mitochondrial density in myelinated axons and hence an underestimation of the change compared with demyelinated axons. However, the increase in mitochondrial density measured in the time series experiments described in chapter 4 which was calculated using CFP images was found to be almost exactly the same (1.60x on day 8), making this an unlikely explanation. While overall there were significantly more large mitochondria in demyelinated axons it should be noted that about 75% of all static particles in demyelinated axons were no bigger than those in myelinated axons, and well within the size range of moving mitochondria. An increase in size therefore does not appear to be the main cause of reduced mitochondrial transport.

Compared with a related study of mitochondrial dynamics in the saphenous nerve previously conducted in the lab (Sajic et al. 2013), the velocities found in the pilot study

were slightly higher (e.g. 0.53µm/s vs 0.30µm/s for anterograde movement in axons of naïve animals). Furthermore, the average size of moving particles was found to be slightly smaller. Since the study at hand used a 50% higher spatial resolution and a 100% higher time resolution, it is possible that more small and fast particles were detected, thus explaining the discrepancy. This explanation is also supported by the fact that the average number of tracks identified here was 19 over 60 seconds, in contrast to an average of 3 tracks over 98.5s found previously (Sajic et al. 2013) (both in naïve animals and spanning 6 or more frames).

An interesting phenomenon which is not related to demyelination *per se* is the significant difference between anterograde and retrograde mitochondrial transport observed in all groups. This phenomenon, although not fully understood, is well-described in the *in vivo* literature (Andrews et al. 2010; Zhang et al. 2010; Kiryu-Seo et al. 2010; Bilsland et al. 2010; Sajic et al. 2013) and I was able to successfully replicated it using the improved methodology described in chapter 3. It is discussed in more detail there.

Most importantly, I detected a highly significant decrease in mitochondrial transport due to demyelination. This finding is particularly interesting because it stands in obvious contrast to findings of demyelination causing increased mitochondrial transport *in vitro* (Kiryu-Seo et al. 2010; Ohno et al. 2014). As laid out in chapter 1, it could also be of clinical significance since mitochondrial transport is believed to be essential for mitochondrial maintenance. When writing up the findings of the pilot study, I speculated that whilst likely helpful in the short term (see Ohno et al. 2014), the local accumulation of mitochondria might be harmful for the long-term survival of the axon if it meant a decrease in mitochondrial transport and exchange of material. I was thus particularly intrigued by a recent paper by Joshi and colleagues showing that the knockout of the mitochondrial anchoring protein syntaphilin in dysmyelinating *shiverer* mice was in fact protective and prolonged the animal's survival (Joshi et al. 2015). The study is discussed in more detail in chapter 7.

At this point it was not clear what the cause of the decrease of transport might be. Previous studies suggested that in the majority of axons conduction should not have

returned by day 7, but given the slightly different methodology used here it was conceivable that the time courses might be different and the increase in mitochondrial density was indeed a reaction to heightened ATP demand. To investigate this possibility, I decided to map the whole time course of de- and remyelination in anatomical and electrophysiological terms and determine mitochondrial dynamics and function at multiple time points throughout. The results are described in chapter 4.

The decrease in mitochondrial trafficking found in this study has one potential caveat: in situations of high mitochondrial density it is more challenging to track moving mitochondria accurately than in axons with fewer stationary particles. This particular problem is addressed in chapter 3, which explains my general approach to particle tracking in more detail and investigates the connection between mitochondrial density and observed transport in naïve animals, as well as in chapter 4 which contains analyses on mitochondrial transport for various densities of stationary mitochondria.

As a result of this study, I also introduced several methodological changes. Firstly, instead of using sterile saline to surround the desheathed nerve during surgery and imaging, I decided to use artificial cerebrospinal fluid. I introduced this change because of the well-known influence which calcium has on mitochondrial trafficking and because of studies showing significant effects on mitochondrial transport caused by using calcium free media *in vitro* (Zhang et al. 2010). Secondly, thanks to a microscope upgrade, I was able to record mitochondrial trafficking using simultaneous CFP and TMRM imaging. This development had two major advantages: it enabled me to separate clearly axonal mitochondria from Schwann cell mitochondria (compare Gonzalez et al. 2015) and it formed the basis for measuring TMRM intensity.

In conclusion, the study of mitochondrial dynamics in demyelinated axons on day 7 after the application of LPC confirmed previous findings of a higher density of stationary mitochondria, and furthermore it revealed a highly significant decrease in mitochondrial trafficking. The result motivated me to investigate further the relationship between demyelination and mitochondria.

CHAPTER 3: MEASURING MITOCHONDRIAL TRANSPORT AND FUNCTION *IN VIVO*

INTRODUCTION

Mitochondrial dynamics are increasingly prevalent in the mitochondrial literature. However, whilst they have been investigated extensively both *in vivo* (Bilsland et al. 2010; Sajic et al. 2013; Sorbara et al. 2014) and *in vitro* (Kiryu-Seo et al. 2010; Zhang et al. 2010; Obashi & Okabe 2013), the properties of the image acquisition and the modes of analysis vary significantly across studies. Recently, efforts have been made to compare and rank different tracking approaches (Chenouard et al. 2014; Bros et al. 2015), but to this day no generally agreed on solution has emerged. Similarly, TMRM is a common tool in mitochondrial research, but even *in vitro* its use has largely been restricted to hole cell analyses and examples of TMRM measurements at mitochondrial resolution are rare (Breckwoldt et al. 2014).

Early during the course of this work I thus set out to develop an analysis pipeline which allowed me to quantify reliably both mitochondrial transport and function in vivo. The requirements for this were:

a) **Single organelle resolution**: Estimates of shape, movement, and membrane potential should be extracted for each individual mitochondrion.
b) **Verification**: Tracking of mitochondria should be correspond well with manual analysis, and TMRM analysis should be able to detect drug-induced increases and decreases in mitochondrial membrane potential.
c) **Minimal manual interaction**: Manual steps should be reduced to conducting the actual experiment and outlining the axons of interest guaranteeing reproducibility and reducing bias

As I was unable to find a solution that worked "out of the box", I devised a combination of pre-existing and novel methods.

This chapter describes my final approach analysing mitochondrial dynamics and function *in vivo*, and experiments to verify the methods, as well as insights about mitochondrial transport and function in the saphenous nerve of untreated animals.

AXONAL MITOCHONDRIAL TRANSPORT AND FUNCTION – PREVIOUS FINDINGS AND OPEN QUESTIONS

It is widely accepted that mitochondrial transport and fission / fusion are essential for a neuron's long term survival: mutations in kinesin and dynein have been shown to cause axonal swellings followed by degeneration (Pilling et al. 2006), loss of the mitochondria fusion proteins Mfn1 and Mfn2 is incompatible with embryonal development (Chen et al. 2003; Lee et al. 2012), and disruption of mitochondrial transport is implicated in a growing number of neurological diseases (see Burté et al. 2014 for a review). This has led to the theory that axonal mitochondria need to be regularly supplied with new, undamaged proteins and mtDNA through fusion with younger mitochondria travelling down from the nucleus, whilst old material needs to be transported back to the nucleus to be destroyed through mitophagy. However, details of this machinery are not well understood. It is, for example, not fully known which factors decide whether and how two mitochondria will fuse. There generally appear to be two different versions of fusion: full fusion and a much faster exchange of material named "kiss and run fusion" (Liu et al. 2009; Wang et al. 2012). Full fusion, which is the complete merging of two particles into one, is enabled by the fusion protein optic atrophy-1 (OPA1) which is ingested and degraded at low membrane potentials (Legros et al. 2002; Song et al. 2007). Kiss-and-run is a much faster exchange (on the scale of a few seconds) which can happen between mitochondria associated with different microtubules, and from which both particles emerge with the same shape they had before the encounter. In contrast to full fusion it appears to be independent of OPA1 (Liu et al. 2009). Intriguingly, mitochondria in β cells have been shown to regularly break into fragments with uneven membrane potentials, depending on which they were either more likely to fuse again or to be degraded without further fusion (Twig et al. 2008). This leads to the intriguing theory

that mitochondria shed their damaged proteins through fission and the particle containing the larger number of damaged proteins is kept from fusing again because of its lower $\Delta\psi m$ and lack of OPA1. Computer simulations suggest that if such exchange happens at a sufficiently high rate, it provides a strong safety mechanism against the accumulation of damage (Mouli et al. 2009). What is not entirely sure is whether a similar mechanism can be found in neurons. A 2004 paper seems to corroborate this idea: Based on cultured chicken DRG neurons, Miller and Sheetz reported that highly polarised mitochondria in cultured neurons predominantly move toward the growth cone whilst mitochondria with low polarisation predominantly move back towards the nucleus (Miller & Sheetz 2004). However, they were not able to record fusion and fission behaviour due to technical limitations and, to my knowledge, their findings, although regularly cited, have yet to be replicated.

The exchange of proteins and mtDNA is not the only function of mitochondrial fission and fusion. Particularly, hyperfusion, that is the formation of large, connected mitochondrial networks can be seen in a number of physiological and pathological conditions. Hoitzing et al provide an interesting theoretical discussion of the potential benefits of mitochondrial fusion (Hoitzing et al. 2015), two of which are important in the context of this thesis. The first suggestion is that mitochondrial fusion may lead to increased ATP production efficiency. Experimental evidence for this comes from fasting or other forms of starvation in which mitochondria present decreased fission rates and fuse to fewer, larger organelles (e.g. Gomes et al. 2011; reviewed in Liesa & Shirihai 2013), or decreases in complex IV activity which was shown to be compensated for by hyperfusion (Rolland et al. 2013). The authors list multiple potential mechanisms, one of which involves a nonlinear increase in membrane potential such that the membrane potential of the fused mitochondrion is higher than the average membrane potential of the smaller, individual mitochondria. The second interesting potential of hyperfusion is that it may be useful in high-calcium situations as free calcium diffusion within the large

mitochondrion is a better way to ensure optimal calcium buffering than would be possible with multiple, smaller particles[7].

In addition to the open questions about the details of mitochondrial fission and fusion, it is not entirely clear whether, and to what extent, old mitochondria need to be transported back to the nucleus at all. While some evidence suggests that mitophagy is largely confined to the cell body (Cai et al. 2012), other groups report significant local mitophagy in axons (Ashrafi et al. 2014). Recently, Davis et al described a particularly interesting mechanism whereby retinal ganglion cells at the optic nerve head, and potentially also cerebral neurons in mice, shed mitochondria by forming axonal evulsions which are taken up by astrocytes and digested in astrocytic lysosomes (Davis et al. 2014). While it is not known how frequently this happens or whether there is an equivalent mechanism in the PNS, it raises the question of whether a cell necessarily has to go through the expensive process of transporting old mitochondria back to the soma and, if not, what the function of retrogradely moving mitochondria might be.

In the chapter at hand I attempt to shed a light on some of these questions. While the focus is largely on developing the necessary tools to quantify mitochondrial transport and membrane potential I also use these tools to try and answer a set of basic questions about mitochondria in naïve animals, such as: how much mitochondrial trafficking can be seen in the axons and in which direction? Are anterograde and retrograde transport balanced or not and are they correlated with the number of stationary mitochondria seen in the axon (as one might expect if the main purpose of motile mitochondria was to replenish the pool of stationary ones)? Can we observe fission and full fusion? What happens to moving mitochondria as they get close to stationary mitochondria? Do they slow down (which could be a sign of kiss-and-run exchange and / or potentially have implications for mitochondrial transport in more crowded environments, see introduction or last chapter's discussion)? Finally, is there any evidence that retrogradely moving mitochondria actually have a lower membrane potential than anterogradely moving ones?

[7] Hoitzing et al actually construct their argument around mitochondrial calcium signalling and argue that hyperfused organelles are better at avoiding saturation of calcium detecting enzymes. However, their line of reasoning applies fully to calcium buffering.

And is there any suggestion of increased effectiveness of larger mitochondria such as a higher membrane potential?

Before going into these questions, however, I will discuss the approaches to quantifying mitochondrial movement and membrane potential in more detail.

EXISTING SOLUTIONS FOR THE QUANTIFICATION OF MITOCHONDRIAL MOVEMENT

Perhaps the most common means of quantifying mitochondrial movement, particularly *in vitro*, are kymographs (e.g. Miller & Sheetz 2004; Kang et al. 2008; Bilsland et al. 2010; Zhang et al. 2010; Ohno et al. 2011; Zambonin et al. 2011; Zala et al. 2013; Obashi & Okabe 2013). In these representations, the axon is straightened and condensed to a single row of pixels for every frame. When aligning the condensed frames on top of each other, vertical and diagonal lines appear, representing stationary and motile mitochondria, respectively. Kymographs take advantage of the fact that in perfectly straightened axons mitochondria travel along a straight line and provide an easy to quantify, and visually striking, representation of movement. Arguably, they are the best way to detect and compare stopping and direction changes and a variety of methods exists to quantify them automatically (Chenouard et al. 2010; Mukherjee et al. 2011; Chetta & Shah 2011; Zhang et al. 2011). However, due to the compression of the whole axon width into a single pixel, the link between particle movement and the actual position of the particle is lost, meaning that it is difficult to combine information about, for example, movement and shape or movement and membrane potential of a given mitochondrion (Pereira & Maiato 2010 suggests the use of colour to encode a particles horizontal position but do not provide a way to retrive it from the kymograph). Furthermore, while kymographs produced from the thin axons and dendrites of cultured neurons tend to be fairly clean, the higher density of stationary mitochondria and much greater number of mitochondria moving close to each other, in peripheral nerves renders

them very cluttered and hard to read (see, e.g., the kymographs in (Bilsland et al. 2010) versus those in (Kiryu-Seo et al. 2010) as well as Figure 3.1).

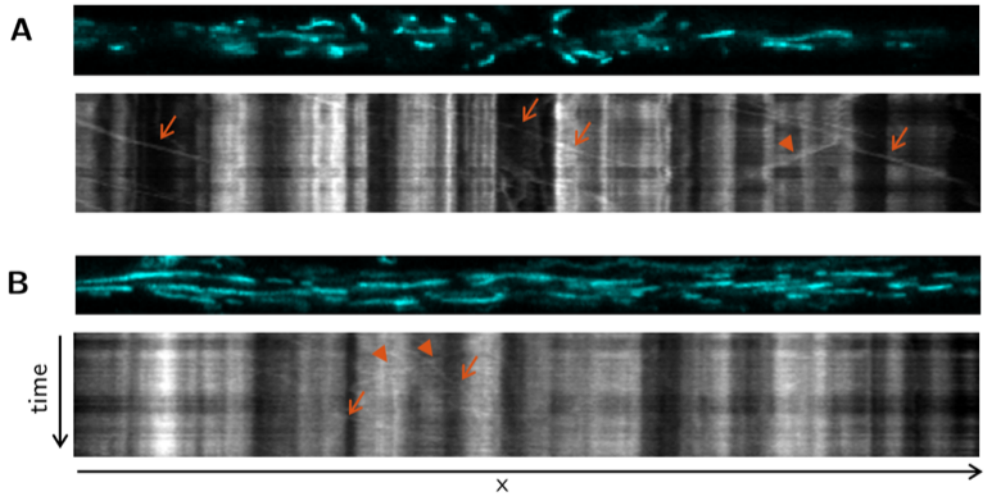

Figure 3.1: Kymographs. Genetically labelled mitochondria in cyan. **A**: Node of Ranvier of an untreated axon. **B**: Lysolecithin-treated axon on day 8. **Orange arrows** indicate anterogradely moving mitochondria, **arrow heads** show retrogradely moving mitochondria. Both kymographs are dominated by static mitochondria. Automatic tracking of the two time lapse recordings revealed 38 and 20 particle tracks, respectively.

Other studies rely on manual tracking for the quantification of mitochondrial movement (Sorbara et al. 2014; Bros et al. 2015). While precise, this method is immensely labour intensive and does not allow for blinded analysis if differences between treatment groups (such as the absence of the myelin sheath, see Figure 2.6) are obvious in the time lapse videos.

Finally, over the last years multiple fully automated particle tracking solutions – both commercial and free – have been published (see Chenouard et al. 2014 for an overview and comparison). Fully automated solutions promise speed, convenience, and high reproducibility. However, few software packages have been optimised to capture axonal transport and a recent comparison showed poor correlation between manual and automated quantification of mitochondrial movement (Bros et al. 2015). One noteworthy particle tracking solution developed specifically for the quantification of mitochondrial movement is the Difference Tracker plugin (DT) (Andrews et al. 2010). Freely available

and the highest scoring algorithm in the abovementioned comparison study, DT has been used both in our lab (Sajic et al. 2013) and by others (Milde et al. 2015). The principle behind DT is to extract only the moving particles from a time lapse recording, thereby reducing the number of possible connections in particle tracking. In a second step, these particles are then assigned to tracks using a simple nearest neighbour search with motion propagation according to the last observed speed of a particle. Unfortunately, in my hands, tracking results obtained with DT did not show a satisfying correlation with manually obtained results (see results). Furthermore, since DT's segmentation step is performed on a per-pixel basis, the resulting moving particles are only fragments of the underlying mitochondrion, preventing any further analysis of mitochondrial shape and size.

Given these limitations I decided to adapt an existing, fully automated particle tracking framework for the quantification of mitochondrial movement whilst also building on the idea of separating motile particles from stationary ones. In doing so I aimed to get a full set of data (size, shape, position, movement, membrane potential) for every mitochondrion in a single run with minimal manual interaction.

AUTOMATED SEPARATION OF STATIONARY AND MOTILE MITOCHONDRIA

Linking particles across frames is an optimisation problem, the complexity of which grows exponentially with the number of candidate particles (Jaqaman & Danuser 2009). Arguably, the strength of the DT algorithm lies in its ability to reduce the number of candidate particles by removing those which are not moving. This is achieved by comparing intensities of each pixel between two frames and including only those pixels in the linking step which decrease in brightness by more than a given threshold value (Andrews et al. 2010 section 3.1). Here, I extended this principle in several ways: Firstly, instead of classifying pixels as either stationary or moving, a measure of stability (*stat score*) is calculated. The stat score is the number of subsequent frames in the segmented

video in which a specific pixel (e.g. at position (13, 35)) is classified as belonging to a particle (see Figure 3.2 B). Neighbouring pixels belonging to the same mitochondrion can be expected to change at a similar rate and thus have similar stat scores. Therefore, particles can be reconstructed from stat scores by setting a maximum stat score difference Δss. Using a simple flood fill, neighbouring pixels with a difference in stat score $<\Delta$ss can be identified as belonging to the same particle. This yields a set of putative particles (sets of neighbouring pixels) with a known size and a fairly uniform stat score. In a final step, each particle is classified as either stationary or moving by combining information about their size and median stat score with a predefined minimum speed. If, for example, the threshold for considering a particle as stationary is set to 0.5px per frame (or 1px every two frames) and the length of a given particle is 5px, then this particle is classified as stationary if it has a median stat score $>$10.

Using this simple algorithm, it is possible to separate reliably moving particles from stationary ones even before tracking, which significantly reduces the complexity of particle linking. Furthermore, the algorithm improves video segmentation by breaking up clusters of moving and stationary particles which are close together and thus have not been successfully separated in the segmentation step. This is important since optical fusion of nearby particles is both a weakness of segmentation algorithms without a shape prior (such as Squassh) and a common problem in particle tracking (Jaqaman & Danuser 2009).

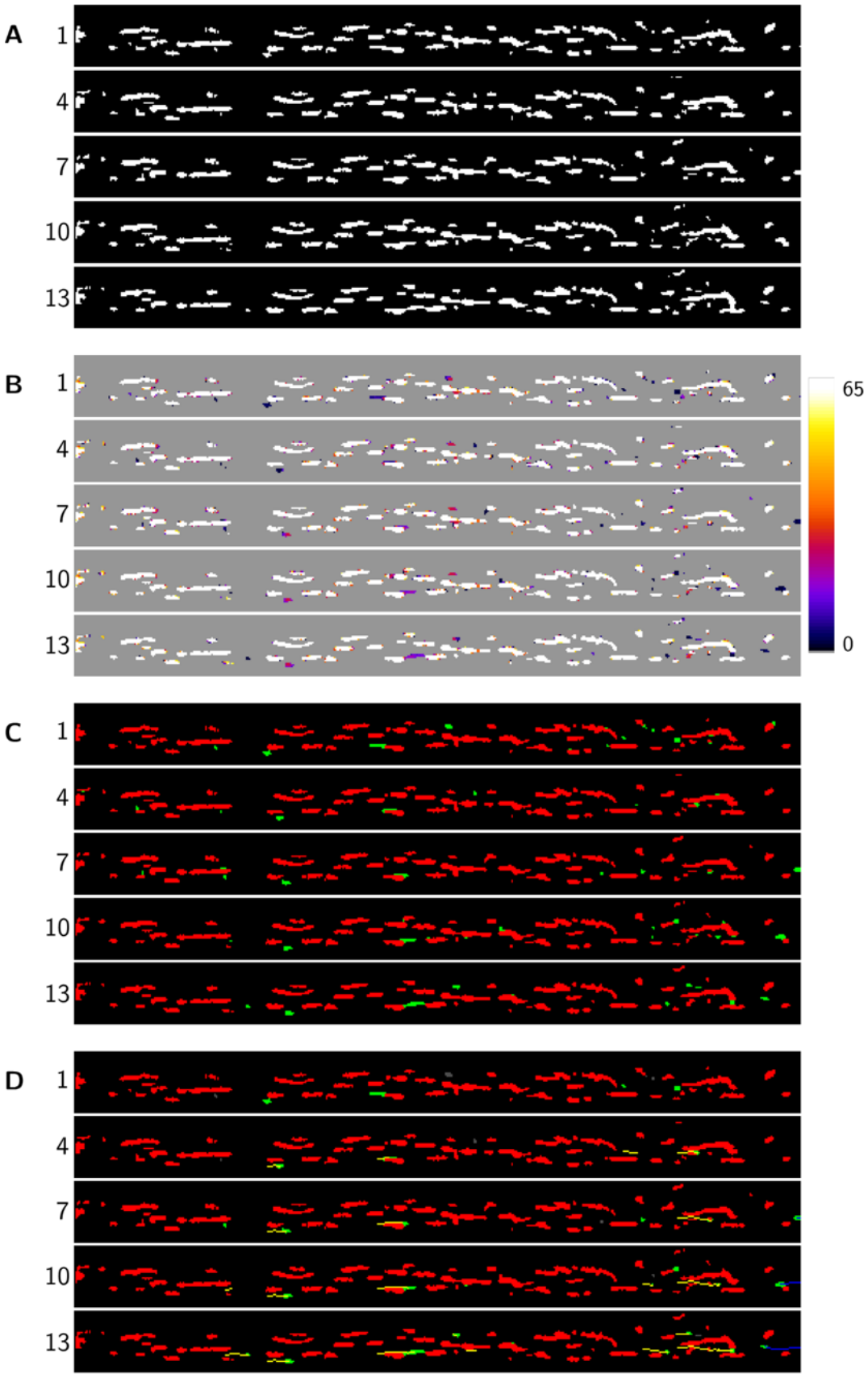

Figure 3.2: Demonstration of the particle classification algorithm. Numbers denote frame numbers. **A**: 5 frames of Squassh-segmented particles spanning 13 frames

/ seconds. **B**: Corresponding pixel stat scores. For demonstration purposes, background is shown in grey. Note that individual particles have homogeneous stat scores, thus making it possible to break up clusters of particles. **C**: Particle separation before tracking. By comparing a particle's median stat score to its length, it is possible to classify the particle as stationary (red) or potentially moving (green). Only potentially moving particles are used in particle tracking. **D**: After particle tracking. Multiple moving mitochondria were successfully tracked including some which initially appeared fused to static particles and were hard to spot even by eye. Putatively moving particles (green in C) which could not be assigned to a track are allocated to a neighbouring static particle where possible or otherwise ignored in the subsequent analysis (shown in grey).

PARTICLE TRACKING: SPECIAL CONSIDERATIONS FOR MITOCHONDRIAL MOVEMENT

Once particles have been extracted from raw data through segmentation, they can be linked over time to form trajectories and extract movement statistics. This is a non-trivial task because in most cases a given particle could be assigned to multiple different tracks. An optimal strategy to construct tracks from a given set of particles is Multiple Hypothesis Tracking (MHT) (Reid 1979; Blackman 2004). In MHT, given a set of tracks and a set of new particles, likelihoods are assigned to every possible link between a particle and a track, as well as the case of a particle starting a new, independent track. In cases where multiple alternative solutions exist, all possible solutions are simply carried forward. The expected trajectories of particles are calculated for every scenario and combined with the next set of particles from the next frame, yielding an extended set of connections and their likelihoods. After all available information has been incorporated, an optimal ensemble of non-conflicting track assignments can be selected according to the highest global likelihood. This combination of assignments is the best possible solution to the particle linking problem given the data (Blackman 2004; Jaqaman & Danuser 2009). Unfortunately, MHT is often not feasible in practise because the enormous number of possible solutions even for relatively small particle linking problems (Jaqaman et al. 2008). Over the last few years, different ways have been developed to reduce the computational burden while retaining some of the benefits of MHT. One such solution was published in 2008 by Jaqaman and colleagues (Jaqaman et al. 2008). Similar to

MHT, their algorithm assigns a cost to all possible links between particles in two subsequent frames but instead of carrying forward all possible solutions, a locally optimal solution is calculated. This way, a set of track fragments is created which, in a second step, can be linked together globally to form the final tracks. This approach is not only computationally feasible but also adds the advantage of being able to deal with the temporary disappearance of particles due to movement artefacts, which is a common problem in in vivo applications. Since its publication, Jaqaman's algorithm has been used in various publications (Jaqaman et al. 2011; Chang et al. 2012; Reuter et al. 2014; Wu et al. 2014; Senning & Gordon 2015; Liu et al. 2015; Plebanek et al. 2015) and formed the backbone of the popular TrackMate plugin for ImageJ (http://fiji.sc/TrackMate). Furthermore, it has been made available in form of the Matlab particle tracking solution uTrack (http://lccb.hms.harvard.edu/software.html) which allows for easy extension using custom written cost functions. All particle tracking in this study is done using uTrack 2.1.3 with the custom written cost functions explained below.

Since mitochondria are transported through axons along microtubules they can only move in parallel with the axon's central axis. In straightened axons (as analysed here), mitochondrial movement should thus be largely horizontal. This fact can be exploited to reduce the number of false connections between particles. Furthermore, while mitochondria mostly move along a straight line with relatively constant speed, they can also stop and reverse direction (e.g. Sorbara et al. 2014). The cost function used in this study reflects these unique properties of mitochondrial transport in several ways. Firstly, it allows for two modes of motion propagation: forwards / backwards movement and stopping. During forward movement, only connections which deviate from the last direction of the particle by less than a given angle α_{vel} are allowed. The new position of the particle is estimated using a Kalman filter and the cost of linking depends on the squared distance between a candidate particle and this propagated position. Furthermore, penalties can be imposed for connecting particles of different sizes. Particles for which there is no movement history or which move so slowly as to be considered stopping can be linked to all particles within a small radius to account for drifts. Beyond this radius their links are limited to particles within α_{vel} from a horizontal line in either direction.

Lastly, a maximum vertical distance from the horizontal line can be defined regardless of the particle's previous movement. Figure 3.3 demonstrates all these restrictions.

Figure 3.3: Custom restrictions to particle linking. A custom set of cost functions for uTrack was developed in order to improve performance when tracking mitochondria. **A**: Particles without a known trajectory, or slowly moving particles, can connect to particles on both sides within a maximum displacement (dashed line, arrow) and a given angle α from the horizontal line. **B**: Particles which are moving with a known velocity can only connect to new particles close to their current position (stopping) or within α relative to their current velocity.

MEASURING MITOCHONDRIAL MEMBRANE POTENTIAL USING TMRM

As discussed previously, mitochondrial membrane potential (Δψm) is essential for mitochondrial function. Several indicators have been developed to assess Δψm, of which TMRM (tetramethylrhodamine methyl ester) and TMRE (tetramethylrhodamine ethyl ester) are the most common ones. A red-orange fluorescent, lipophilic, cationic dye, TMRM is rapidly taken up into axons and mitochondria due to their membrane potential. Thus, the final concentration of dye in mitochondria depends on both the axon membrane potential (Δψp) and the mitochondrial proton gradient (Δψm). In theory, the relative concentration of TMRM on the two sides of a membrane (e.g. inside the axon relative to the extracellular space) can be calculated using the Nernst equation:

$$\Delta\psi = 2.3\frac{RT}{mF}\log_{10}\left\{\frac{[TMRM]_{in}}{[TMRM]_{out}}\right\} \qquad (1)$$

where R is the gas constant, T is the absolute temperature, m is the electric charge on the ion, and F is the faraday constant. The factor of 2.3 is due to the use of log10 instead of ln. When filling in all constants and rearranging to express the concentration of TMRM inside a mitochondrion relative to the outside, this changes to:

$$[TMRM]_{in} = [TMRM]_{out} * 10^{\Delta\psi/61mV} \quad (2)$$

In equilibrium, this equation applies both to the axonal and to the mitochondrial membrane (Nicholls & Ferguson 2013 chapter 9). An important difference, however, is the time course of equilibration. Since mitochondria have an exceptionally large surface to volume ratio, TMRM exchange over their membrane is considered virtually instantaneous, whereas exchange over the axonal membrane is orders of magnitude slower (Gerencser et al. 2012; Nicholls & Ferguson 2013).

Since the mitochondrial concentration of TMRM is exponentially larger than the intra-axonal concentration, and the intra-axonal concentration in turn is exponentially larger than the extracellular concentration, it follows that even small differences in TMRM concentration in the extracellular space (e.g. between two experiments or due to dilution effects over time) lead to vast concentration differences in the mitochondrial matrices. This makes mitochondrial brightness by itself an unreliable indicator of $\Delta\psi m$. Sophisticated whole cell approaches based on mathematical modelling of dye dynamics have been developed, which allow for the absolute quantification of $\Delta\psi m$ with high precision (Nicholls 2006; Chinopoulos et al. 2010). However, approaches of this kind require extensive calibration and a precise loading of dyes which is not feasible *in vivo*. Given high enough resolution, a third approach is to measure the TMRM fluorescence within the mitochondrial fraction of an image relative to the surrounding cytosol (Chacon et al. 1994; Scaduto & Grotyohann 1999; Diaz et al. 2000; Nicholls & Ward 2000). As long as TMRM is used in non-quenching concentration (see below) the ratio of these intensities should depend mostly on $\Delta\psi m$ and be independent of the extracellular TMRM concentration. This approach was used throughout the present study.

At low concentrations, TMRM fluorescence intensity is generally assumed to be linearly correlated with TMRM concentration (O'Reilly et al. 2003; Gerencser et al. 2012; Nicholls & Ferguson 2013). Such concentrations are known as non-quenching (Nicholls & Ward 2000; Nicholls 2012). If, however, the dye concentration exceeds a certain threshold, the photon emissions of the densely packed TMRM particles within mitochondria begin to interfere and their cumulative fluorescence relative to their number decreases. In this setting, known as quench mode, the ratio of TMRM fluorescence between mitochondrial fraction and axoplasm does not correspond to the ratio of concentrations, making the estimation of mitochondrial membrane potential impossible. In practice, concentrations of TMRM used *in vivo* tend to be significantly higher than *in vitro* (e.g. 7.5nM *in vitro* (Gerencser et al. 2012) vs 600nM *in vivo* (Romanelli et al. 2013)). Hence, it is necessary to calibrate carefully the loading of TMRM in order to ensure non-quenching mode.

Here, I adapted an established *in vitro* protocol to estimate an appropriate TMRM concentration. The H^+ ionophore FCCP rapidly depolarizes mitochondria, thus provoking the release of TMRM into the axoplasm. In quench mode, this leads to a pronounced increase in whole cell fluorescence as previously quenched molecules (i.e. particles which did not add to the mitochondrial and cellular brightness) leave the mitochondrion and increase the overall fluorescence of the axon (Nicholls & Ward 2000; Brand & Nicholls 2011). No such increase can be seen in non-quench mode, since the mitochondrial depolarization simply causes a redistribution of unquenched TMRM particles. The quenching threshold can thus be established by applying FCCP to preparations with different concentrations of TMRM.

After establishing a candidate TMRM dose, I then verified its suitability for detecting changes in mitochondrial membrane potential via the application of $\Delta\psi m$ altering drugs. The antibiotic oligomycin binds to a subunit of the proton channel of the ATP synthase where it inhibits transport of H^+ protons from the outside of the mitochondrial inner membrane to the inside and thereby ATP synthesis (Symersky et al. 2012). Since mitochondria in intact cells usually produce ATP, this leads to a small increase in $\Delta\psi m$ (Nicholls & Ward 2000). FCCP, on the other hand, rapidly depolarises mitochondria, and when used at a sufficiently high dose completely abolishes $\Delta\psi m$. Treating cells with

oligomycin followed by FCCP is a well-established protocol to verify $\Delta\psi m$ measurements *in vitro* and the same approach was taken here *in vivo*.

MATERIALS AND METHODS

ANIMALS

Animals used in these experiments were either male C57Bl/6 mice acquired from Charles River (TMRM dose calibration) or male Mito-S mice bred in-house (all other *in vivo* imaging). Ages commonly ranged from 8 to 12 weeks, never exceeding 16, and care was taken to ensure that treatment and control groups were age-matched and wherever possible litter mates.

All animal experiments were carried out according to the 1986 Animals (Scientific Procedures) Act, UK, and were approved by the institutional ethics committee.

MICROSCOPES

Shortly after the conclusion of the pilot study, the LSM Pascal 5.0 microscope was replaced by an LSM 710 which yielded significant improvements in our imaging capabilities. Most significantly, much improved CFP contrast and reduced photo-bleaching allowed for simultaneous recording of CFP and TMRM. This chapter marks the transition from LSM 5 to LSM 710. Specifically, the experiment comparing different doses of TMRM is the last experiment performed on the old microscope. All subsequent experiments (including the validation of the chosen TMRM dose using oligomycin and FCCP) were conducted using new equipment.

TMRM DOSE CALIBRATION

First, a non-quenching dose of TMRM was determined based on changes in whole cell fluorescence. Animals (C57Bl/6J, n=5) were prepared for imaging as described in chapter 2. Additionally, a thin polypropylene tube was inserted through the skin and placed with its end close to the nerve (Figure 3.5). The tube was filled with a mixture of 0.5µM fluorescein and 100µM FCCP in sterile saline. Multiple fluorescein doses were tried and 0.5µM was selected because it allowed for clear monitoring of the FCCP injection but did not interfere with the TMRM signal. After the surgery, different doses of TMRM (1µM, 0.75µM, 0.5 µM, 0.25 µM; life technologies) diluted in sterile saline were applied to the desheathed nerve for 45min. A well made of petroleum jelly was formed around the surgical opening and the opening was covered with a glass coverslip.

Imaging was performed using the LSM Pascal 5.0 confocal microscope (Zeiss) and a Zeiss Appochromat 10x objective (NA 0.3). The gain of the photomultiplier tube was adjusted at the beginning of each experiment such that the average TMRM signal of the nerve was in the middle of the detectable intensity range. Settings for the green (fluorescein) channel were kept identical for all animals. A series of images was recoded with one image of both the red and the green channel taken every 10 seconds. After 2 minutes, 2-3µl of the FCCP containing solution was injected via the tube using a microinjection device. This corresponds to approximately 10% of the total liquid volume in the preparation, yielding a final FCCP concentration of 10µM. Time lapse recording continued for a total of 20min. If the fluorescein signal suggested that the FCCP did not spread throughout the field of view reaching all parts of the nerve, the recording was discarded. Furthermore, a control animal was treated with 1µM TMRM and a solution containing fluorescein but no FCCP was injected to control for potential bleed through of the dyes or any effects of the increase in pressure.

Images were processed using Fiji/ImageJ Version 1.48v. Time lapses were motion corrected based on their red (TMRM) channel using the 'Register Virtual Stack Slices'-Plugin. Subsequently, the nerve was selected manually and green and red fluorescence

averaged over the nerve were measured for every frame. TMRM intensity is presented normalized to the first 12 frames (i.e. before injection of the FCCP solution).

This series of experiments yielded a candidate dose of 0.25µM TMRM. To confirm the choice of this dose, animals (Mito-S, n=6) were prepared for imaging as described above. After exposing and desheathing of the saphenous nerve, a solution of 0.25µM TMRM in ACSF was applied for 45 min in order to allow the dye to equilibrate. Imaging was performed using the LSM 710 confocal microscope (Zeiss) and a Zeiss Appochromat Plan 63x oil objective (NA 1.4) using the same settings as in all subsequent mitochondrial imaging (see below). Throughout all experiments, the laser power, and photo multiplier gain for the CFP channel remained unchanged, while the laser power for the TMRM channel was slightly adjusted (within a range of 0.5% to 2%) in order to avoid over- or under-saturation. Axons of interest were located using the CFP channel only (and thus independent of their apparent TMRM intensity); then a single image of both CFP and TMRM was recorded.

After taking 10-12 such images, the animal was removed from the microscope stage, the coverslip taken off and a solution containing TMRM as well as either 10µg/ml (3 animals) or 25µg/ml (3 animals) oligomycin from a 1mg/ml stock in EtOH was applied to the nerve. The imaging procedure was repeated. Finally, a third solution containing the same dose of TMRM as well as 10µM FCCP was applied to the nerve, followed by a last round of imaging.

Relative mitochondrial TMRM intensity was measured relative to the surrounding axoplasm as described below (Image Analysis). Briefly, axons of interest were identified, cut out and straightened using Fiji (Schindelin et al. 2012). For every axon, the CFP channel was segmented using Squassh to create a binary mask. This mask was used to identify the location of mitochondria in the image. Using Matlab scripts, the TMRM intensity of every single mitochondrion was measured relative to its local background. The final intensity of a particle was defined as the median foreground intensity divided by the median background intensity.

Conditions were compared on an axon-by-axon basis with every data point corresponding to the median relative TMRM intensity of all mitochondria contained in that axon. Statistical significance was tested using the statistical software environment R. Using the *nlme* package, a two-level linear model with a fixed slope and random intercepts was fitted to the data. Median TMRM intensity per axon was used as the response variable, treatment ('tmrm only', 'tmrm + oligomycin', 'tmrm + FCCP') as a fixed effect and animal ID as a random effect. See Appendix A for a discussion of this approach.

IN VIVO IMAGING AND IMAGE ANALYSIS

Naïve animals (male Mito-S, 6-8 weeks, n=6) were anaesthetised with urethane and ketamine and prepared for imaging as described in chapter 2. TMRM was applied at a concentration of 0.25μM in aCSF for 45 minutes and the imaging site was sealed off with a cover slip as described above but without replacing the TMRM solution. Imaging was performed using a Zeiss Appochromat Plan 63x oil objective (NA 1.4). For each animal, time lapse recordings of at least 15 different axons were taken. The axons were selected based on genetically encoded CFP signal only to avoid bias towards particularly bright or dim TMRM intensities. If necessary, the laser intensity for TMRM imaging was adjusted slightly (within a range of 0.5% to 1.5%) to ensure that the signal fell in the middle of the detection range. Then, TMRM and CFP were recorded simultaneously at 1 frame/sec for 65 seconds. A pinhole size of 1AU was used to ensure a thin optical slice.

Analysis of mitochondrial movement was performed using the pre-processing method and custom cost functions for particle tracking explained above. Briefly, movement artefacts were reduced using the Descriptor-based Registration plugin (Preibisch et al. 2010). Axons of interest were identified, cut out and straightened using Fiji (Schindelin et al. 2012). For each axon, the CFP channel was segmented using the Squassh (*segmentation and quantification of subcellular shapes*) algorithm (Paul et al. 2013; Rizk et al. 2014) to create a binary mask. Squassh combines image segmentation with deconvolution based on the microscope's point spread function (PSF), which increases segmentation

performance near the resolution limit. PSF for both CFP and TMRM-based segmentation were determined experimentally from small, fluorescent beads (PS-Speck, Molecular Probes) using the same wavelength and pinhole settings as used during time lapse recordings (Cole et al. 2011).

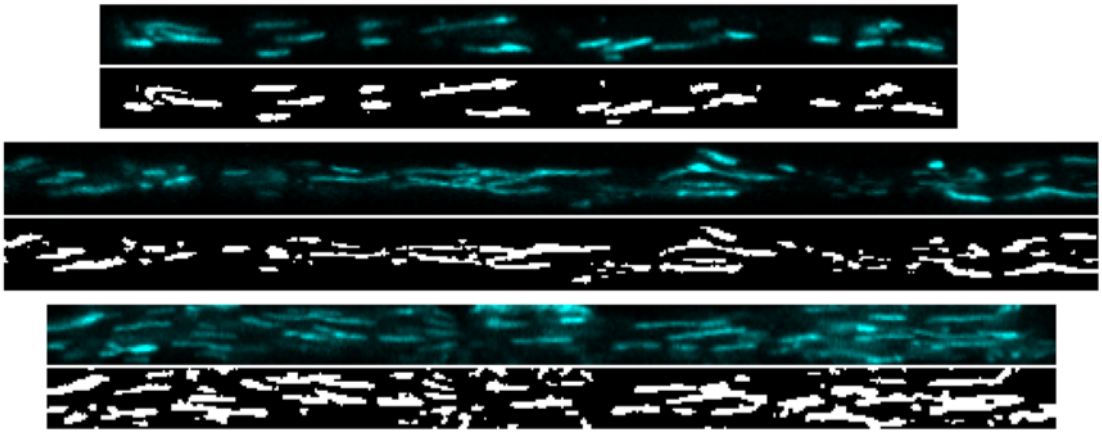

Figure 3.4: Squassh segmentation. Example frames from three different animals showing raw images of mitochondrial CFP fluorescence above the corresponding image segmentations.

Mitochondrial size and shape were measured in Matlab using these binary images. In order to extract statistics about mitochondrial dynamics, the segmented videos were further processed using a custom algorithm which utilizes pixel changes over time to classify particles as either moving or stationary and separate connected particles (see above). Particles categorised as moving we linked using the Matlab package uTrack 2.1.3 (Jaqaman et al. 2008) with custom cost functions (see above). Only tracks with a length of at least four frames and a total particle displacement of at least three pixels were used for further analysis.

TMRM intensity was measured separately for every mitochondrion relative to its local background as follows. First, the median intensity of all foreground pixels of the particle was measured. Then, a local background selection was created containing all pixels within a 3px radius around the mitochondrion of interest which were not part of, or immediately

adjacent to, another mitochondrion and the median intensity of these particles was calculated. The final intensity of a particle was defined as the median foreground intensity divided by the median background intensity.

EVALUATION OF PARTICLE TRACKING

In order to evaluate the performance of the segmentation and tracking solutions described above, the results of automatic particle tracking were compared with both manual tracking and the Difference Tracker plugin (Andrews et al. 2010). Briefly, videos of 115 axons from 6 animals and 3 different conditions (2x naïve: 37 axons, 2x day 8 saline control: 45 axons, 2x day 8 LPC demyelination: 33 axons) were used for comparison. The different conditions were chosen to test the algorithms on both normal axons and axons with increased mitochondrial content. Data for the LPC treated and control animals was taken from the time series study presented in chapter 4. All time lapses were registered using the *Register Virtual Stack Slices* plugin for Fiji (Arganda-Carreras et al. 2006), straightened, and cropped to 30 seconds duration. Subsequently, they were analysed in three different ways:

1. After enhancing contrast for maximal visibility, all particles in all time lapse recordings were tracked by hand using the manual tracking capability of the TrackMate plugin.
2. All videos were analysed using DT as described by Andrews et al. (2010) including the optional steps “Enhance contrast” (0.4%) and "Despeckle".
3. All time lapse recordings were analysed using the custom analysis pipeline described above.

For the purpose of this comparison, mitochondrial transport was defined as the average number of moving particles per frame times their speed.

STATISTICS

As before, the estimation of effect sizes and statistical significance testing was performed using a multi-level linear model with a fixed slope and random intercept via the *nlme* package for R. Where axon-specific effects were tested (e.g. when correlating the total area of stationary mitochondria with the total axonal transport), animal ID was used as a random effect. Correlations on the mitochondrial level (e.g. mitochondrial size vs speed or TMRM intensity of anterogradely vs retrogradely moving mitochondria) were estimated with both animal ID and axon ID as nested random factors. R2 was estimated as the marginal R2 (i.e. the proportion of variance explained by the fixed factors alone) using the method developed by Nakagawa and Schielzeth (Nakagawa & Schielzeth 2013) as implemented in the *piecewiseSEM* package in R (Lefcheck 2015). When analysing the speed of transport depending on the density of surrounding particles, mitochondria were compared with themselves and the effects of animals and axons could be neglected. Hence, a simple paired t-test was used to assess statistical significance.

RESULTS

TMRM DOSE CALIBRATION

The injection of FCCP / control solution could be precisely monitored via the fluorescein signal (Figure 3.5). In all animals used for the final analysis, this signal increased rapidly for 2-3 frames (20-30 seconds) before falling off exponentially to slightly over starting level. Injection of fluorescein alone did not increase the TMRM signal but caused a gradual decrease of approximately 10% over 15 minutes (Figure 3.5 B). In contrast, when FCCP was injected, whole-nerve TMRM fluorescence showed a rapid, dose dependent increase for concentrations >= 0.5µM and a steeper-than-control decrease for a TMRM concentration of 0.25µM (Figure 3.5 B). After the spike, TMRM fluorescence of all concentrations decreased at a similar rate. These results suggest that in this particular setup TMRM concentration of 0.5µM and more caused imaging in quench mode while concentrations <= 0.25µM should be used for non-quench imaging. While this is a rather

high concentration compared with typical *in vitro* studies, it is nevertheless lower than many concentrations used *in vivo* (Nikić et al. 2011; Romanelli et al. 2013; Sajic et al. 2013).

Based on this finding, all subsequent experiments were conducted using a TMRM concentration of 0.25μM.

Next, I measured relative TMRM intensity under regular experimental conditions. Results varied considerably between axons, with the median TMRM intensity over background of all mitochondria in an axon ranging 1.22 to 5.56 in untreated axons. On average and after correcting for animal baseline, the intensity was 2.91 in untreated axons (SE: 0.10). Upon the application of oligomycin, TMRM intensity increased by 0.65 (SE: 0.11, $p<0.001$). This difference, whilst highly significant, was subtle and impossible to see by eye. FCCP treatment, on the other hand, led to a very obvious redistribution of TMRM from the mitochondria to the axoplasm and relative mitochondrial intensity fell by 1.49 relative to untreated axons (SE: 0.11, $p<0.001$). This pattern could be observed across all five animals, suggesting that a TMRM concentration of 0.25μM is a safe choice for detecting both increases and decreases in $\Delta\psi m$.

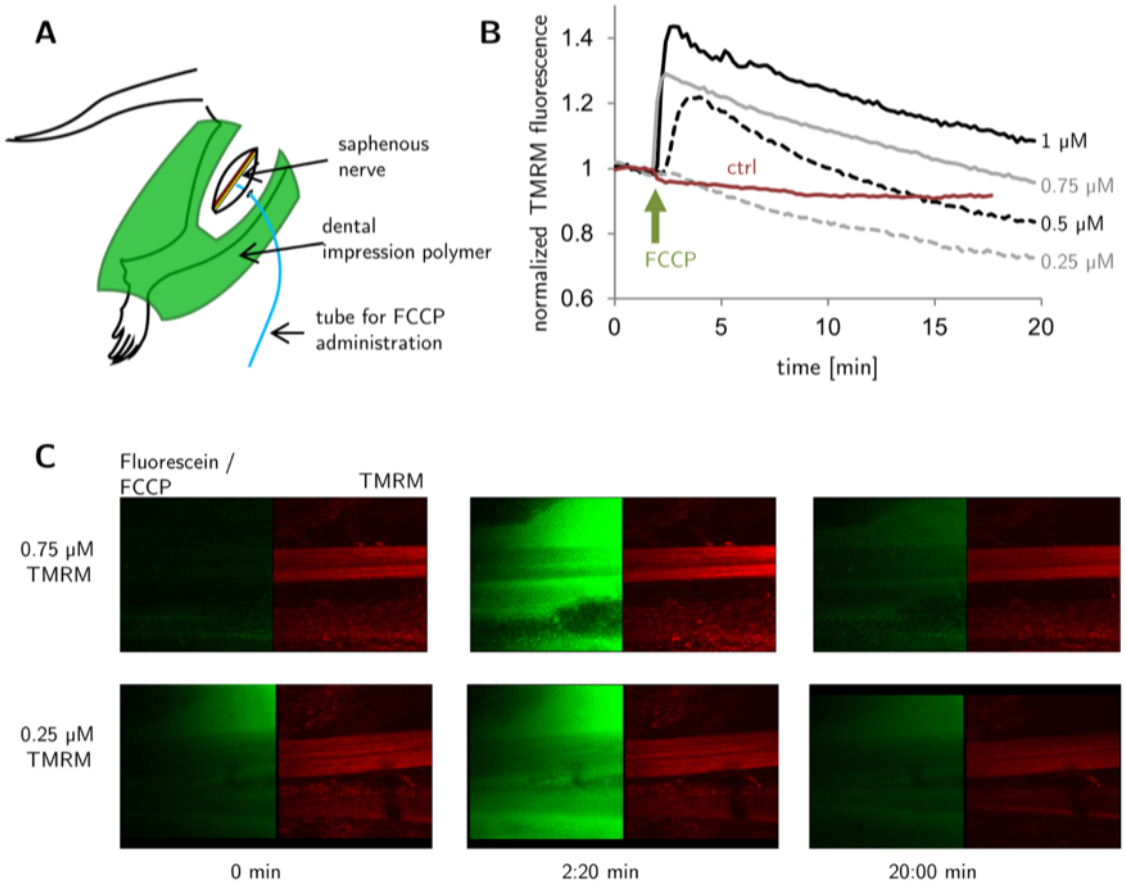

Figure 3.5: **TMRM dose calibration *in vivo*.** **A**: Setup: 10µM FCCP together with 0.5µM fluorescein (for visualization of the injection) is administered through a thin tube in the skin. **B**: Whole nerve TMRM fluorescence normalised to baseline. Upon application of FCCP, a rapid spike in TMRM intensity is visible for 1µM, 0.75µM, and 0.5µM TMRM which slowly resolves over time. No such spike is seen when using 0.25µM TMRM. The red line indicates a control experiment with 1µM TMRM (the maximum dose used) and an injection of fluorescein, but no FCCP, demonstrating that there is no significant bleed through between the red and green channel. **C**: Motion corrected time lapse images at the beginning of the experiment, just after injection of FCCP and fluorescein, and after 20 minutes.

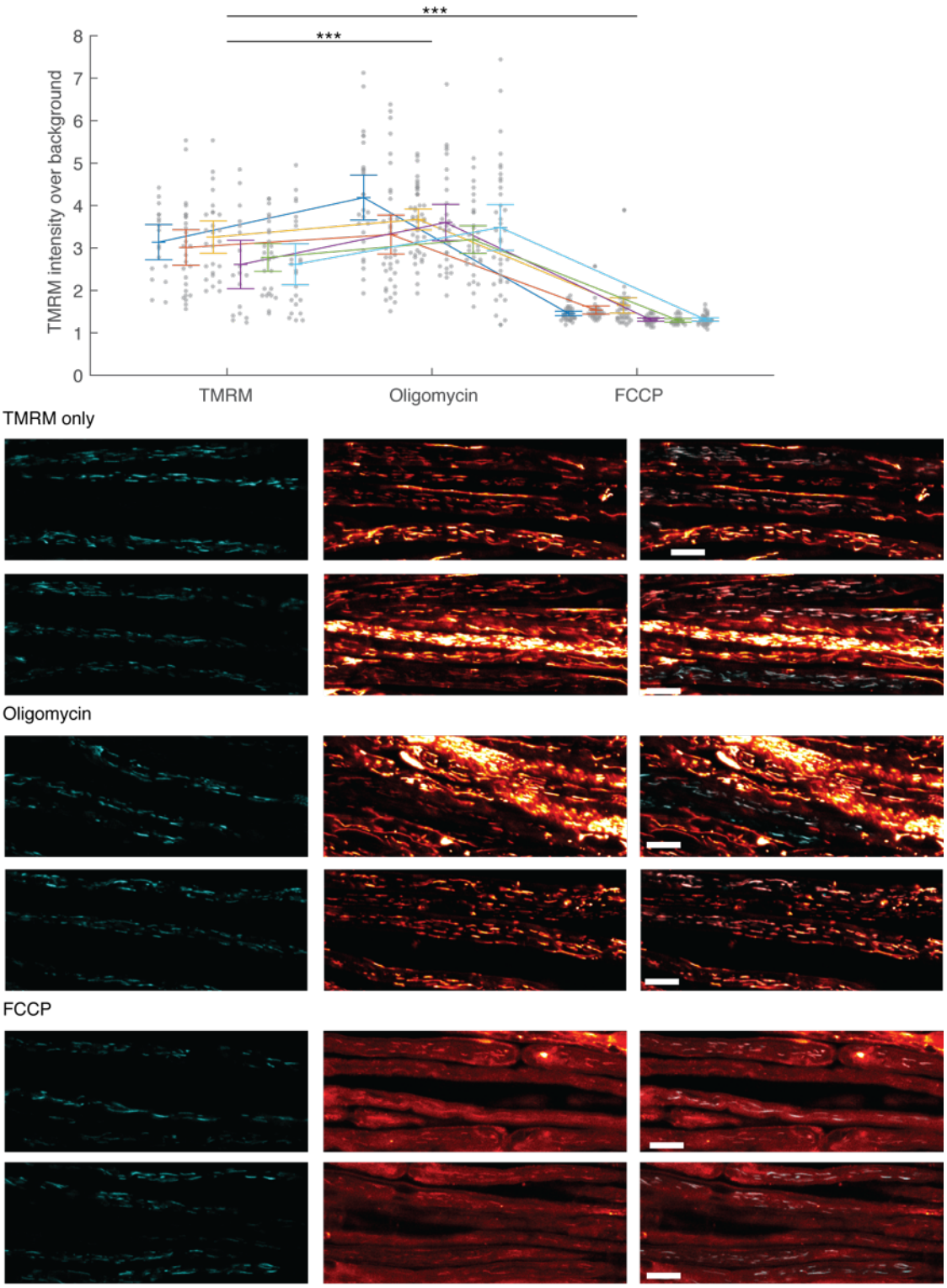

Figure 3.6: **Drug induced changes in TMRM signal**. **Top**: TMRM intensity over background. Each dot indicates the median TMRM intensity of a single axon, each coloured line indicates mean intensity ± 95% confidence interval of the mean per animal. Bottom: Representative example images (2 per condition). **Left**: CFP channel, middle: TMRM channel, right: merge. A red to white lookup table was applied to the TMRM channel in order to amplify differences in signal. Bars indicate 10µm. See text for details.

EVALUATION OF PARTICLE TRACKING

Both Difference Tracker measurements and the analysis method developed here correlated significantly with the results obtained through manual tracking. However, DT results were noisy, accounting for only 61.4% and 40.2% of the manually observed transport for anterograde and retrograde particles, respectively (as indicated by the adjusted R^2 of a linear fit). In contrast, the analysis routine developed here had a signal to noise ratio of roughly 80% for both directions (anterograde: 79.1%, retrograde: 82.4%). The performance of both algorithms was worst in case of the LPC-treated axons, with the R^2 of DT dropping to 0.26 and -0.02 for anterograde and retrograde transport, respectively while the custom solution showed R^2s of 0.48 and 0.72. It also more accurately captured the speed distribution of moving mitochondria, and was able to reconstruct a higher percentage of tracks (DT: 58% (95% CI: 43%-73%); custom: 71.3% (95% CI: 57%-86%)). Both approaches tended to underestimate mitochondrial transport compared with manual analysis. See Figure 3.7 for details.

The difference between manual tracking and automated tracking was largely due to problems with segmentation. Many particles detected in manual tracking were so faint as to be unidentifiable in a still image.

The differences between the performance of DT and the custom solution developed here could mostly be explained by one of two sources of error. Firstly, the pixel by pixel filtering step used in DT produced a number of artefacts at the edges of large, stationary particles which were subsequently linked to form false tracks. This was prevented in the custom particle splitting solution by grouping pixels into larger clusters. Secondly, a number of tracks produced by DT showed unrealistic, zig-zag-shaped changes in direction, linking particles which did clearly not correspond to the same mitochondrion. Such links were prevented in the custom made linking algorithm by preventing the connection angle between two pixels (see Figure 3.3).

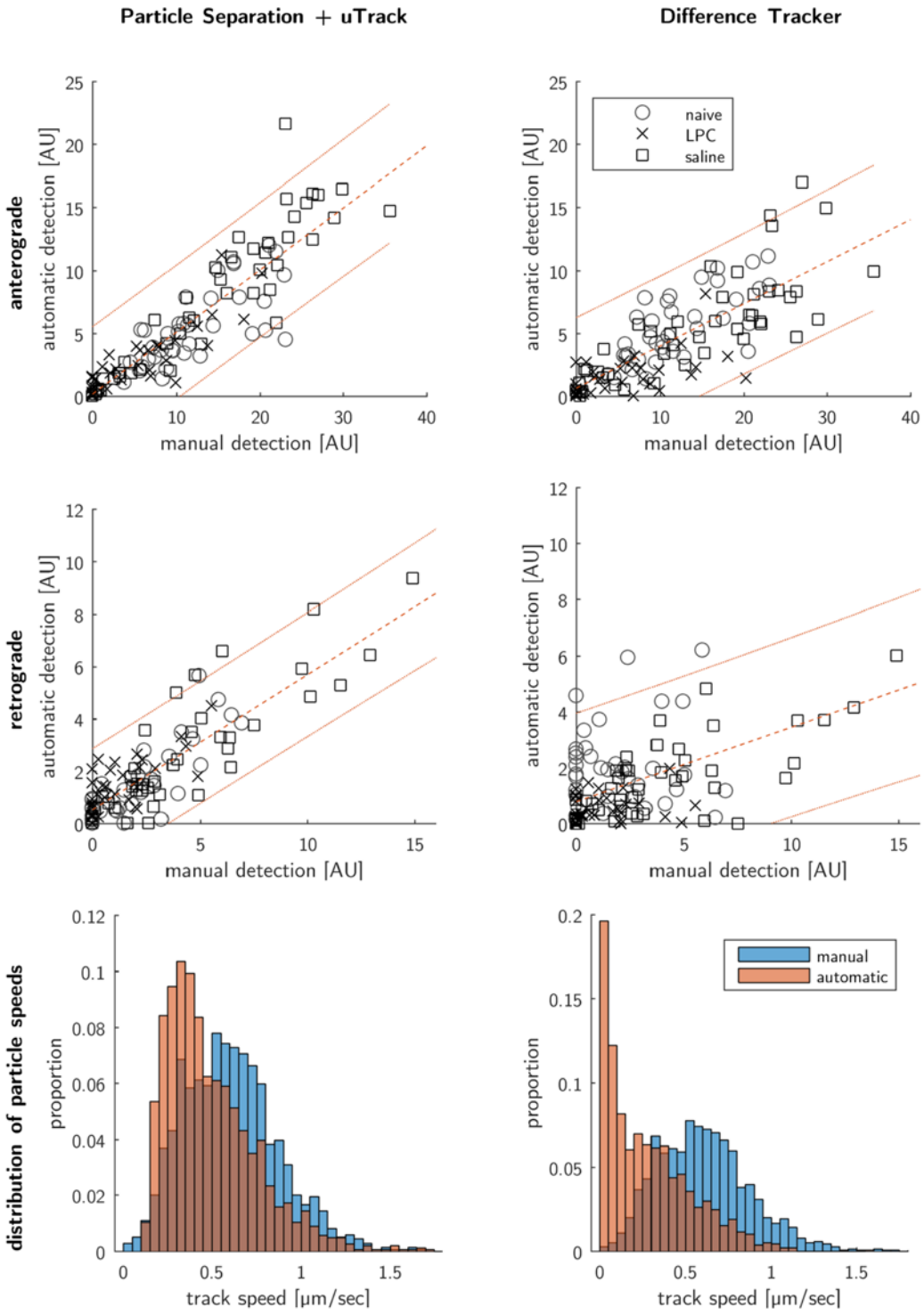

Figure 3.7: Correlations between manual and automatic tracking solutions. The left column shows results obtained with a custom-made particle tracking solution, the right column shows results obtained with the Difference Tracker plugin. Orange lines indicate the linear correlation between manually and automatically acquired results as well as the expected 95% confidence interval for new measurements. See text for details.

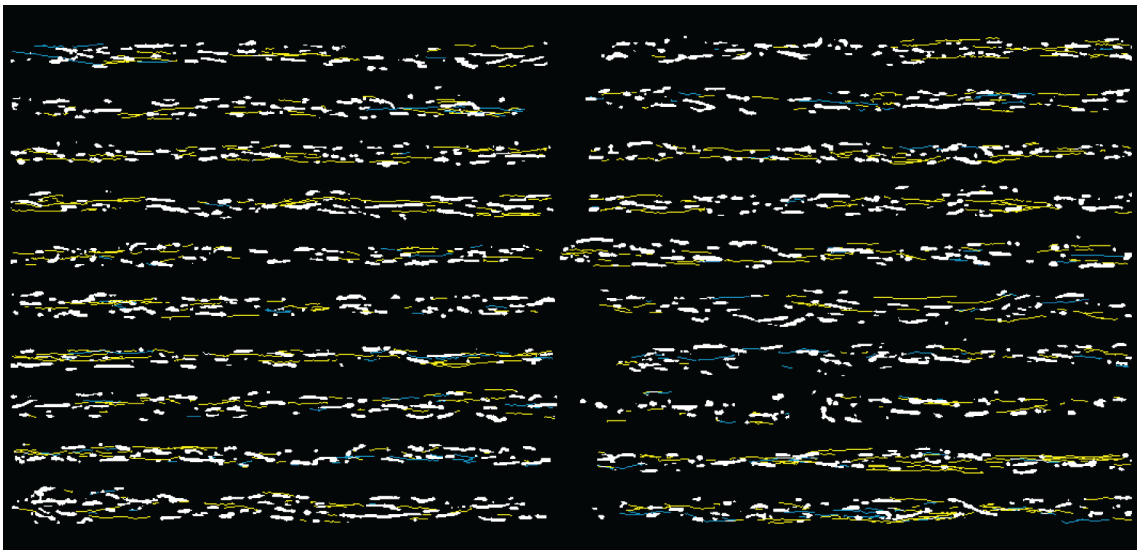

Figure 3.8: **Mitochondrial trafficking in naïve animals**. The image shows 20 randomly selected axons with 61 seconds recording time each. Stationary mitochondria (median projection) are shown in white, the tracks of anterogradely (left to right) moving mitochondria are shown in yellow and retrograde tracks are shown in blue. In order to clear up the image, the outlines of the moving mitochondria themselves are not shown.

A total of 110 axons from 6 different naïve animals were recorded, yielding 2432 individual mitochondrial tracks. Mitochondrial transport could be detected in all axons, although the rate of transport varied significantly between axons. While movement of mitochondria was observed to stop and start, very few changes of direction were seen. More remarkably, not a single fusion or fission event was observed.

Compared with the pilot study, transport rates measured here were lower in both directions (pilot: anterograde transport 1.84 ± 0.12 AU, retrograde transport 0.52 ± 0.08 AU; here: anterograde transport 1.19 ± 0.07 AU, retrograde transport 0.30 ± 0.03 AU; mean ± SE). However, the difference between anterograde and retrograde transport was remarkably consistent with anterograde transport on average accounting for 78% of all mitochondrial movement vs 79% in the pilot study (see also Figure 3.9 D). A more detailed analysis revealed that this difference between directions was almost entirely

explained by the number of moving particles; both speed of movement ($p = 0.054$) and size of moving particles ($p = 0.051$) did not differ between the directions.

I first tried to understand the relationship between axon width, total area of stationary axons, and mitochondrial transport. Axon diameters (defined as the width of the smallest rectangle around the straightened axon that could contain 98% of all mitochondrial pixels) ranged from 2.11µm to 5.80µm. There was some correlation between axon diameter and mitochondrial content of the axon (see Figure 3.9 A), however, the diameter only explained about 20% of the variation in total mitochondrial area (marginal R2=0.19, $p < 0.001$). Since mitochondrial dynamics are often thought to maintain and 'refresh' populations of stationary mitochondria, I next investigated the correlation between each axons stationary mitochondrial mass and the total mitochondrial transport observed (Figure 3.9 B). Somewhat surprisingly, neither anterograde nor retrograde transport of mitochondria were correlated with the total area of stationary mitochondria ($p = 0.95$ and $p = 0.20$) or mitochondrial density of the axon ($p=0.16$ and $p=0.72$). Even the correlation between anterograde and retrograde transport, whilst statistically significant ($p < 0.05$) was extremely weak ($R2 = 0.05$, Figure 3.9 C).

As mentioned in the introduction, one open question is whether mitochondrial transport can be inhibited by spatial constrains and the resulting obstruction. The high precision particle tracking achieved here enabled an interesting way to tackle this question. Whilst there was generally a lot of free space within untreated axons (the maximum intra-axonal area occupied by stationary mitochondria in this data set was 21%), many moving mitochondria came close to stationary particles at some point during the observation period. In order to find out whether this lead them to slow down, I compared the speed of every mitochondrion when it was moving freely and away from other particles to when it was close to a stationary particle. *Close* was defined as having no blank pixels between the moving and a stationary mitochondrion (i.e. them passing at a distance of < 0.18µm) in at least two consecutive frames (see Figure 3.2 for an example). The analysis was performed using 525 individual tracks. No difference was found between parts of the track where moving mitochondria were close to other particles and parts where they were moving freely ($p = 0.17$, Figure 3.9 E). The average change was estimated to be between

-0.006μm/sec and +0.03μm/sec (95% CI) compared with an average speed of about 0.45μm/sec. Thus, there was no evidence for a slowing down of moving mitochondria due to the proximity of other particles.

Finally, I investigated whether larger mitochondria were moving at a slower speed. The analysis revealed the average speed of moving mitochondria to be extremely uniform with 95% of all mean track speeds between 0.15μm/sec and 0.89μm/sec (2432 tracks) and while very large particles were found to move slightly slower, the correlation between size and speed was extremely weak ($R2 = 0.027$, $p < 0.001$).

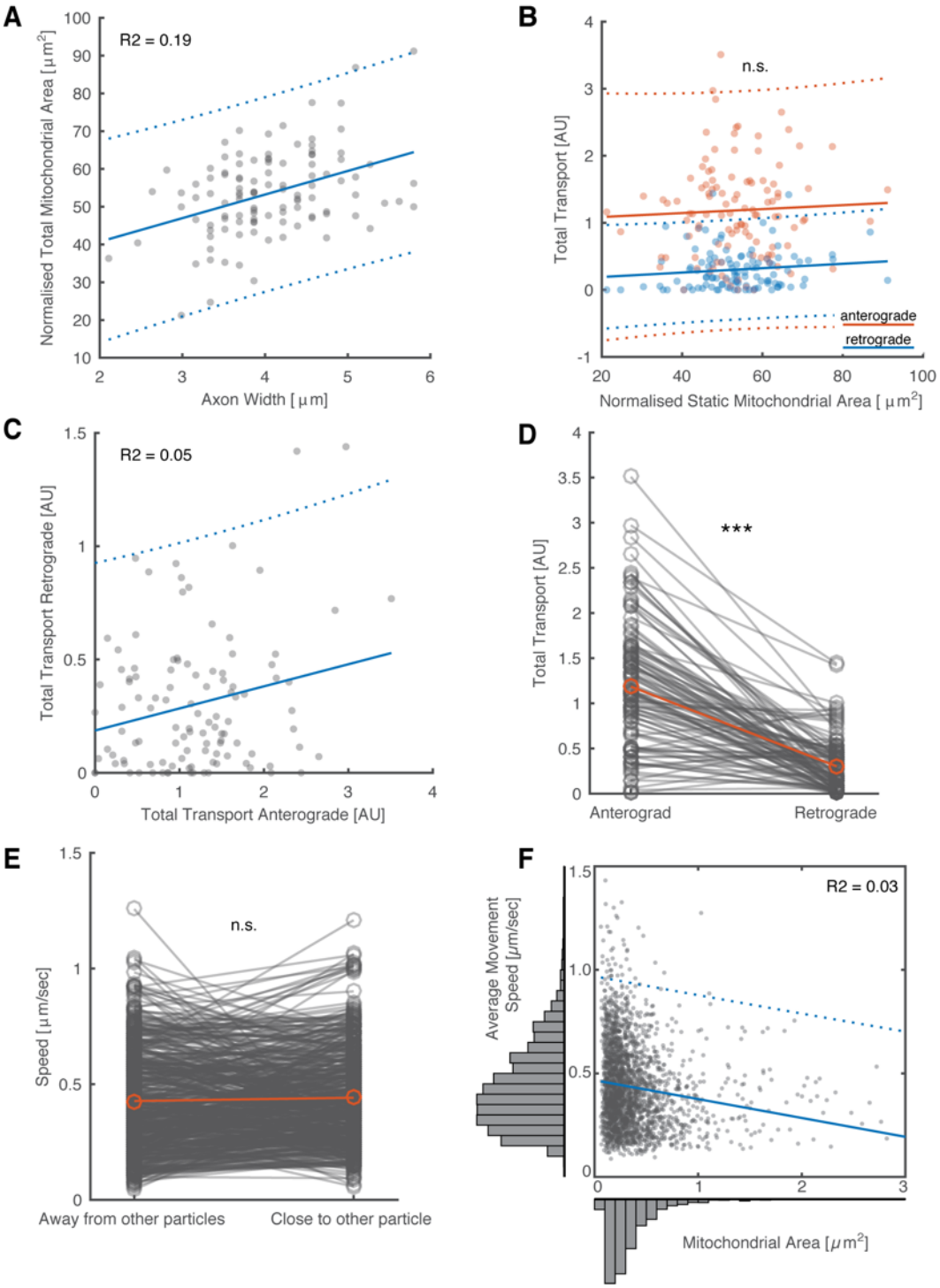

Figure 3.9: **Mitochondrial dynamics in naïve axons**. **A** Axon width explains some, but not all of the total mitochondrial content of the axon. **B** Neither anterograde, nor retrograde transport in an axon show a significant correlation to the size of its stationary population of mitochondria. **C**, **D** Retrograde transport was significantly lower than anterograde transport and both were only weakly correlated. **E** There was no sign of slowdown as motile particles passed stationary ones at low distances. **F** The speed of a moving mitochondrion showed virtually no correlation with its size.

In addition to mitochondrial trafficking, I also investigated the membrane potential of different mitochondrial populations in untreated axons. There was a small but significant difference between the relative TMRM intensity of stationary and moving mitochondria with stationary mitochondria showing higher intensity ($p < 0.05$, 108 axons, Figure 3.10 B). However, the interpretation of this difference was complicated by a weak yet significant correlation between mitochondrial size and TMRM intensity ($R2 = 0.05$, $p<0.001$, Figure 3.10 C). In order to untangle the two factors, I constructed a multilevel linear model with TMRM intensity as the outcome variable, mitochondrial size and motility (moving vs stationary), as well as their interaction as fixed factors, and animal ID as well as axon ID as nested random factors. The data consisted of 5108 mitochondria (646 moving, 4462 stationary) from 110 axons. After correcting for animal and axon specific differences in this way, both size and motility were found to influence independently a mitochondrion's membrane potential. The baseline intensity over all mitochondria was found to be 2.74 ± 0.12 (SE, $p < 0.001$). Every extra μm^2 of mitochondrial size increased this value by 0.33 ± 0.02 units ($p < 0.001$). In addition, being mobile reduced TMRM intensity by 0.37 ± 0.09 units on average ($p < 0.001$). The interaction effect of area and motility was not significant ($p = 0.85$). However, whilst size and motility seemed to be contributing factors to a mitochondrion's membrane potential, they only explained a small fraction of the total variance in TMRM intensity (marginal $R2 = 0.06$).

As mentioned in the introduction, a long standing discussion is whether mitochondria which are transported retrogradely are older and destined for mitophagy. One piece of evidence for this theory which has been suggested is that retrogradely moving mitochondria have a lower membrane potential than anterogradely moving ones (Miller & Sheetz 2004). I tested this idea by comparing the relative TMRM intensity of anterogradely and retrogradely moving mitochondria whilst correcting for the influence of axon and animal. A total of 1702 anterogradely moving mitochondria, and 456 retrogradely moving mitochondria were measured. I did indeed find a small, yet significant difference between the two populations with retrogradely traveling

mitochondria showing a 5% lower relative TMRM intensity compared with anterogradely moving ones (ant: 2.44 ± 0.07 SE ret: 2.32 ± 0.08 SE, $p < 0.01$, Figure 3.10 A). Importantly, this difference was not explained by size as retrogradely moving particles were actually slightly larger than anterogradely moving ones (ant: 0.35µm^2 ± 0.04 SE ret: 0.40µm^2 ± 0.04 SE, $p < 0.01$, data not shown).

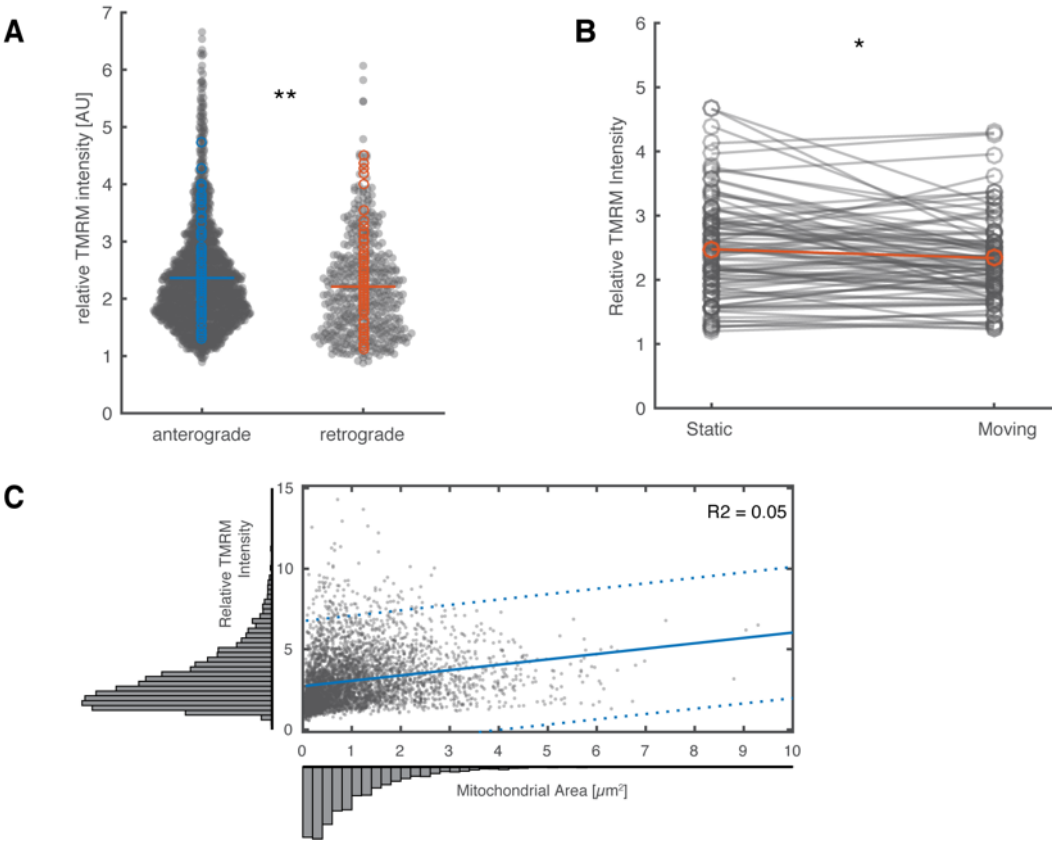

Figure 3.10: **TMRM intensity in untreated axons**. **A** Small but significant difference in the relative TMRM intensity between anterogradely and retrogradely moving mitochondria. Grey dots denote individual mitochondria and circles show axon means. **B**, **C** Stationary mitochondria showed slightly higher membrane potentials than moving mitochondria which was partially, though not exclusively, explained by size (see text for details).

The investigation of mitochondrial function and trafficking in untreated animals yielded a couple of encouraging result. Firstly, methods to quantify mitochondrial trafficking and membrane potential were developed and verified. I was successfully able to detect the relatively small difference in membrane potential caused by the application of oligomycin (about 5mV according to Nicholls & Ward 2000) which would likely go undetected with a quenching concentration of TMRM. However, it is also apparent that this approach does not allow for an absolute quantification of $\Delta\psi m$. Assuming $\Delta\psi m = 150mV$, the Nernst equation suggests a $[TMRM]_{mito}$ to $[TMRM]_{axoplasm}$ ratio of approximately 290 (see above) or 100x the difference in fluorescence intensity observed here. A likely explanation for the extreme difference between the theoretical and the observed TMRM ratio is that the confocal microscope's point spread function is significantly taller than the diameter of axonal mitochondria, causing a "dilution" of mitochondrial TMRM intensity. This effect is further intensified by an accumulation of TMRM in the myelin surrounding the axon (see also Romanelli et al. 2013) as well as in Schwann cell mitochondria (Gonzalez et al. 2015). Because of this, small shifts in the focus plane may also contribute to the large variance in TMRM measurements across axons. While computational approaches for approximating the correct TMRM intensity of mitochondrial pixels have been suggested (Fink et al. 1998; O'Reilly et al. 2003), they require the acquisition of multiple images at different Z planes followed by deconvolution, making them incompatible with time lapse recording and particle tracking.

The performance of the fully automated tracking approach developed here was significantly better than suited for my purposes than the previously used DifferenceTracker plugin. In fact, it slightly outperformed the comparison to manual tracking published by the authors in their original paper, even though the underlying data was acquired using much more stable nerve explants (Andrews et al. 2010). Importantly, it returned a full set of data with size, movement, and membrane potential which enabled some of the most interesting results in this chapter. Like the measurement of TMRM intensity, however, it was not without limitations: laser exposure was fairly

high and photo bleaching and the occasional depolarisation of single mitochondria was sometimes observed when imaging periods were extended to more than 60 seconds. Also, while it seemed well-suited to investigate differences in transport between treatment conditions, it did not provide an absolute quantification of mitochondrial movement and tended to underestimate it when compared with manual tracking.

Like in the pilot study, mitochondrial transport was observed in virtually all axons. The rate of transport observed here, however, was slightly lower. Whilst this might simply be a result of noise in the measurement, it is also possible that it is the result of switching from saline to aCSF as the medium surrounding the desheathed axons as at least one *in vitro* study suggests that using calcium free media increases mitochondrial transport (Zhang et al. 2010).

Conflicting reports exist about whether spatial constraints can lead to reduced mitochondrial transport (e.g. Pilling et al. 2006 vs Janakaloti Narayanareddy et al. 2014). Here, mobile mitochondria weren't found to slow down when passing close to (often larger) stationary mitochondria which suggests that the reduction in transport observed in the pilot study is likely not explained by a lack of intracellular free space.

A striking finding when studying mitochondrial dynamics in naïve animals was the complete absence of fusion and fission events. Such events are notoriously hard to detect automatically, particularly in a noisy *in vivo* setting where particles appear to change their size constantly by a few pixels due to movement artefacts. However, in over a thousand recordings of mitochondrial dynamics in axons (both here and in other chapters) I cannot point to a single fission/fusion event, which strongly suggests that they occur only rarely. I did not find evidence for kiss-and-run fusion, either. Although only transient, this kind of fusion is still considered to take a few seconds (Liu et al. 2009; Wang et al. 2012). There was no evidence of mobile mitochondria slowing down when they get close stationary mitochondria and it seems unlikely that mitochondria have enough time to fuse in a kiss-and-run fashion. The absence of fission and fusion may in part be explained by the fact the axons imaged *in vivo* are more mature then those imaged *in vitro*. Mitochondrial motility has been reported to decrease with age (Lewis et

al. 2016) and it has been suggested that mitochondrial fission and fusion may decline in the same way (Jendrach et al. 2005; Arnold et al. 2011; Figge et al. 2012).

In line with this absence of interaction between mobile and stationary mitochondria, I also did not find a significant correlation between the total area of stationary mitochondria and either anterograde or retrograde transport. This is perhaps surprising given the prevalent view that mobile mitochondria replenish stationary ones, yet it is also in line with findings by Misgeld and colleagues in nerve explants (Misgeld et al. 2007). Similarly, there was no significant correlation between anterograde and retrograde transport within the same axon.

As in the pilot study, retrograde transport was found to be significantly lower than anterograde transport. As mentioned in the discussion of chapter 2, this observation (as well as a tendency towards larger retrogradely traveling particles) has been described in multiple other studies: in the mouse saphenous nerve (Sajic et al. 2013), in mouse tibial nerve explants (Andrews et al. 2010), in excised frog nerve (Zhang et al. 2010), in drosophila larvae (Pilling et al. 2006) and in cultured neurons (Kiryu-Seo et al. 2010). The most extreme example actually stems from another *in vivo* study of the mouse saphenous nerve in which the authors note that "*Retrograde transport was not observed in the sciatic nerve of* [...] *untreated control animals*" (Bilsland et al. 2010). The most likely explanation for this phenomenon seems to be that a significant proportion of mitophagy takes place in the synapses and axon terminals. Alternatively, states of predominantly anterograde transport and states of predominantly retrograde transport may alternate, for example based on the hosts circadian rhythm (as seems to be the case for other mitochondrial processes: Peek et al. 2013; Neufeld-Cohen et al. 2016) although this seems far less likely.

Overall then, a picture emerges whereby mitochondria in the healthy saphenous nerve, rather than participating in constant exchange of material, are shuttled mainly from the soma towards the axon terminal with relatively few interactions along the way.

I was, however, able to confirm one finding which is in line with the classical idea of a mitochondrial life cycle: Like Miller and Sheetz I found that on average anterogradely

moving mitochondria have slightly higher membrane potentials than mitochondria moving back towards the soma (Miller & Sheetz 2004). However, whilst Miller & Sheetz did not directly measure membrane potential and instead manually categorised mitochondria as either high-potential or low-potential, the difference found here was small (about 5%) and definitely not visible by eye. The same was true for the difference in membrane potential between stationary and moving mitochondria which was found to be partially explained by the larger size of stationary particles. It is possible that larger mitochondria only appear brighter because the corresponding pixels contain less background intensity. However, the fact that movement had an effect on intensity even after correcting for size suggests that mitochondria in different states do indeed build up different membrane potentials and it seems very possible that larger mitochondria are able to build up higher potentials and therefore are more efficient producers of ATP as suggested previously (Liesa & Shirihai 2013; Hoitzing et al. 2015).

In conclusion, this chapter described the successful development and verification of methods for simultaneously tracking of mitochondrial movement and estimations of mitochondrial membrane potential. Applying these methods to the saphenous nerve of untreated mice yielded some interesting insights about mitochondrial dynamics in healthy axons, some of which (in particular the fact that mitochondria do not seem to be slowed down by nearby stationary particles) are relevant for understanding mitochondrial dynamics in demyelination. In the next chapter, the same methods are applied to study mitochondria at various time points throughout the course of de- and remyelination.

CHAPTER 4: TIME-COURSE OF DE- AND REMYELINATION AFTER TOPICAL APPLICATION OF LYSOLECITHIN

INTRODUCTION

Following the encouraging results of the pilot study I decided to study the relationship between demyelination and mitochondrial dynamics more closely. As mentioned previously, one of the advantages of the lysolecithin-based model used here is the swift progression from demyelination to virtually complete remyelination. Most of what we know about this process stems from a set of studies by Smith, Hall and Gregson (Hall & Gregson 1971; Gregson & Hall 1973; Hall 1973; Smith & Hall 1980; Smith et al. 1982). In the first of these studies, Hall and Gregson investigated the ultrastructural effects of lysolecithin injection in the mouse saphenous nerve. They reported an internode-by-internode swelling and unravelling of myelin, starting almost immediately after injection. The foam-like myelin debris was then taken up by macrophages, leaving most affected axons free from any surrounding myelin on days 4 and 6. Remyelination with gradually increasing myelin thickness was reported to occur from d9 to d25 ("*well established in the 14-day samples*") after injection and debris between axons was reported to be cleared fully after about three weeks. Importantly, the authors found that small variations in the concentration or amount of LPC solution injected changed the extent of the demyelination but not its time course. Two years later, a study by the same authors elaborated on these findings, adding that on day 14 every pre-demyelination internode seemed to be replaced by on average two new internodes, doubling the number of nodes of Ranvier and cutting the distance between them in half (Gregson & Hall 1973). Interestingly, this altered density of nodes, together with a significantly higher number of axon-associated cells was found to persist up to 90 days after treatment, and probably indefinitely.

A few years later, Smith and Hall investigated the functional consequences of demyelination. Similarly to the above studies, the authors report first, single layer

remyelination of individual axons at day seven and multi-lamellae remyelination of 70%-80% of axons at day 14. Whilst they found virtually all axons to be remyelinated after four weeks, maximal myelin thickness according to electron microscope images was not reached until 8 weeks after treatment (Smith & Hall 1980). When investigating the conduction properties of demyelinated axons, the authors report an initial burst of activity (seconds) followed by extensive conduction block on days 2-4. Over the period from day 6 to day 14, conduction was found to return gradually, albeit with compound action potentials with long, irregular tails of up to 5ms. This alternate, slower mode of conduction was particularly obvious in the refractory period of the first of a double stimulus (see methods) and was found even in nerves showing few signs of remyelination. In a subsequent publication using membrane current recordings with high spatial accuracy in rats, this new mode of conduction was shown to be facilitated by closely spaced, node-like foci which appear to assemble even in the absence of Schwann cells (Smith et al. 1982). Finally, at 60 days, remyelinated axons were found to have conduction properties indistinguishable from saline treated axons.

As laid out in the introduction, we thus have three distinct states of conduction (and presumably energy demand): early demyelination with total conduction block, early remyelination and the gradual return of microsaltatory, putatively more energetically expensive, conduction, and later remyelination where gross conduction properties are similar to untreated axons. In order to study mitochondrial dynamics and function in all of these conditions I decided to investigate mitochondria at days 2, 4 (early demyelination), 8, 12 (return of conduction), and 20 (more advanced remyelination). First, I investigated the state of myelination at these time points anatomically using semi-thin resin sections. In order to test whether the conduction properties reported earlier apply, I then recorded compound action potentials on days 8 and 12. Finally and most importantly I applied the methods for studying mitochondrial function and dynamics developed earlier to study mitochondria at all five time points in demyelinate axons compared with control axons. My goal is to combine observations about anatomical, electrophysiological, and mitochondrial changes in order to understand what might drive the changes in mitochondrial dynamics observed in the pilot study.

MATERIALS AND METHODS

ANIMALS

Animals used for this section were either male C57Bl/6 mice acquired from Charles River (anatomy and electrophysiology) or male Mito-S mice bred in-house (*in vivo* imaging). Ages commonly ranged from 8 to 12 weeks, never exceeding 16, and care was taken to ensure that treatment and control groups were age-matched, and wherever possible were litter mates.

All animal experiments were carried out according to the 1986 Animals (Scientific Procedures) Act, UK, and were approved by the institutional ethics committee.

SEMI-THIN RESIN SECTIONS

Animals (C57Bl/6J, n=2 per group (d2, d4, d8, d12, d20) plus n=2 naïve, n=12 total) underwent the demyelination procedure described in chapter 2 using 1% LPC on both hind legs. At the desired time points after treatment, animals were anaesthetized using isoflurane (3%) and euthanized via cardiac perfusion with heparinised buffered saline followed by a mixture of 4% paraformaldehyde (PFA) and 2% glutaraldehyde in phosphate buffered saline (PBS). The saphenous nerves were harvested and, post-fixed and embedded in resin as described in chapter 2. 0.7μm thick transverse sections were cut from the middle part of each specimen using an ultramicrotome (Reichert Ultracut S, Leica), stained with toluidine blue and examined and photographed using a Zeiss Axiophot microscope equipped with a Nikon D300 camera (Nikon, USA).

Images were processed using Fiji/ImageJ Version 1.48. Photographs of resin sections were converted to grayscale and contrast was optimised for each image such that the image's histogram covered the whole range of grey levels.

ELECTROPHYSIOLOGY

Animals (C57Bl/6J; naïve: n=3; d8 saline: n=3; d8 LPC: n=4; d12 LPC: n=4) underwent the demyelination procedure described in chapter 2 using 1% LPC on their left hind leg. After the desired time period, the saphenous nerve was exposed in the groin and at the ankle close to the foot, i.e. on either side of the demyelinated area. In the groin region, fat was removed from the surgical opening and the nerve was carefully separated from the surrounding tissue. A small piece of Teflon tape was placed between the nerve and the surrounding muscle tissue to provide insulation, and the opening was filled with mineral oil. A pair of stimulating platinum electrodes with hook-shaped ends was carefully placed under the saphenous nerve using micromanipulators. Stimuli were produced using a battery powered StimBox (DS2A, Digitimer). At the ankle, a small incision was made in the skin and the active recording electrode was placed in between the skin and the, in this region, very superficial nerve. A reference needle electrode was inserted in one of the toes and a ground electrode in the abdominal muscle. Active, reference, and ground electrode were connected to an amplifier (Neurolog System, Digitimer) via a headstage (NL100AK, Digitimer). The recorded signal was amplified (gain: 2000, NL104 AC preamp, Digitimer), filtered (8-10kHz; 50Hz notch filter; NL125, Digitimer), and recorded using a digital oscilloscope (Sigma 60, Nicolette Technologies). See Figure 4.1 for a sketch of the setup.

Two different stimulation protocols were used. Firstly, single CAPs were evoked using square, supramaximal stimuli (1.5 to 2.5 V, 50µs) at a rate of 1Hz. 100 traces were recorded from 1ms before the stimulus to 9ms post stimulus, at a rate of 5000 samples per second. Using custom Matlab scripts, traces containing large artefacts ("glitches") were filtered out and the remaining traces were averaged to yield a single CAP trace with a low noise level.

Secondly, a double stimulation protocol measuring the refractory periods of transmission (RPT) similar to the one developed by Ken Smith was employed (Smith & Hall 1980; Smith 1980). RPT has been shown to be a sensitive measure of conduction impairment which correlates well with the anatomical changes seen in demyelination (Smith & Hall

1980). It is less dependent on electrode placement than a comparison of CAPs which is particularly helpful given the spatial constrains in the current application. Briefly, instead of using a single stimulus, a pair of stimuli is given in short succession. Initially, while the first stimulus induces a CAP, the second one does not because of the axons' refractory period. However, as the inter-stimulus-interval (ISI) is increased, a second, smaller and partially overlapping CAP appears. The amplitude of this second signal increases with increasing ISI, as does the separation between the two response peaks in time. By subtracting the first response from the dual response it is possible to obtain a precise and visually striking representation of any changes to conduction speed and refractory period of the nerve.

First, 30 single stimuli were given at a frequency of 1Hz and the resulting CAPs recorded as described above. Then 30 double stimuli (two square stimuli of 50µs each) were recorded at the same rate. The initial delay between the two stimuli was 0.3ms. Blocks of single and double stimuli were alternated and the time between the double stimuli was increased in steps of approximately 0.1ms up to approximately 2.8ms. Using custom Matlab scripts, the resulting traces were filtered, averaged, and aligned at the stimulus artefact. In order to reveal the shape of the second CAP, each averaged single stimulus trace was subtracted from the corresponding averaged double stimulus trace and the resulting lines were stacked vertically (Smith 1980). See Figure 4.1 C.

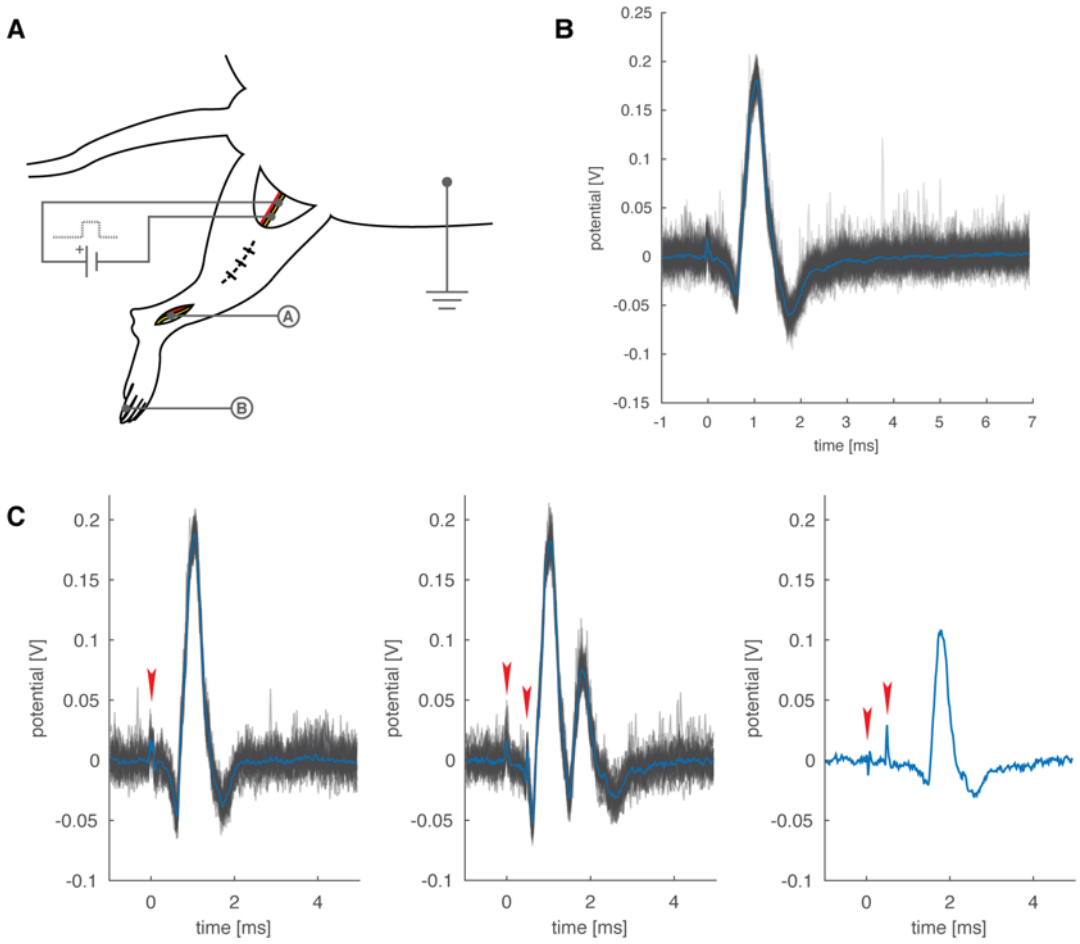

Figure 4.1: **Electrophysiology setup**. **A**) Setup: Stimulation in the groin region and recording near the foot (A and B indicate the two recording electrodes). The site of demyelination in between is undisturbed. **B**) Example of 100 raw CAP traces (dark grey) and the resulting mean trace (blue). **C**) Isolation of the second CAP after a double stimulus. **Left**: 30 CAPs recorded with a single stimulus and averaged. The red arrow head indicates the stimulus artefact. **Middle**: 30 traces induced by a double stimulus with a 0.7ms inter-stimulus interval. **Right**: Aligning the mean single and double trace at the first stimulus artefact and subtracting the first reveals the true shape of the second CAP.

IN VIVO IMAGING

Animals (CFP positive Mito-S; n=3 saline controls + n=3 LPC treated per time point: d2, d4, d8, d12, and d20; n=30 total) underwent the demyelination procedure described in chapter 2 using 1% LPC on their left hind leg. After the desired time period, they were prepared for imaging as described in chapter 3. Whenever possible, two animals (one LPC treated plus one saline control) were imaged in the same sitting.

Mitochondrial dynamics and membrane potential were recorded as described and verified in chapter 3, using 65 frame time lapses with simultaneous recording of CFP and TMRM. At least 15 axons were recorded for each animal. In addition, myelination was assessed using *SCoRe*, a recently published label free method which utilises the reflective properties of myelin by exciting the tissue with a relatively small number of photons of different wavelengths and capturing all reflected light with similar wavelengths (Schain et al. 2014). A *SCoRe* myelin reflection image was taken after recording CFP/TMRM time lapses to capture the myelination status of each axon. See Appendix B for a list of all excitation and recording wavelengths.

IMAGE ANALYSIS

Recordings were analysed as described in chapter 3. Data from axons which remained in-focus for less than 45 subsequent frames or had an axon length of less than 50μm were discarded.

STATISTICS

As before, the estimation of effect sizes and statistical significance testing was performed using a multi-level linear model with a fixed slope and random intercept via the *nlme* package for R. A separate model was constructed for each time point, using treatment as a fixed factor and animal ID as a random factor. R2 was estimated as the marginal R2 (i.e. the proportion of variance explained by the fixed factors alone) using the method developed by Nakagawa and Schielzeth (Nakagawa & Schielzeth 2013) as implemented in the piecewiseSEM package in R (Lefcheck 2015). Probability density estimates were calculated using Matlab's ksdensity function with a normal kernel. Corresponding confidence intervals were estimated via bootstrapping using 10,000 repeated draws of the same sample size as the original distribution. The 95% confidence interval for cumulative distribution functions was estimated using Greenwood's Formula.

THE TIMECOURSE OF DE- AND REMYELINATION AFTER APPLICATION OF LPC

The processing of most harvested nerves was successful, although three tissue samples ended up unusable. As in the pilot experiment (chapter 2), cross sections of the saphenous nerves showed clear signs of demyelination (Figure 4.2). The affected area appeared slightly larger in the current experiment, perhaps due to an increased proficiency at removing the surrounding tissue, and covered approximately 10 to 70% of the nerve's cross section. Importantly, the time course of de- and remyelination was very similar across all samples. Two days after application of LPC, virtually all axons were still surrounded by myelin but it appeared swollen and less optically dense than at the caudal end of the nerve. On day 4, the surrounding myelin debris was largely removed from the axon and affected areas contained completely demyelinated axons. A few axon cross sections (fewer than 5%) appeared dark and swollen, likely indicating dying axons. On day 8, a number of optically dense cells were found to be associated with the demyelinated axons and on day 12, a thin layer of myelin surrounding most axons could be seen. By day 20, this layer appeared increased in thickness, though still thinner than the thickly myelinated axons towards the deep side of the section.

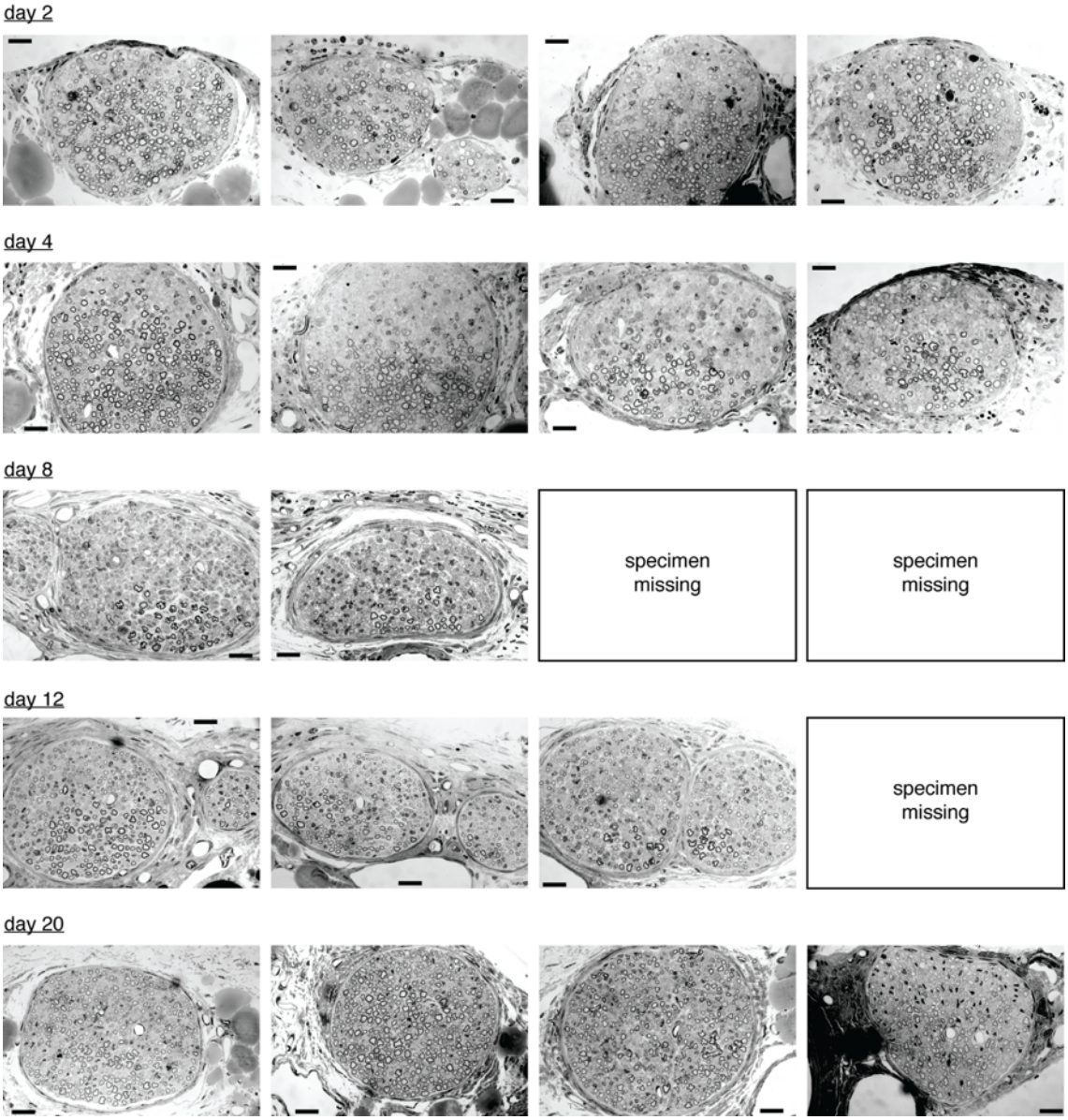

Figure 4.2: **Resin cross-sections of saphenous nerves at different time points after LPC application**. All sections are rotated such that the side of application points upwards in the image. Different animals were used for each time point and each row contains the left and right saphenous nerve from two animals. Some samples were lost during processing. Scale bars indicate 20μM. See text for details.

The time course suggested by the thin resin sections was further confirmed by *in vivo* imaging. From the very first time point (d2), nodes of Ranvier were absent from LPC treated nerves and not seen again until day 20. TMRM residue in the myelin surrounding the axon (the main *in vivo* indicator used in the pilot study) could not be seen on days 2, 4, and 8 and appeared only as a faint line on days 12 and 20. In addition to this

indirect marker, *SCoRe* reflection images were used to judge the state of myelination (See Figure 4.3). Unfortunately, in my hands at least, this technique was strongly dependent on the distance of the axon from the cover slip. Axons which were too far away from the glass showed only faint reflection signals whilst for the very top axons reflection from the glass itself saturated the detectors and masked the underlying tissue. Nevertheless, where images were available, they mirrored the resin sections shown above. On day 2, axons still showed myelin reflection, albeit with a smoother appearance and fewer details compared with control treated axons. No such reflections were seen on days 4 and 8 and only rarely on day 12. On day 20, however, most axons presented with *SCoRe* images similar to control axons. Apart from the limitations described above, the appearance of most axons at any given time point were uniform within and across animals.

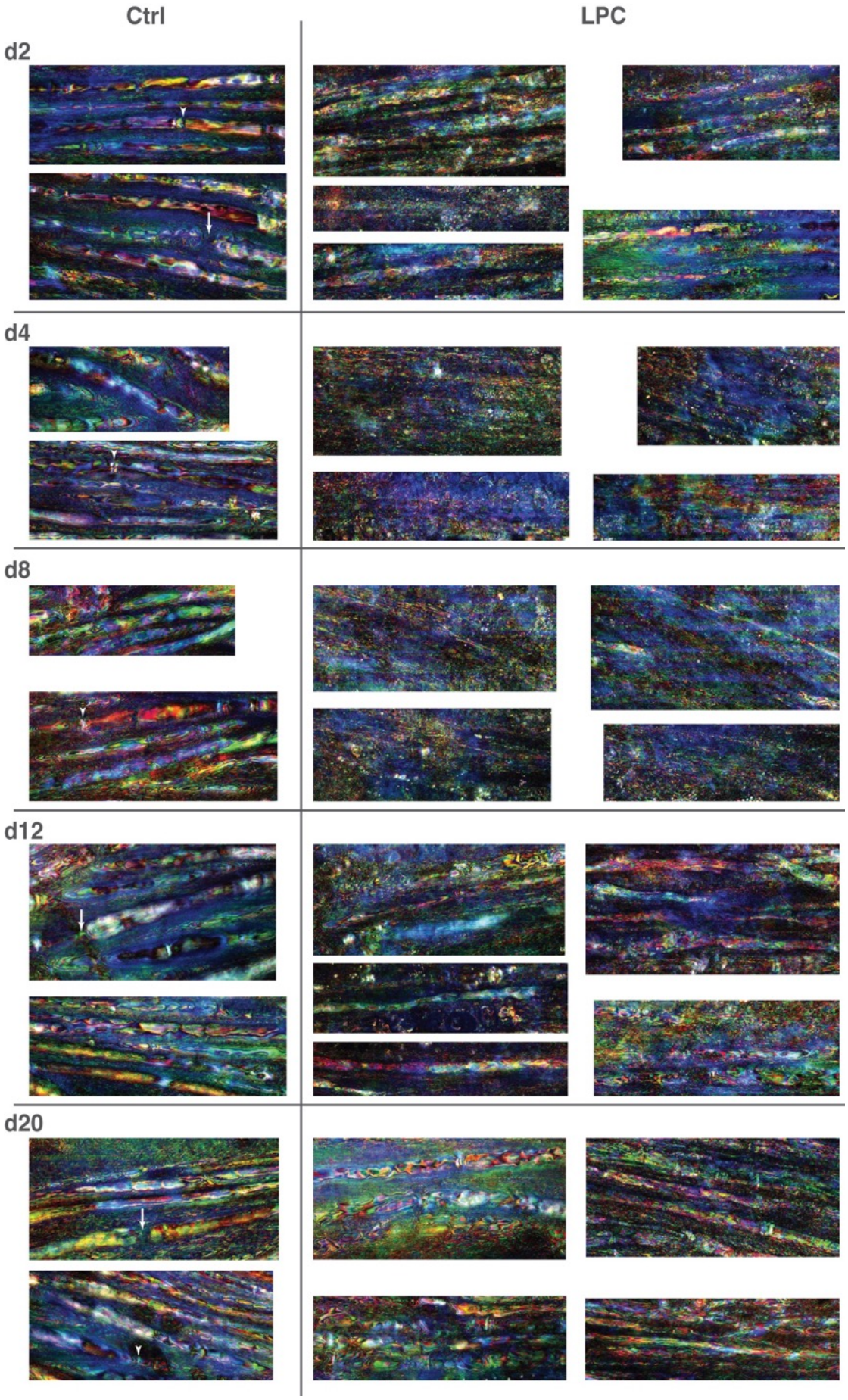
Ctrl
LPC
d2
d4
d8
d12
d20

Figure 4.3: **SCoRe reflection imaging over the time course of de- and remyelination**. Arrows indicate nodes of Ranvier, arrow heads point to potential Schmidt-Lanterman incisures. See (Schain et al. 2014) for comparison.

ELECTROPHYSIOLOGY OF THE DEMYELINATED SAPHENOUS NERVE

Compound action potentials were successfully recorded from animals at all four time points / conditions. CAP amplitude differed significantly between animals in the same condition, likely as a function of electrode placement and hence taken by itself proved to be an unreliable indicator of conduction. Similarly, there was no clear pattern in the minimum inter stimulus interval necessary to produce a second CAP which ranged from 0.3ms to about 0.8ms. However, there was a clear difference in the shape of the second CAP, particularly when stacked up into a "3D array" (Smith 1980). While differing in amplitude, CAP stacks from both naïve animals and saline treated animals on day 8 after treatment showed a sharp rise and fall leading into a flat line within less than 1.5ms across all inter-stimulus intervals. On day 8 after LPC treatment, in contrast, CAPs showed multiple peaks with very small amplitudes stretched out over more than 2.5ms. By day 12, these had increased significantly in amplitude but the sharp rise of the CAP was still followed by a prolonged return phase with multiple peaks. Taken together, these measurements suggest that conduction in the treated nerves was still largely blocked on day 8 but returned in the form of micro-saltatory conduction with prolonged refractory periods after the first CAP by day 12.

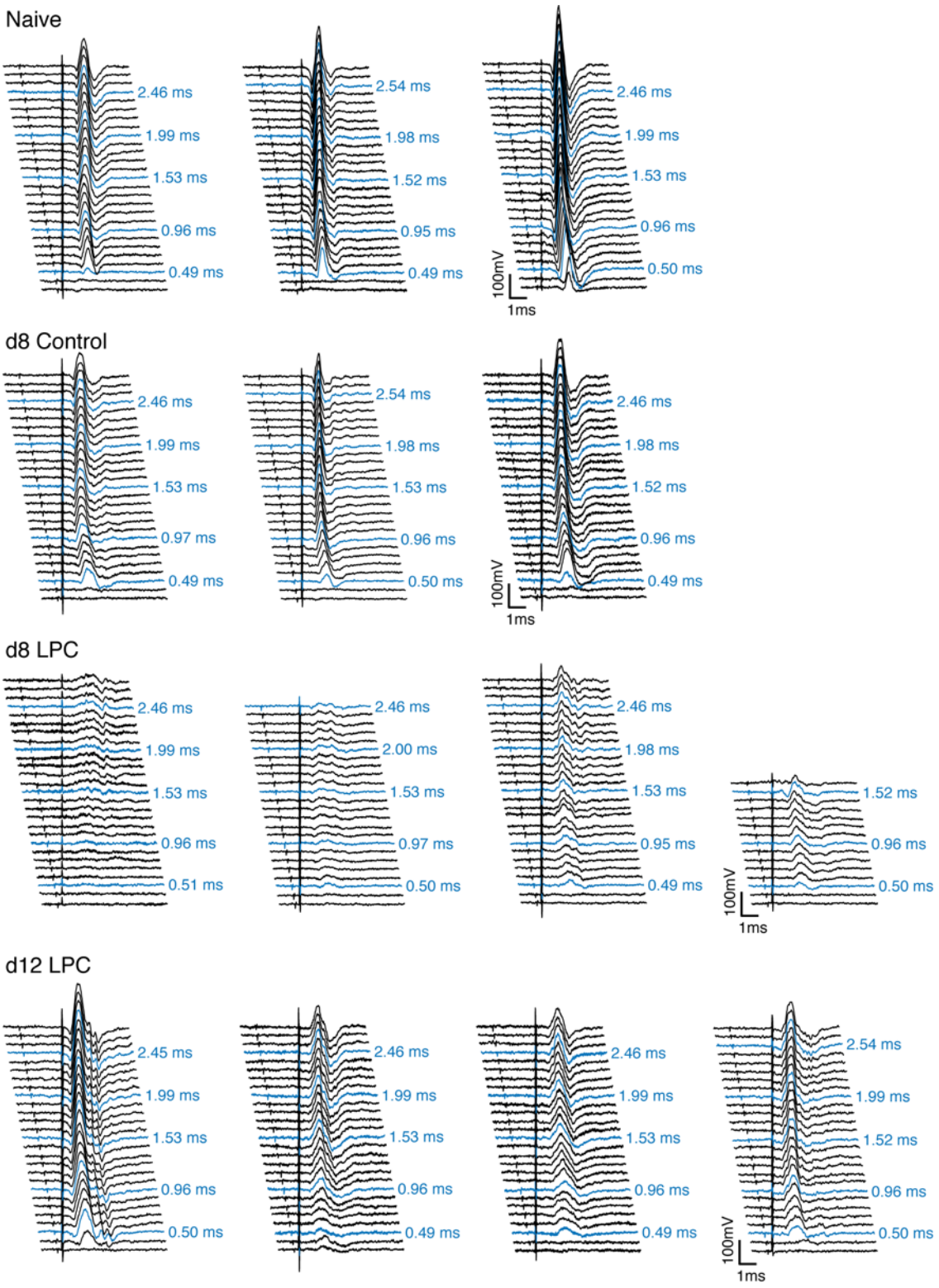

Figure 4.4: **Electrophysiological time course**. Each line shows the second compound action potential (2CAP) following a double stimulus. The time between the two stimuli increases from the bottom to the top in increments of approximately 0.1ms. Blue lines indicate similar stimulus intervals for comparison. **Top two rows**: 2CAPs rise and fall sharply in both naïve animals and saline controls. **Third row**: Conduction appears severely limited in LPC treated animals on day 8. 2CAPs are significantly smaller and

longer and show multiple peaks. **Bottom row**: By day 12, 2CAPs have increased in size but still appear abnormally long and with multiple peaks.

MITOCHONDRIAL FUNCTION AND DYNAMICS

After discarding unstable recordings and axons of less than 50µm length, the total number of recordings analysed in this experiment was 650 (saline control: 330, LPC: 320). In common with the pilot study and chapter 3, axons with CFP positive mitochondria were reliably expressed in the nerve and damaged / dying axons were clearly distinguishable from healthy axons. Although the penetration depth of LPC appeared increased compared with the pilot study, the total number of damaged axons was smaller, suggesting that at least some of the damage seen in the pilot study was caused by surgery rather than the application of LPC.

Axon width (defined as the width of the smallest rectangle around the straightened axon that could contain 98% of all mitochondrial pixels) was similar across all time points except for day 8 where it was found to be significantly increased compared with controls (ctrl: 4.24µm ± 0.16µm vs. LPC: 5.36µm ± 0.28µm, mean ± SE, $p<0.01$; Figure 4.5 A). However, as in the pilot study, this apparent increase in diameter co-occurred with an increase in the density of stationary mitochondria - on both day 4 and day 8, demyelinated axons contained an increased amount of stationary particles (d4: ctrl 13.30% ± 0.83% vs LPC 17.36% ± 1.41%, $p<0.05$; d8: ctrl 12.39% ± 0.40% vs LPC 19.85% ± 0.72%, $p< 0.001$; mean ± SE, Figure 4.5 B). This increase was also reflected in the size of stationary particles which was increased on day 4 and even more so on day 8 (Figure 4.5 C). The size of moving mitochondria, in contrast, remained stable except for a potential increase on day 2 (note however the very small number of day 2 observations, see below).

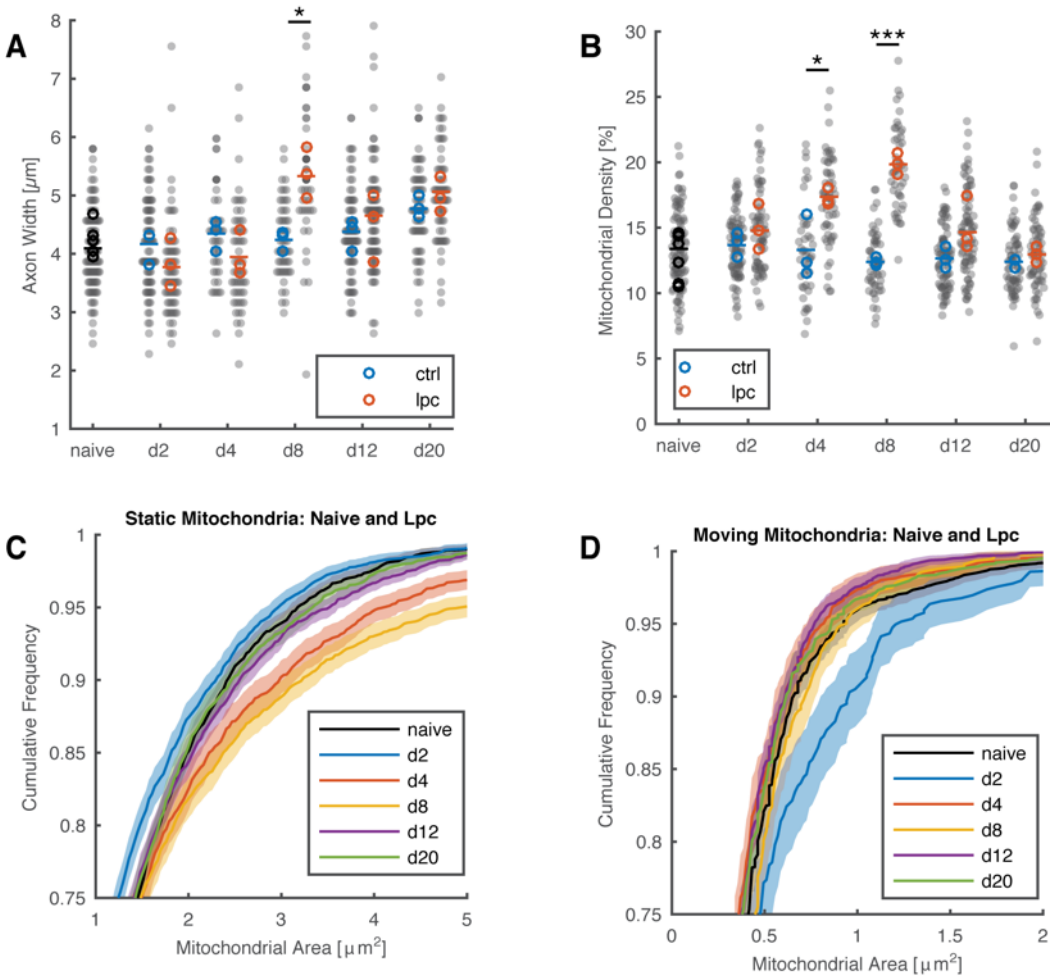

Figure 4.5: **Mitochondrial size and density**. **A**: Axon width. **B**: Mitochondrial density. Grey dots indicate individual axons; circles indicate animal means. Naïve data are taken from chapter 3 and replicated for comparison. **C**, **D**: Cumulative density plots showing the size of stationary and moving mitochondria, respectively. Shadows indicate 95% CI of the mean.

I next analysed the effect of demyelination on mitochondrial transport. Transport was significantly reduced in the early stages of demyelination, particularly on days 2, 4, and 8 with both anterograde and retrograde transport affected and on day 12, on which retrograde transport was found to be significantly different to controls (see Figure 4.6 A and Table 4.1). This reduction in transport was particularly striking on day 2, in part because mitochondrial size and density was still very similar to control axons, leaving large intra-axonal spaces with no mitochondria passing them. This experiment thus replicated the reduction in transport seen in the pilot study. There were, however, a few differences. The reduction seen here on day 8 was 58.5% and 48.2% for anterograde and

retrograde transport, respectively, which was lower than the 74.3% and 76.7% reductions observed on day 7 in the pilot study. Moreover, the reduction in transport speed seen on day 7 in the pilot study was not found here: Instead, particles moving in either direction showed a narrow range of speeds with the possible exception of anterogradely moving particles on day 2 which were found to move slower on average (Figure 4.6 C). Instead, the difference in transport was mostly explained by a smaller number of moving particles and shorter track lengths, indicating more frequent stopping (Figure 4.6 B).

Day	**Direction**	**Saline control [AU]**	**LPC [AU]**	**p**
d2	anterograde	1.04 ± 0.06	0.19 ± 0.11	< 0.0001
	retrograde	0.29 ± 0.04	0.12 ± 0.07	< 0.05
d4	anterograde	1.80 ± 0.19	0.73 ± 0.33	< 0.05
	retrograde	0.47 ± 0.07	0.19 ± 0.13	< 0.05
d8	anterograde	1.72 ± 0.14	0.71 ± 0.24	< 0.01
	retrograde	0.56 ± 0.05	0.29 ± 0.10	< 0.05
d12	anterograde	1.65 ± 0.41	1.28 ± 0.70	n.s.
	retrograde	0.69 ± 0.07	0.42 ± 0.12	< 0.05
d20	anterograde	1.66 ± 0.33	1.11 ± 0.57	n.s.
	retrograde	0.34 ± 0.05	0.45 ± 0.08	n.s.

Table 4.1: **Measurements of total transport** Total transport is defined as the average number of mitochondrial tracks seen at any given time point multiplied with their respective speeds. Values are mean estimates and SE according to a multilevel linear model with LPC treatment as the fixed effect and animal ID as a random effect.

A caveat of this result is that, in contrast to e.g. mitochondrial density or membrane potential, mitochondrial dynamics in saline treated axons varied markedly over time. This result is discussed further below.

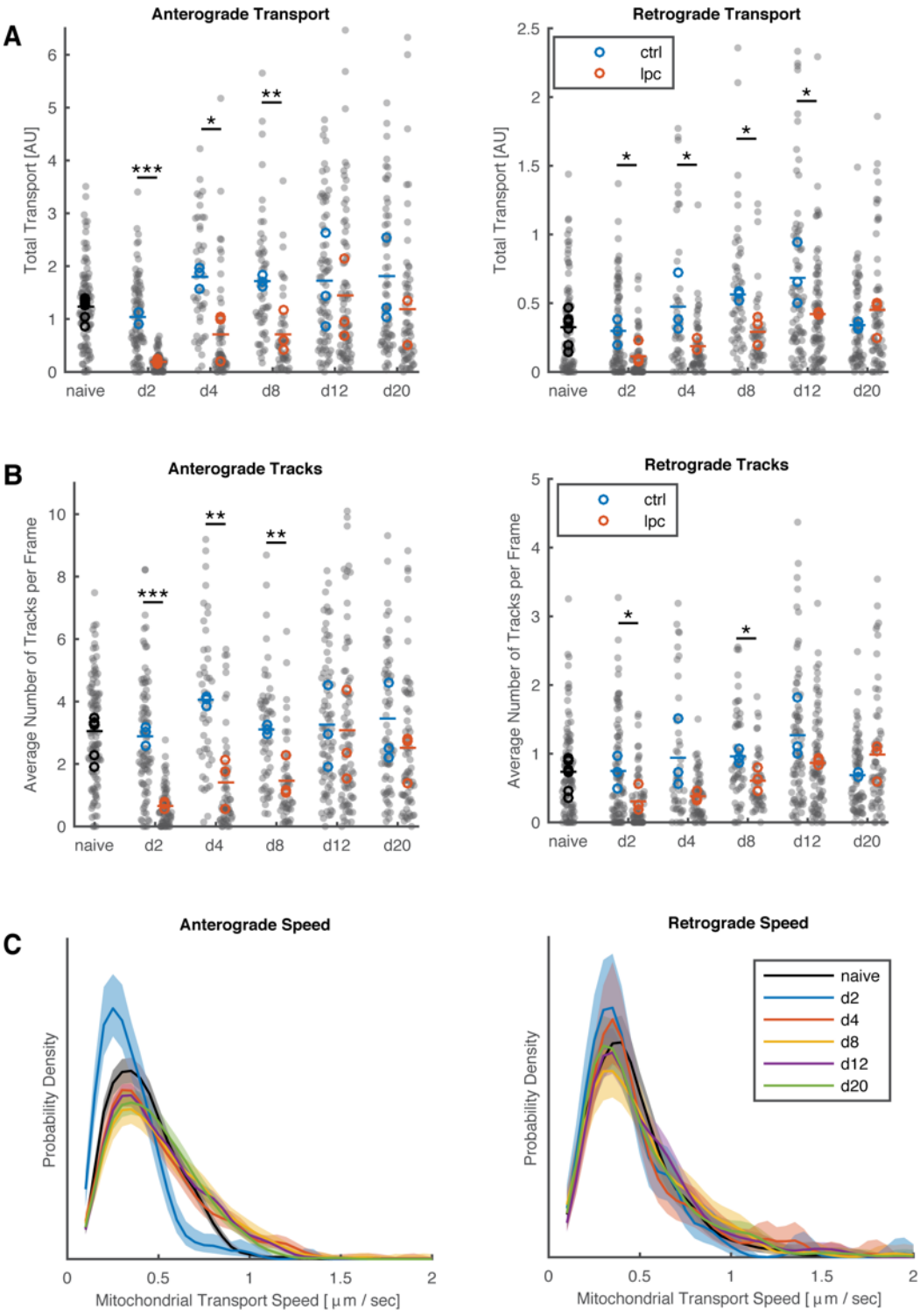

Figure 4.6: **Mitochondrial transport throughout the time course of demyelination**. **A**: Total anterograde and retrograde transport over time, defined as the average number of moving particles in any given frame multiplied with their respective speeds. **B**: Number of moving particles per frame. Grey dots indicate individual axons; circles indicate animal means. Naïve data are taken from chapter 3 and replicated for comparison. **C**: Distribution of transport speeds for untreated as well as LPC treated axons at different time points. Shadows indicate bootstrapped 95% confidence intervals of the mean.

One particularly interesting result of this set of experiments was the change in mitochondrial membrane potential: Stationary mitochondria in demyelinated axons presented with significantly higher TMRM ratios compared with controls on days 2 and 4 (d2: 4.74 ± 0.60 vs. 2.96 ± 0.34, $p<0.05$; d4: 3.57 ± 0.24 vs. 2.68 ± 0.15, $p<0.05$; mean ± SE). On day 2, this increase was strong enough to be obvious by eye. On day 8, the ratio was virtually identical to controls (2.85 ± 0.17 vs. 3.01 ± 0.10, n.s.) only to fall to below-control levels on day 12 (2.30 ± 0.17 vs. 2.91 ± 0.10, $p<0.05$). This trend was mirrored by moving mitochondria, although the difference on day 2 was not significant in this case. Importantly, the effect could not only be seen in measurements of TMRM intensity relative to the axoplasm, but also in the TMRM intensity of mitochondrial pixels alone (without background normalisation), suggesting that the change was driven by a true increase in mitochondrial membrane potential rather than just a decrease in background intensity due to the removal of TMRM.

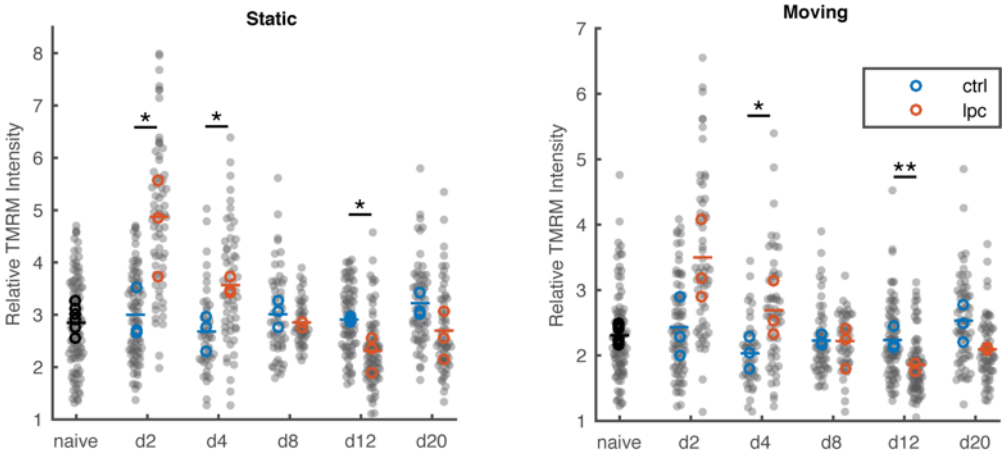

Figure 4.7: **Mitochondrial membrane potential over the time course of demyelination**. Grey dots indicate individual axons; circles indicate animal means. Naïve data are taken from chapter 3 and replicated for comparison.

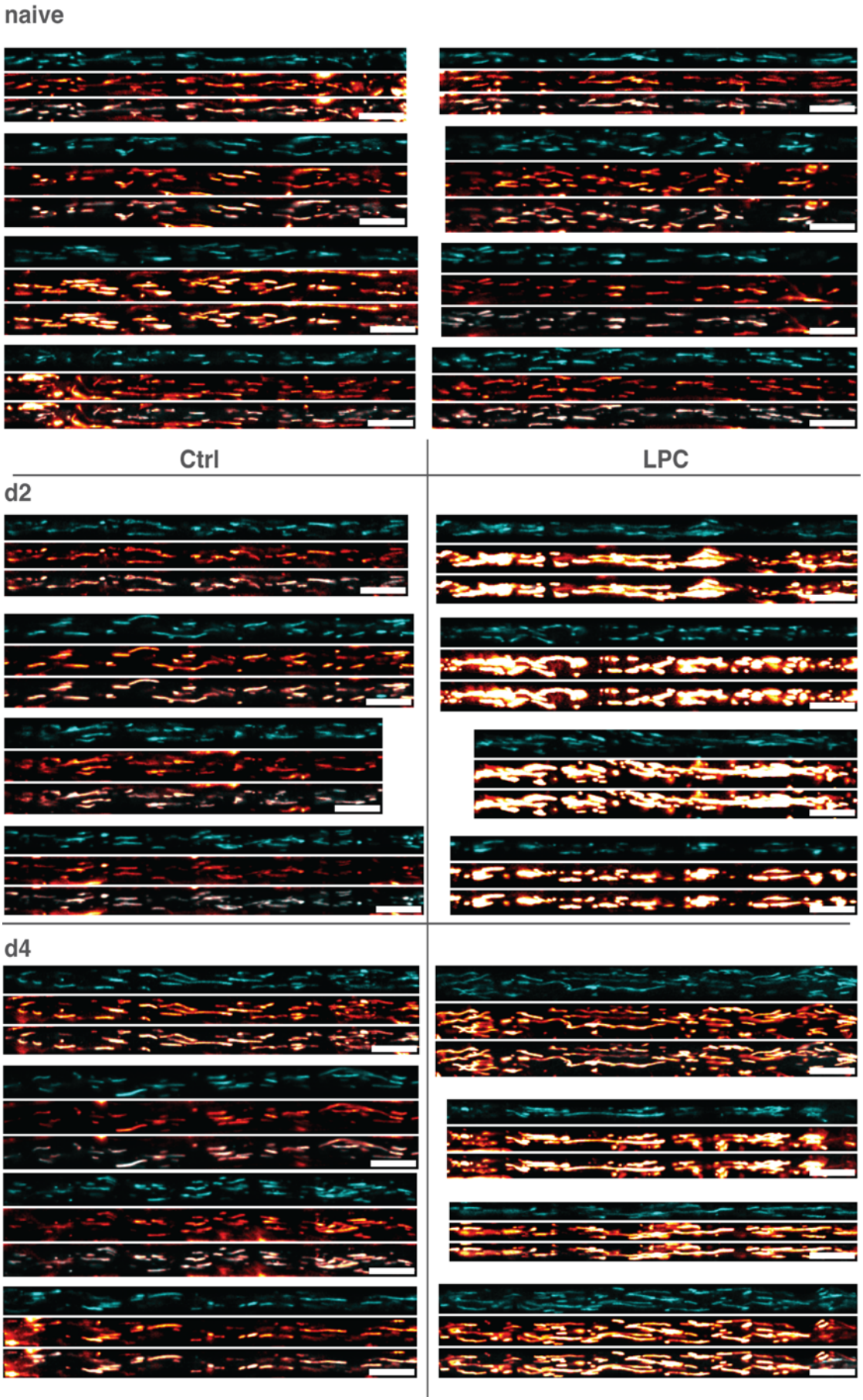
naive
Ctrl
LPC
d2
d4

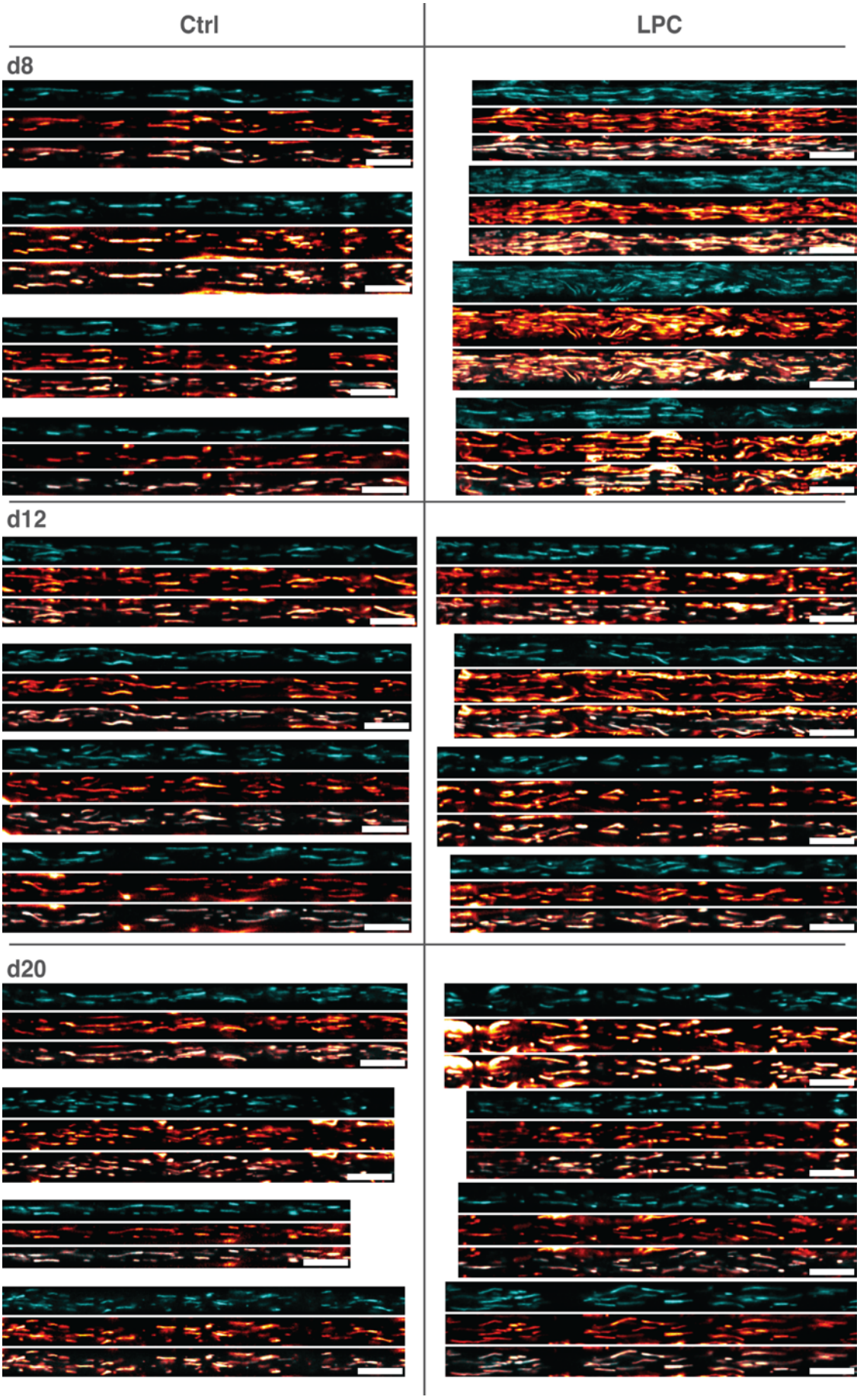
Ctrl
LPC
d8
d12
d20

Figure 4.8: **Representative images of axons taken at various time points throughout the time course study**. Genetically encoded CFP in cyan and TMRM in red. TMRM images were normalised to the background (defined as the 25th percentile of all pixels in the image) and the Fiji look-up table Red Hot was applied to emphasize differences in TMRM foreground intensity. Note the apparent increase in membrane potential on days 2 and 4 as well as the striking increase in mitochondrial density on day 8. Scale bars indicate 10μm.

DISCUSSION

Before investigating the role of mitochondria I first set out to map out the anatomical and functional time course of lysolecithin-induced de- and re-myelination. Overall, my findings were in good agreement with previous literature. Anatomically, the finding that most affected axons were not surrounded by any myelin on day 4, the first signs of early remyelination on day 8 and the more advanced remyelination seen on day 12 and particularly 20 were in good agreement with the findings of Smith, Hall, and Gregson laid out above. There was, however, a difference in the spread of demyelination. Despite using a comparatively low dose of LPC, axons were found to be demyelinated over much longer stretches and myelinated and demyelinated axons were rarely seen in the same image. This is in stark contrast to Gregson and Hall's finding that most axons only showed loss of myelin along the length of 2 to 3 internodes (Gregson & Hall 1973) and is likely a function of the difference in application. Whilst all papers cited in the introduction relied on microinjections of LPC in the nerve or white matter tract of interest, I opted for topical application (Griffin et al. 1990; Wallace et al. 2003), causing a much wider spread of lysolecithin along the nerve. Arguably, a lesion which allows for comparing myelinated and demyelinated sections of the same axon would have been more desirable, however, I found the small diameter of the saphenous nerve incompatible with injections. Nevertheless, the proportion of degenerating axons seen in the resin sections was very low, suggesting that whilst extending the lesion my choice of LPC application did not cause additional damage to the axons.

The extent of demyelination over the nerve's cross section seen here was comparable to previous reports based on topical application of LPC (Wallace et al. 2003 (40% of axons))

and, in fact, not too dissimilar from the numbers reported by Smith and Hall (Smith & Hall 1980 (53% of axons on average)) although no nerve was seen which came close to the reported maximum of 95% from the latter study.

My studies also suggest that the recently published *SCoRe* imaging procedure is useful for confirming demyelination *in vivo*, at least on an animal by animal basis.

In order to find the onset of return of conduction, a previously published double stimulus electrophysiology protocol was employed. However, CAPs recorded by me were wider than in the original study by Smith and Hall and the inter stimulus interval necessary to evoke a second CAP was noticeably larger, even in naïve axons. In part, the slower dynamics might be explained by the different fibre composition of the two nerves: whilst the sciatic nerve investigated by Smith and Hall is a mixed nerve with many fast motor axons, the saphenous nerve is purely sensory, including a large number of slowly conducting C fibres. More likely, however, it was also influence by suboptimal recording conditions. Smith and Hall went to great lengths to ensure a constant temperature of the nerve and all surrounding tissues, going so far as to submerge the whole animal in a temperature controlled bath of mineral oil. In the setup used here, in contrast, the leg was warmed only with a heating lamp controlled according to the animal's rectal temperature rather than a more precise probe measurement next to the nerve. Hence it is possible that the final temperature of the nerve, whilst fairly stable over time, was below the 37C. As both conduction speed and refractory period are very dependent on temperature (personal communication, Ken Smith) this might explain the slower speeds measured here.

Nevertheless, the time of return of conduction seen here was largely in agreement with previous findings, if perhaps slightly delayed. While conduction in the majority of axons was still be conduction blocked on day 8, elongated second CAPs with multiple peaks were observed in recordings from LPC based axons on both day 8 and 12. This suggests the onset of micro-saltatory conduction somewhere around this time, i.e. slightly later than originally reported (i.e. from day 6). However, this difference could easily be explained by the significantly longer lesions compared with the injection based study),

since conduction is restored to axons with short lesions before those with long lesions (personal communication, Ken Smith).

Taken together, the anatomical and electrophysiological findings suggest that the axons imaged on day 2 and 4 were electrically inactive. By day 8, a few of them had probably regained the ability to conduct action potentials, although their number was likely still low. On day 12, on the other hand, a substantial number of remyelinated axons seemed to be conducting in a slower, most likely micro-saltatory fashion. Conduction on day 20 is more difficult to predict as no electrophysiological recordings were conducted in this study and few data about similar time points can be found in the publications cited above. However, myelin thickness appeared significantly increased compared with day 12 suggesting that conduction might also be more similar to the axon's natural state. In terms of putative energy demand (or at least its conduction dependent component), one would thus expect a slightly decreased ATP consumption on days 2 and 4 and increased ATP demand in at least some axons on day 12 and perhaps day 8.

Given this background, it is striking that the observed decrease in transport was strongest not at the return of conduction, which is generally thought to cause an increase in energy demand, but, rather, early on in the course of demyelination, preceding the accumulation of stationary mitochondria. This is of methodological relevance as well, since it shows that the reduced transport found in demyelinated axons is not just an artefact of moving mitochondria being hidden by a larger number of stationary ones. One caveat of this finding is that the transport rates in controls varied significantly. Furthermore, they were found to be higher than in untreated axons. One possibility is that because experiments on naïve animals were conducted before the time series, followed by most d2 and d4 experiments, there may have been a training effect whereby later surgeries were more skilled and less disruptive to the axon. Alternatively, the control surgery and the resulting local environment around the nerve might stimulate increased mitochondrial transport, perhaps through damage to branches supplying the skin (compare e.g. Mar et al. 2014). Alternatively, there might have been slight differences for example in temperature control across experiments, leading to slightly different mitochondrial dynamics. However, one

LPC treated and one control animal each were imaged on the same day, meaning that many of the potential biases should apply to both groups.

In any case, there is little doubt that LPC treatment led to significantly compromised mitochondrial transport. Interestingly, the reduction in transport happened at a time when conduction in the axons was almost certainly blocked and was largely resolved by the likely time of return of conduction. Similarly, both density and size of stationary mitochondria peaked at time points when the axons most likely did not conduct action potentials. This calls into question the common assumption that mitochondrial changes in demyelinated axons are driven by increased ATP demand due to continuous conduction of action potentials (van Horssen et al. 2012). Other processes may drive up energy consumption in early demyelination. As mentioned in the introduction, upkeep of the axon's membrane potential is believed to account for a large proportion of white matter energy consumption even in healthy axons (Howarth et al. 2012). It is possible, that its cost increases further after demyelination due to increased leakiness of the membrane. Similarly, the cells "housekeeping" cost which is estimated to be similar in magnitude to the cost of membrane potential upkeep may be increased due to repair processes. Ultimately, direct measurement of the axon's ATP/ADP ratio (Imamura et al. 2009; Berg et al. 2009) would be necessary to conclusively rule out low ATP as the reason for the observed effects.

Alternatively, two other mechanisms seem well-suited to explain the time line observed here. The most obvious one is an increase in intracellular calcium. Ca^{2+} has long been recognized as one of the main influences on mitochondrial transport (see introduction). If intra-axonal Ca^{2+} is increased – either because the demyelinated axon is unable to effectively regulate calcium influx or due to a direct effect of lysolecithin – this would almost certainly lead to a reduction in mitochondrial movement (see introduction). Intracellular calcium levels are measured and discussed further in chapter 6.

Another possibility is that the reduction in mitochondrial transport is a direct consequence of conduction block. Work from our lab has shown that stimulation of the saphenous nerve leads to an increase in mitochondrial transport speed as well as an

increase in the number of moving mitochondria through fission of larger, stationary ones (Sajic et al. 2013). This suggests that perhaps decreasing neuronal activity might have the opposite effect, leading to a shift towards fusion as well as a decrease in mitochondrial transport. This theory is explored further in chapter 5.

The time course revealed here also raises interesting questions about the link between mitochondrial transport and the observed hyperfusion of mitochondria. Traditionally, calcium overload is associated with mitochondrial fission rather than fusion (Hom et al. 2007; Hom et al. 2012; discussion of Drp1 regulation in van der Bliek et al. 2013). However, in many cases this is in the context of a catastrophic event, so the putative Ca^{2+} increase here would likely be less extreme compared with the cited studies. Mitochondrial fission and fusion are often seen as stochastic events, with selective fusion controlled by membrane potential (Twig et al. 2008; Mouli et al. 2009; Tam et al. 2013). If moving mitochondria stop more often (as is clearly the case here) it is conceivable that the hyper-fusion observed on days 4 and 8 seen here is a direct consequence of them having more opportunities to merge. This mechanism might be boosted further by the observed increased membrane potential (see below). Alternatively, increased fusion has been shown to downregulate mitochondrial transport in dendrites as larger clusters of mitochondria fail to enter the small dendrites (Fukumitsu et al. 2016). However, many of the stationary mitochondria on day 2 were well within the normal size range of mobile mitochondria. Hence it seems more likely that hyperfusion is either a consequence of the decrease in mitochondrial transport or an independent event than the cause of reduced transaport. One possible transport-independent mechanism is cellular stress (Tondera et al. 2009; Gomes et al. 2011) and oxidative stress in particular (Shutt et al. 2012; Redpath et al. 2013), both of which have been shown to cause mitochondrial hyperfusion. LPC-mediated demyelination was shown to cause upregulation of the stress-induced transcription factor ATF3 (Kiryu-Seo et al. 2010) and an increase in reactive oxygen species due to changes in $\Delta\psi m$ might further drive fusion. Interestingly, Kiryu-Seo *et al.* suggest that ATF3 causes an increase in mitochondrial size as well as transport within 48h after LPC treatment. While my observations on day 2 seem to strongly contradict this finding it is conceivable that the stress response in the peripheral nerve is simply

delayed. Thus, even though I never observed the increase in transport reported by the authors, stress may support the return of mitochondrial transport which seems to coincide with the increase in mitochondrial density.

A particularly interesting finding was the sharp increase in TMRM signal observed on days 2 and 4. This finding has to be treated with some caution as lack of a myelin sheath surrounding the axon might lead to a reduction in background TMRM signal and hence an apparent increase in relative mitochondrial TMRM brightness (see also discussion of chapter 3). However, in semi-thin resin sections axon were still surrounded by a swollen layer of myelin on day 2 when relative TMRM intensity was highest. Furthermore, a change in background signal cannot explain the reduced membrane potential observed on day 12. One theory which fits well with the observed timeline is that increased $\Delta\psi m$ might simply be a function of reduced energy demand and hence mirror the increased membrane potential seen in conditions of excessive nutrient supply (Liesa & Shirihai 2013). This theory is explored further in chapter 5. However, it is worth noting that the increase seen here was significantly higher than the increase in $\Delta\psi m$ caused by oligomycin which suggests that something else must influence the membrane potential. As with hyperfusion, the potential influence of calcium is complicated. Larger increases in intracellular Ca^{2+} are known to cause a reduction of $\Delta\psi m$ (e.g. Abramov & Duchen 2008). However, as an important indicator of cellular activity, e.g. in synapses or muscle cells, calcium would also be well suited to cause dynamic upregulation of ATP production and over the last years a series of publications have emerged showing that moderate increases in calcium do indeed upregulate mitochondrial metabolism (Glancy & Balaban 2012; Rangaraju et al. 2014; Llorente-Folch et al. 2015). Using perhaps the most sophisticated methods to quantify $\Delta\psi m$ published so far, Gerencser *et al.* reported a 14% hyperpolarisation of mitochondria in cultured rat cortical neurons due to physiologically elevated levels of intracellular calcium (Gerencser et al. 2012) – a bigger difference than can be induced through blocking of the ATP synthase using oligomycin. It seems possible that a combination of moderately increased calcium levels and decreased ATP consumption might cause the observed increase in membrane potential.

Another factor which has been shown to boost $\Delta\psi m$ is the presence of neurotrophic factors (Huang et al. 2005). Schwann cells are known to produce large quantities of neurotrophic factors such as NGF, BDNF, NT-3 and NT-4/5 in reaction to axon injury (Frostick et al. 1998) which could in theory influence mitochondrial membrane potential in the nearby axons. However, the increase in neurotrophic factors usually lasts for weeks which seems incompatible with the brief increase and subsequent fall in membrane potential observed here.

Finally, a few potential caveats of this study need to be addressed. Firstly, the fact that some of the most extreme changes occurred at the earliest time point raises the obvious questions whether LPC itself might cause the reduction in mitochondrial transport. Two observations argue against this: firstly, as discussed in the introduction of chapter 2, LPC is quickly deactivated *in vivo* whereas the effects on mitochondrial transport lasted for days. Secondly, Kiryu-Seo *et al.* showed that LPC does not have an effect on mitochondrial transport or size when applied to unmyelinated axons *in vitro* (Kiryu-Seo et al. 2010). I furthermore tried to address these concerns in a control experiment using a different demyelinating agent (see Appendix C). Secondly, the reduction in mitochondrial transport could be caused by inflammation. In other contexts such an animal model of multiple sclerosis (EAE), inflammation has been shown to arrest mitochondrial movement (Sorbara et al. 2014) and the peak of reactive oxygen species production by microglia / macrophages in the CNS after injection of lipopolysaccharides is also on day 2 (A L Davies et al. 2013). However, other observations are not consistent with the inflammation hypothesis. Firstly, the number of inflammatory cells in LPC lesions seen by me and others is very low. And secondly, the by-products of inflammation such as NO which impair mitochondrial trafficking also significantly reduce $\Delta\psi m$ (Nikić et al. 2011) which stands in contrast to the strong early increase in membrane potential observed here.

In summary, studying mitochondrial dynamics and function at different time points during demyelination helped further to illuminate the underlying processes. I was able to confirm the transport deficit discovered in the pilot experiments and the increase in mitochondrial mass reported elsewhere. However, both occurred at a time when axonal

conduction was very likely still blocked, suggesting that an increase in axonal energy demand due to alternate forms of conduction was not the underlying cause. Furthermore, I found a striking early increase in mitochondrial membrane potential. Potential mechanisms explaining these findings include elevated intracellular calcium, conduction block, and cellular stress. I test the first two in chapters 5 and 6.

CHAPTER 5: CHANGES IN MITOCHONDRIAL FUNCTION DUE TO DRUG-INDUCED CONDUCTION BLOCK

INTRODUCTION

The link between mitochondrial transport in axons and neuronal activity is only poorly understood. As mentioned in the introduction, calcium is generally excepted as the main signal causing mitochondria to stop at energetically demanding locations such as synapses (e.g. MacAskill et al. 2010). Calcium also enters axons during action potential propagation through voltage-gated Ca^{2+} channels at the nodes of Ranvier (Jackson et al. 2001) but reports on whether this leads to mitochondrial arrest are conflicting. Using cultured mouse hippocampal neurons, Obashi and Okabe report that field stimulation increases mitochondrial stopping while treatment with the sodium channel blocker tetrodotoxin (TTX) reduces it (Obashi & Okabe 2013). Similarly, Ohno et al report a reduction in the speed of mitochondrial transport at nodes during resting state, an overall decrease in transport during stimulation, and an increase in the number of mobile mitochondria after TTX application (Ohno et al. 2011); Chen and Sheng report a syntaphilin-dependent decrease in transport during KCl stimulation of cultured hippocampal neurons (Chen & Sheng 2013); and Zhang *et al.* describe calcium dependent recruitment of mitochondria to nodes of Ranvier during tetanic stimulation of excised frog nerves (Zhang et al. 2010). In contrast, research from our own lab suggests that physiological stimulation of the saphenous nerve leads to increased mitochondrial transport both in terms of speed and number of particles (Sajic et al. 2013). Finally, Beltran-Parrazal *et al.* report based on cultured rat cortical neurons that neither action potential firing (spontaneous or chemically induced), nor TTX treatment or removal of extracellular calcium have any effect on mitochondrial transport (Beltran-Parrazal et al. 2006). I do not have a conclusive explanation for the difference between these findings but potential candidates include the difference between *in vivo* and *in vitro* settings (e.g. the difference in age of the neurons mentioned in the introduction), different stimulation

protocols (see also discussion of Sajic et al. 2013), or the difference between central and peripheral axons. The last point seems particularly interesting given other differences in mitochondrial transport between the two populations. For example, injuring peripheral axons has been shown to upregulate mitochondrial transport *in vivo* whereas injury to central axons does not have the same effect (Mar et al. 2014; Smit-Rigter et al. 2016). This example also highlights that there are regulators of mitochondrial transport beyond calcium, many of which we do not fully understand.

Given the upregulation in mitochondrial fission and transport observed by Sajic *et al.* I decided to investigate whether blocking axonal conduction might have the opposite effect. Since the normalisation of mitochondrial transport coincided with the putative return of conduction in my time course experiment (Chapter 4), I reasoned that conduction block might cause some of the changes which occur in demyelination.

Experimental conduction block is commonly achieved using the pufferfish toxin tetrodotoxin (TTX) or through local anaesthetics such as lidocaine or bupivacaine. All three substances have in common that they block voltage gated sodium channels. However, TTX is highly toxic with an LD-50 of only 334 μg/kg in mice (Fisher Science Material Safety Datasheet) which makes it difficult to control, particularly close to the saphenous vein. Hence I chose lidocaine and bupivacaine to induce conduction block. Both drugs act mainly by blocking voltage gated sodium channels in a use-dependent manner – that is, the first action potential after drug application is usually unchanged but subsequent ones that follow closely in time are significantly diminished (Scholz 2002). To a lesser extent, they also block potassium and calcium channels. Although their mechanisms of action are similar, bupivacaine has a 4-10x stronger affinity to its target channels. Both drugs are usually given in combination with ephedrine in order to minimise absorption into the blood stream and prolong their duration of action. However, I decided not to add this drug in order to avoid the effects of decreased blood flow on mitochondria.

ANIMALS

Animals used for this section were either male C57Bl/6 mice acquired from Charles River (electrophysiology) or male Mito-S mice bred in-house (*in vivo* imaging). Ages commonly ranged from 8 to 12 weeks, never exceeding 16, and care was taken to ensure that treatment and control groups were age-matched and wherever possible litter mates.

All animal experiments were carried out according to the 1986 Animals (Scientific Procedures) Act, UK, and were approved by the institutional ethics committee.

ELECTROPHYSIOLOGY

Different combinations of local anaesthetics and means of application were tested in order to achieve a reliable, prolonged conduction block. Initially, animals were prepared for surgery similarly to the demyelination procedure and had a small pad of sterile Gelfoam (Pfizer) soaked in a local anaesthetic implanted under the skin just above the saphenous nerve. After the desired time period, they were terminally anaesthetised and prepared for electrophysiological measurements as described in chapter 4. Multiple combinations of drugs and time periods were tried (see Table 5.1), however, none led to prolonged conduction block.

drug	time between implant and CAP recordings	result
2% lidocaine	48h	normal conduction
2% lidocaine	24h	normal conduction
5% lidocaine	24h	normal conduction
10% lidocaine	24h	terminated, cardiovascular side effects
1% bupivacaine	24h	normal conduction
1% bupivacaine	8h	reduced CAP amplitude

Table 5.1: **Different doses of local anaesthetics delivered through a Gelfoam implant in the leg**.

Since in my hands Gelfoam implants were not sufficient to cause a reliable medium-term conduction block, I investigated the duration of action of sub cutaneous bupivacaine injections instead. C57Bl/6 mice (n=3) were anaesthetised using isoflurane (5% induction, 1.5% maintenance). The hair was removed from their left leg using electronic hair clippers and hair removal cream and the underlying skin was sterilized using ethanol wipes. Then, an injection of 30µl of 1% w/Vol bupivacaine hydrochloride (Sigma Aldrich) in sterile saline was placed under the skin in the same area that was usually used for demyelination. The animal was left to recover for approximately 30 minutes after which it was re-anaesthetised and prepared for electrophysiological examination as described in chapter 5. 50 single stimuli at a frequency of 1Hz were given every 10 minutes starting approximately 80 minutes after injection and up to 190 minutes. Traces were filtered and averaged in Matlab.

IN VIVO IMAGING AND IMAGE ANALYSIS

Based on the measured electrophysiological effects of bupivacaine injection, I decided to investigate a conduction block of six hours induced by four injections in 90 minute

intervals. Animals (Mito-S, n=5 per condition) were anaesthetised with isoflurane (5% induction, 1.5% maintenance) and the inside of their left legs was shaved and sterilised. Then, 30µl of either 1% w/Vol bupivacaine hydrochloride (Sigma Aldrich) in sterile saline, or saline only, were injected s.c. above the saphenous nerve in the location used for the demyelination procedure in previous experiments. Subsequently, they were allowed to recover. The injection was repeated three more times in 90min intervals under light isoflurane anaesthesia. After the fourth time, the animals were terminally anaesthetised using urethane / ketamine and prepared for imaging as described before. Just before desheathing the nerve, bupivacaine was applied one last time. TMRM was applied at a concentration of 0.25µM in aCSF for 45 minutes and imaging was performed using the LSM 710 microscope and a Zeiss Appochromat Plan 63x oil objective (NA 1.4). Simultaneous CFP / TMRM time lapses were recorded as described above (at least 15 different axons per animal) and the resulting data were analysed as described in chapters 3 and 4.

STATISTICS

As before, the estimation of effect sizes and statistical significance testing was performed using a multi-level linear model with a fixed slope and random intercept via the *nlme* package for R, using bupivacaine treatment as a fixed factor and animal ID as a random factor.

RESULTS

RETURN OF CONDUCTION AFTER INJECTION OF BUPIVACAINE

The total time between the injection of bupivacaine and recording of the first CAP was about 80 minutes, including a 30 min recovery period after injection. At this time point, there was no sign of conduction in any of the three animals investigated. The first CAPs (defined as the first averaged recording with more than 4 standard deviations difference

from the baseline at any point) occurred after about two hours and CAPs didn't reach their full amplitude until at least 2.5h after injection (see Figure 5.1). Encouragingly, this time course was very similar across different animals. Based on these findings, I decided to use four injections of bupivacaine at 90min intervals to produce a conduction block of six hours.

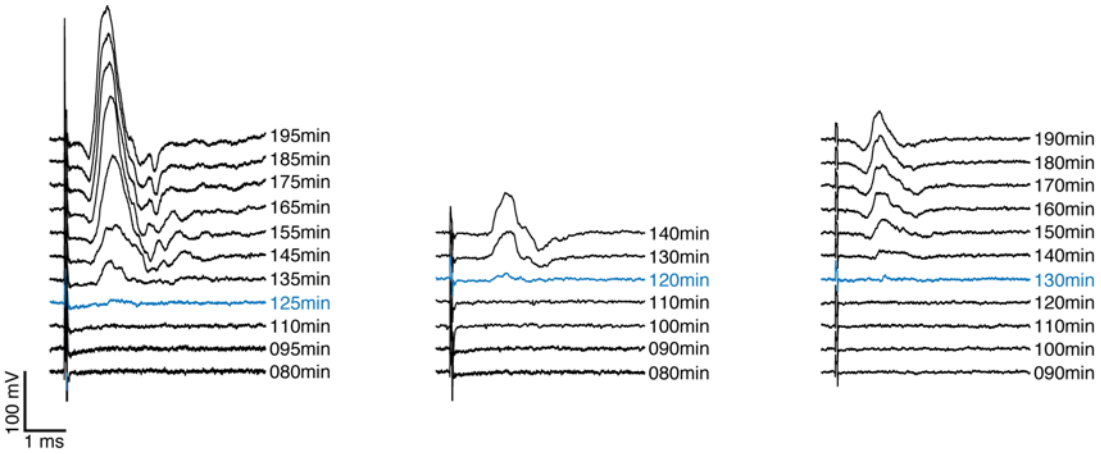

Figure 5.1: **Return of conduction**. Compound action potentials recorded from three different animals after subcutaneous injection of bupivacaine. The first detectable signal is indicated in blue (>4 standard deviations over baseline, 2500 samples). In all cases, conduction was blocked for at least 120 minutes.

MITOCHONDRIAL DYNAMICS AND FUNCTION IN CONDUCTION BLOCKED AXONS

When investigated under the microscope after 6h of conduction block, saphenous nerves appeared normal with no signs of mitochondrial or axonal changes compared with saline injected controls. This first impression was confirmed by subsequent data analysis. Mitochondria in bupivacaine-treated axons were virtually identical to those in saline-treated axons in all of the aspects measured in the previous chapters: mitochondrial size, density (saline 11.97% ± 0.26%, bupivacaine 12.68% ± 0.49%, $p > 0.12$), anterograde (saline 1.82 ± 0.31, bupivacaine 1.71 ± 0.57, $p > 0.81$) and retrograde (saline 0.38 ± 0.08, bupivacaine 0.39 ± 0.15, $p > 0.94$) transport, and relative TMRM intensity (saline

3.12 ± 0.10, bupivacaine 2.83 ± 0.18, $p > 0.10$). These values were similar to naïve and control values observed in chapters 3 and 4.

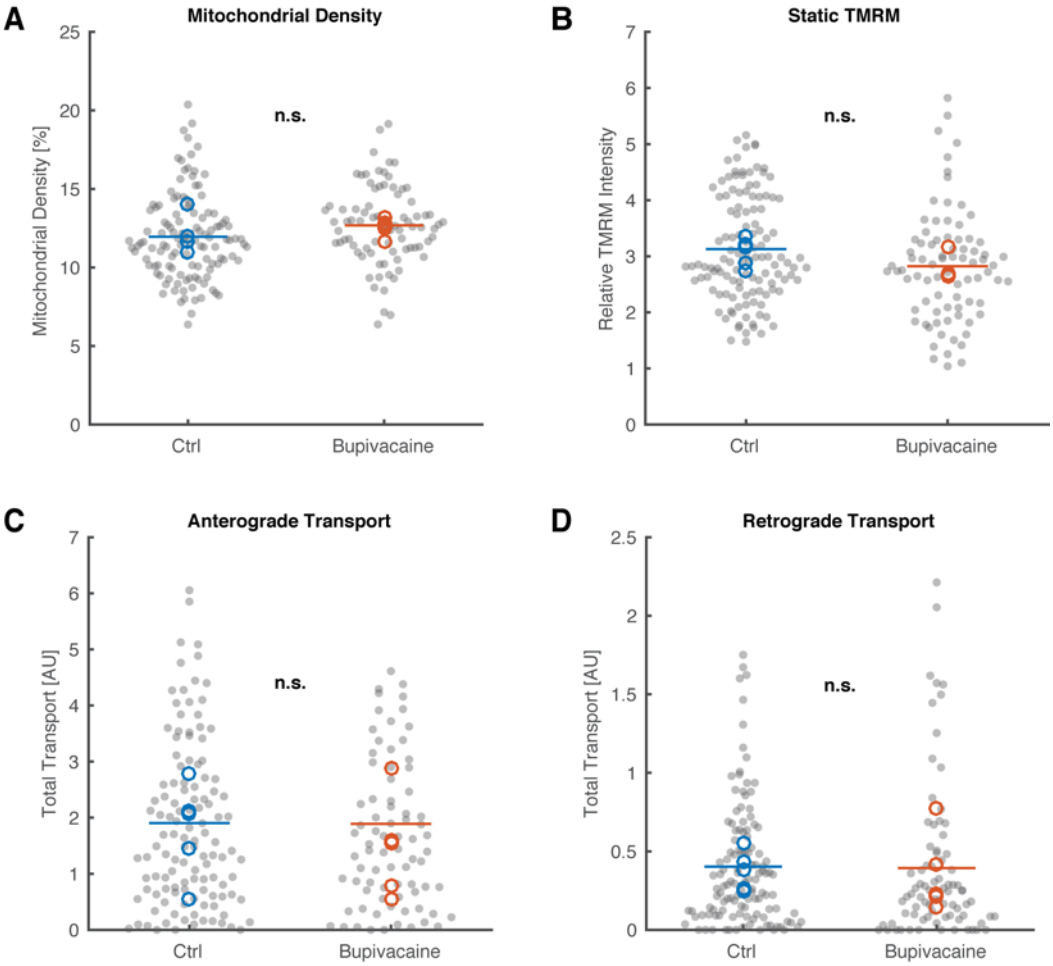

Figure 5.2: **Effects of 6h conduction block on mitochondria**. There was no significant difference between bupivacaine-treated and control axons for any of the properties investigated. Grey dots indicate individual axons; circles indicate animal means.

DISCUSSION

Conduction block over 6 hours using bupivacaine had no discernible effect on mitochondrial density, dynamics, or membrane potential. While the duration achieved here was significantly below the 48 hours of conduction block at the earliest time point investigated in chapter 4, it nevertheless provides evidence that the mitochondrial

changes observed early on in demyelination are unlikely to be caused by conduction block itself. Changes in mitochondrial transport and distribution due to TTX, for example, were reported as early as 15min (Ohno et al. 2011) or 30min (Obashi & Okabe 2013) after the application of the sodium channel blocker *in vitro*. Similarly, depolarisation of $\Delta\psi m$ due to stimulation and subsequent hyperpolarisation have both been reported to happen on the scale of tens of seconds (Gerencser et al. 2012). While the possibility cannot be excluded that a prolonged conduction block would induce changes similar to those seen in demyelination cannot be excluded, the results presented here suggest that conduction block is not the driver of the observed mitochondrial changes.

CHAPTER 6: CHANGES IN INTRA-AXONAL CALCIUM CAUSED BY THE APPLICATION OF LYSOLECITHIN

INTRODUCTION

As elucidated above, calcium is one of the most potent regulators of mitochondrial function and dynamics and elevated calcium levels could explain many of the phenomena seen so far from decreased mitochondrial transport to increased membrane potentials. Thus investigating intra-axonal calcium was a logical next step in trying to understand the chain of events linking demyelination and mitochondria.

Imaging-based measurement of Ca^{2+} has seen great advances in the last years. Today, calcium sensors are available both as injectable dyes such as Fura2 (Barreto-Chang & Dolmetsch 2009; Grienberger & Konnerth 2012) or OGB1 (Agronskaia et al. 2004; Lee et al. 2007), or as a variety of protein-based genetically encoded calcium indicators (GECIs) which can be delivered via viral constructs or inserted into the genome of mouse lines. GECIs can be further divided into single-fluorophore indicators such as GCaMP and dual-fluorophore indicators like Yellow-Cameleon or Tn-XXL (Grienberger & Konnerth 2012). When choosing an appropriate calcium indicator, the first important consideration is whether one desires to measure acute changes or compare baseline calcium levels in two different conditions. GCaMPs have been engineered to produce strong increases in fluorescence within fractions of a second upon calcium entry into a cell, allowing the detection of single action potentials in dendrites (Tian et al. 2009; Chen et al. 2013). However, since they only emit a single wavelength they do not provide a good way of quantifying resting state cytosolic Ca^{2+}. Tn-XXL in contrast is less bright and takes longer to change its emission in reaction to changes in calcium but since its readout is the ratio of two wavelengths rather than a change in brightness of one, it allows for the quantification of intra-axonal calcium "as is" without inducing a change. A second important attribute of calcium indicators is their Ca^{2+} affinity. Ca^{2+} affinity is the strength with which the indicator binds free calcium and is usually expressed through its dissociation constant K_d. K_d measures the likelihood that a calcium molecule will

separate from the indicator - hence low affinity indicators have a high K_d and *vice versa*. In theory, low affinity indicators are preferred as they buffer less calcium and therefore interfere less with the cell's physiology. In practise, however, higher affinity may sometimes be necessary to enable fast changes in the fluorescence signal (Grienberger & Konnerth 2012).

For this study, Tn-XXL was identified as the most suitable calcium indicator. As a dual-fluorophore indicator with a comparatively low affinity (K_d = 830nM), it is appropriate for measuring changes in resting state cytosolic Ca^{2+} (Williams et al. 2014; Siffrin et al. 2015; Luchtman et al. 2016). Importantly, a mouse line expressing Tn-XXL under the Thy1.2 promoter has been developed and extensively tested for behavioural and neurophysiological abnormalities (Direnberger 2011; Direnberger et al. 2012) giving us the opportunity to investigate intracellular calcium in a strain of mice and a subset of axons similar to those expressing mitochondrially targeted CFP. We received the mice as a kind gift from Oliver Griesbeck in Munich and bred them in house.

The Tn-XXL construct is made up of the fluorophores eCFP and Citrine cp174 which are connected via a modified version of the calcium binding protein troponinC (TnC) (Mank et al. 2008). TnC is a muscle protein and does not interfere with neuronal proteins, hence avoiding some of the long term physiological side effects and inactivation of indicator proteins reported for calmodulin-based GECIs (Hasan et al. 2004; Tian et al. 2009). Upon binding of Ca^{2+}, troponinC undergoes a conformational change which brings the two fluorophores closer together (see Geiger et al. 2012 for a rather impressive 3D rendering of the conformational change). This causes an effect known as fluorescence (or Förster) resonance energy transfer (FRET). FRET is a special form of quenching whereby energy is transferred non-radiatively from one excited fluorophore to another. Two conditions for FRET are a) that the emission spectrum of the first fluorophore and the excitation spectrum of the second fluorophore overlap and b) that they are within very close proximity of one another (1-10nm range). In fact, the rate of energy transferred falls with the 6th power of the donor-acceptor distance (Jares-Erijman & Jovin 2003). When using Tn-XXL for the quantification of intracellular calcium, only the CFP fluorophore is excited. As Ca^{2+} causes a conformational change of TnC that brings CFP

and Citrine closer together, a larger proportion of energy is transferred from CFP to Citrine, causing a shift in their emission ratio. This ratio can serve as semi-quantitative readout of axonal Ca^{2+}.

In order to better understand the effects of demyelination on intracellular calcium, I first optimized the imaging settings and analysis methodology for single photon measurements of Tn-XXL on our microscope. Axons were flooded with extracellular calcium using the Ca^{2+} ionophore ionomycin to gage the detection range (Siffrin et al. 2015). Then, I performed the demyelination procedure established above on Tn-XXL mice and compared intra-axonal calcium levels at an early (d2) and an intermediate (d8) time point.

MATERIALS AND METHODS

ANIMALS

Calcium imaging was performed using male, C57Bl/6J based Thy1-TN-XXL mice (Direnberger et al. 2012) which were kindly gifted by Oliver Griesbeck and bred in-house. Thy1-TN-XXL mice homozygously express the calcium sensor Tn-XXL (Mank et al. 2008; Geiger et al. 2012) in a broad range of neurons and were shown to have a healthy phenotype up to an age of at least six months (Direnberger 2011; Direnberger et al. 2012). The expression pattern in the saphenous nerve was similar to that of Mito-S mice with expression in myelinated axons but not in C-fibres. However, the level of expression was much more variable and Tn-XXL was seen in approximately 0-80% of all axons of a given animal with no obvious heritability pattern. See results for details.

All animal experiments were carried out according to the 1986 Animals (Scientific Procedures) Act, UK, and were approved by the institutional ethics committee.

IN VIVO IMAGING

For initial proof of concept, animals (Tn-XXL, n=5), were prepared for imaging as described above. No dyes were applied to the nerve and image acquisition was performed using a Zeiss Appochromat Plan 63x oil objective (NA 1.4). Axons of interest were identified by exciting the Citrine fluorophore of Tn-XXL directly via a 514nm laser, producing a crisp image with little background fluorescence and low laser power. Then, two 512x512px images were taken for every axon: a ratiometric two-channel image with an excitation of 405nm and detection ranges of 460nm - 510nm and 520nm - 570nm for CFP and Citrine, respectively, and an 'anatomical' image with 514nm excitation and a broad detection range of 515nm - 650nm (see Figure 6.1). Laser settings were left constant across all animals. Since a laser with the optimal excitation wavelength for Tn-XXL (around 432nm) was not available, some of the initial calibration experiments were conducted using both a 405nm laser and a 458nm laser for comparison. After all visible axons were imaged, the animal was removed from the microscope stage and ionomycin (100µM in aCSF) was applied to the nerve for 10 minutes. A new coverslip was placed on the leg and imaging was repeated.

To assess axonal calcium in demyelination, animals (Tn-XXL, $n_{d2} = 7$, $n_{d8} = 6$) underwent demyelination as described above with one change: since no dyes were used, the time from induction of anaesthesia to image acquisition was significantly reduced, making it possible to image both hind legs of any give animal. Hence, each subject served as its own control: one hind leg was treated with LPC and one with sterile saline. The treatment side was alternated. After the desired time period, animals were prepared for imaging as described in chapter 2. The left leg was imaged first. After all visible axons were recorded, the animal was removed from the microscope stage, the surgical opening in the leg was closed with 2-4 sutures of 6-0 polypropylene thread (Ethicon) and the cast of dental impression material carefully detached from the stage. Subsequently, the procedure was repeated for the right leg.

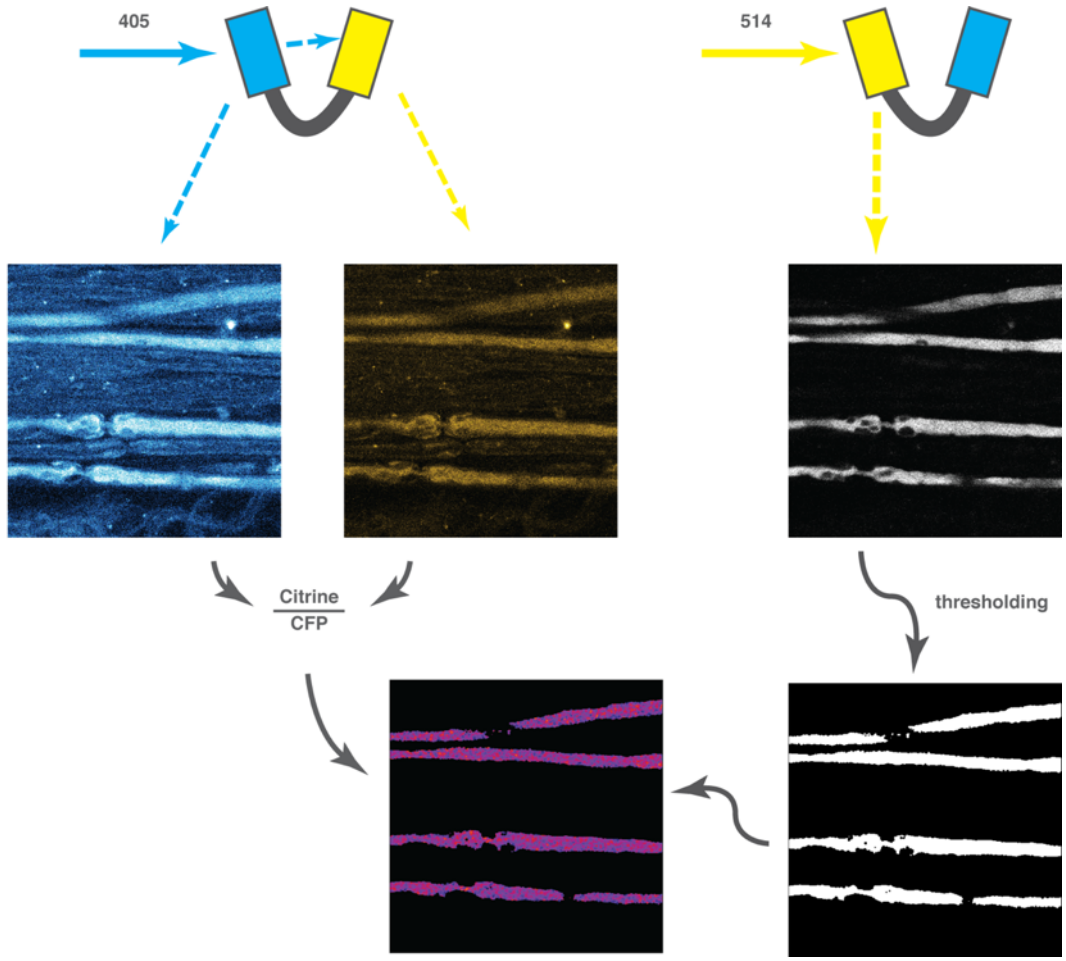

Figure 6.1: **Calcium imaging and analysis**. See text for details.

IMAGE ANALYSIS

Image analysis was performed using Matlab. First, all images were filtered using a 3x3px median filter to reduce noise. Individual axons were extracted by manually selecting a rough axon outline. Then, all pixels of interest were selected by thresholding the anatomical (Citrine-only) image. For each pixel of interest, the ratio of Citrine to CFP in the ratiometric image was calculated. A number of publications stress the importance of background subtraction in the analysis of calcium imaging data (Helmchen 2011; Niesner et al. 2013; Siffrin et al. 2015). However, in my hands, background subtraction

did not further enhance the detection range. Results are presented as the median pixel ratio per axon.

Conditions were compared on an axon-by-axon basis. Statistical significance was tested using the statistical software environment R. Using the *nlme* package, a two-level linear model with a fixed slope and random intercepts was fit to the data. The median pixel ratio per axon was used as the response variable, treatment/day as a fixed effect and animal ID as a random effect. See Appendix A for a discussion of this approach.

RESULTS

Tn-XXL expression in the saphenous nerve differed widely across animals (see Figure 6.2). It ranged from virtually every myelinated axon in the nerve expressing the indicator to less than a handful of axons, and even total lack of expression in the PNS (investigation of one zero expression animal revealed strong Tn-XXL signal in the hippocampus). Whilst the expression was similar between two legs of the same animal, it varied across littermates with no obvious correlation to the expression seen in their parents. However, peripheral Tn-XXL was more reliably seen in females than in males. Despite these differences, the level of expression (as indicated by fluorescence intensity) seemed uniform across all expressing axons, even across different animals.

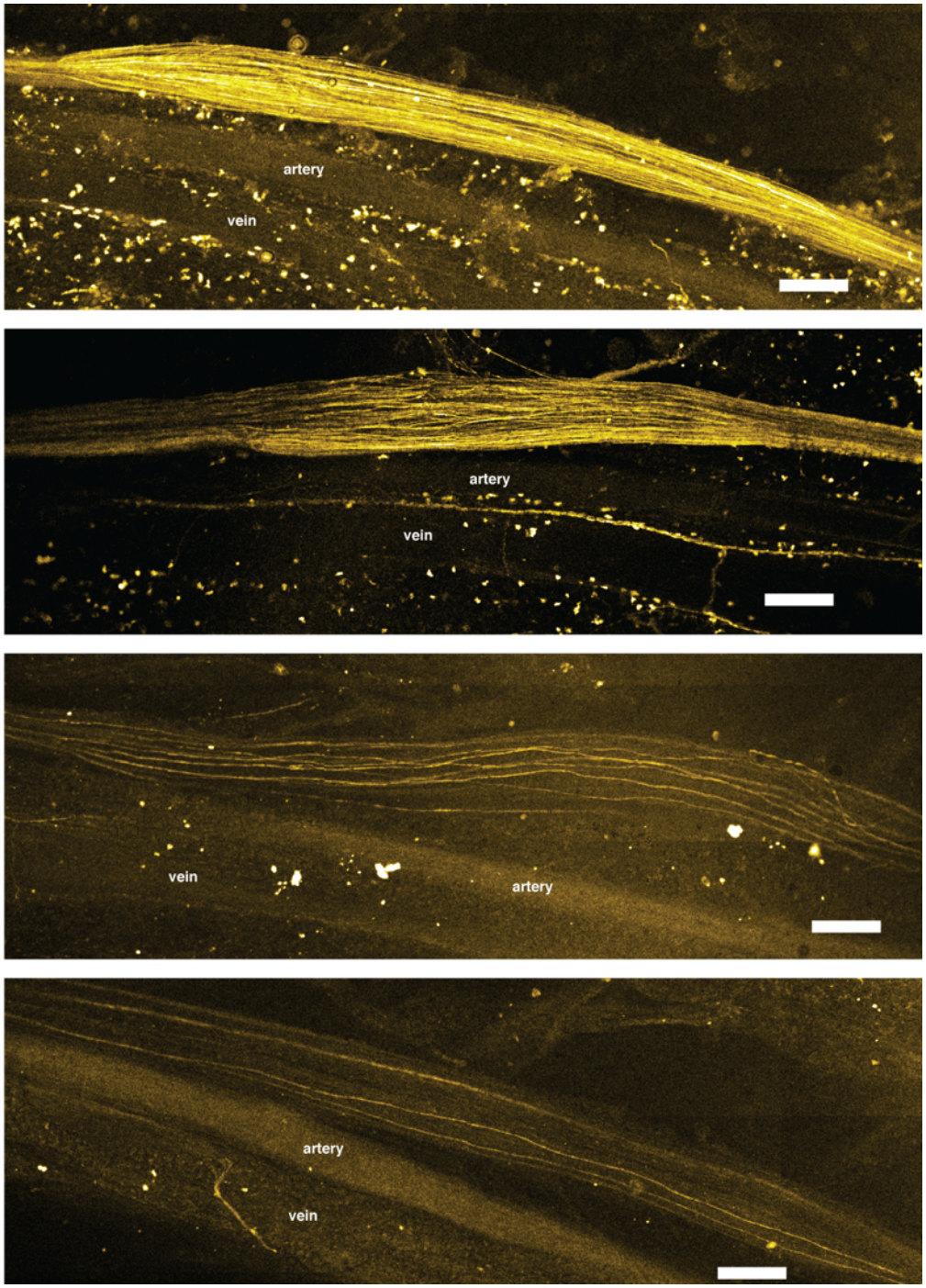

Figure 6.2: **Different expression patterns of Tn-XXL in the saphenous nerve**. Expression ranged from virtually every axon in the nerve to none. C fibres did not show expression. All images taken from naïve animals. Scale bars indicate 250µm.

In experiments using both a 405nm and the 458nm excitation wavelength for comparison, background fluorescence was significantly lower when using the latter. However, this wavelength also seemed to excite the Citrine fluorophore directly, leading to a reduced detection range. Thus, all subsequent experiments were conducted using 405nm

excitation. While the indicator's signal was strongest in the axoplasm of nerve fibres, many myelin sheaths were clearly visible, too (most obvious after ionomycin application, see Figure 6.4). This was surprising since this expression pattern had not been described (Mank et al. 2008; Direnberger 2011; Direnberger et al. 2012). However, reports of Thy1.2 promoted transgene expression in Schwann cells have been published (Livet et al. 2007) and since the sheaths were visible in Tn-XXL mice even when excited with 514nm light (a wavelength which typically does not produce autofluorescence) but never in Mito-S mice, it seems that Schwann cells do indeed express Tn-XXL.

In naïve animals, the Citrine to CFP ratio of axons was remarkably consistent across animals (mean: 0.267 ± 0.007 SE, n = 5 animals, 257 axons; see Figure 6.3 A). Upon application of ionomycin, it increased significantly by 0.176 ± 0.004 (mean and SE, $p < 0.001$), enough to be visible by eye. At the same time, the treated axons changed shape to a bead-like appearance with swellings and constrictions. The effects of demyelination were less strong but still highly significant (Figure 6.3 B and D) and occurred in every animal. At day 2 after treatment, the fluorescence ratio in demyelinated axons was increased by 0.02 ± 0.004 (mean and SE, n=7 animals, 219 vs 172 axons, $p<0.001$) and at day 8 by 0.04 ± 0.005 (mean and SE, n=6 animals, 125 vs 140 axons, $p<0.001$). Differences between the control treatments on days 2 and 8, between control treatments and untreated axons, or between LPC treated axons on days 2 and 8 were not significant. Some of the demyelinated axons showed calcium indicator ratios similar to those seen after ionomycin application. In order to make sure that the observed effects were not caused by axons with catastrophic levels of intracellular calcium, I removed all axons with fluorescence ratios within two standard deviations of the mean of ionomycin treated axons from the analysis (Figure 6.3 D). Importantly, the differences between myelinated and demyelinated axons remained significant with $p<0.001$.

In order to determine whether the increase in calcium and / or the measurement thereof was influenced by axon diameter, the correlation between fluorescence ratio and axon width was determined for demyelinated axons on both days. No correlation was found between putative calcium levels and axon diameter (Figure 6.3 C) and axon diameters seemed virtually identical for naïve, saline treated, and demyelinated axons (4.10µM,

4.26μM, and 4.10μM, respectively; differences not significant). Myelin in LPC treated nerves appeared disrupted but mostly still in proximity to the axons on day 2. On day 8, axons appeared virtually free from myelin and obvious clusters of debris could be seen between them. No nodes of Ranvier were seen on either day in demyelinated axons and no beading as seen after ionomycin treatment was observed.

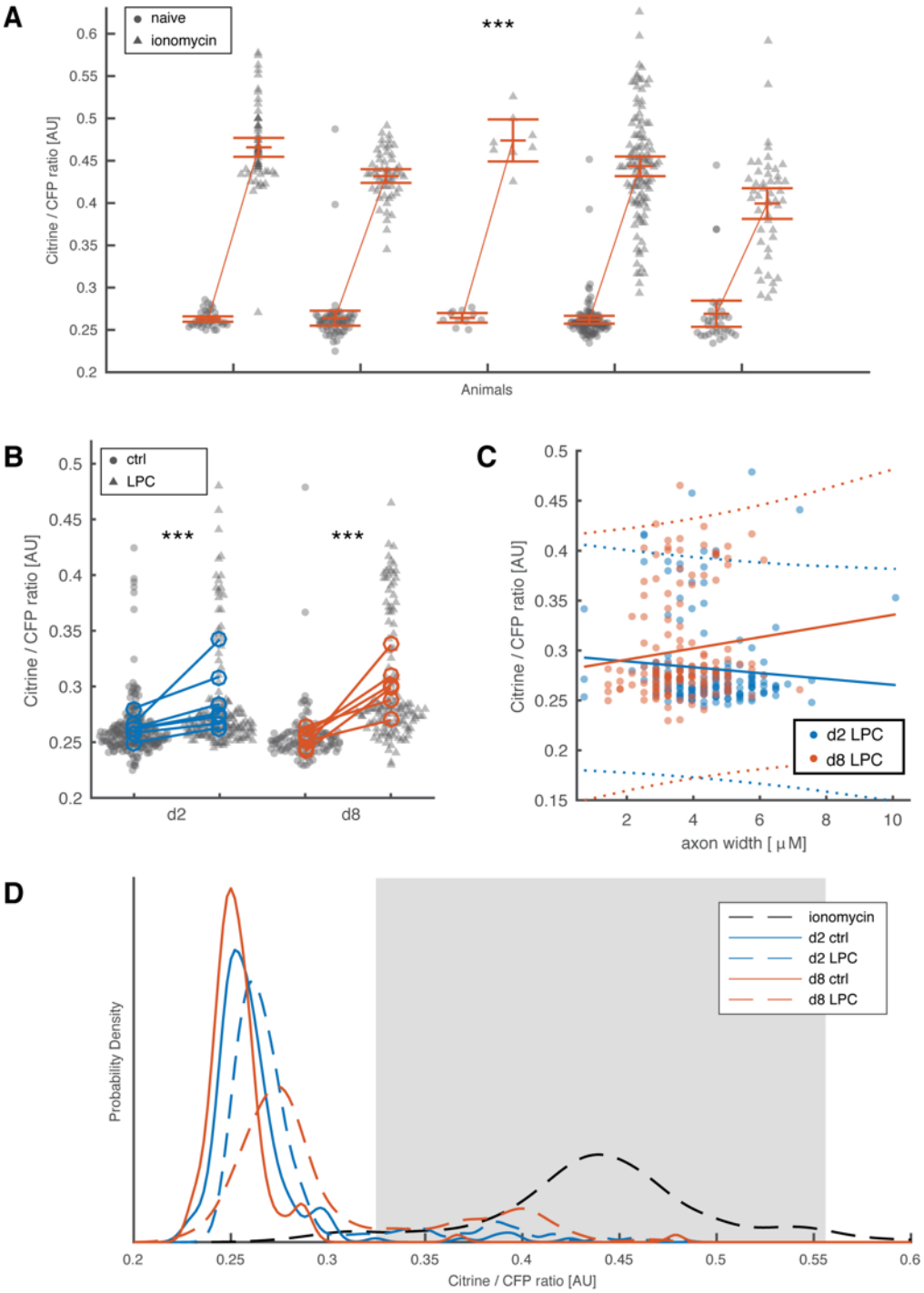

Figure 6.3: **Changes in Tn-XXL ratio following ionomycin treatment and demyelination**. **A**: Citrine/CFP ratio in five animals before and after ionomycin application. Markers indicate median pixel ratios for individual axons. Error bars indicate mean and 95% confidence interval. **B**: Significant change in fluorescence ratio due to demyelination. Markers indicate individual axons, connected circles show average ratios for the LPC and saline treated leg of the same animal. **C**: No correlation between axon width and fluorescence ratio. **D**: Kernel density plots of fluorescence ratio distributions. The grey rectangle indicated two standard deviations above and below the mean ratio for ionomycin treated axons. The difference between myelinated and demyelinated axons

remained significant even when all axons within this range were removed from the analysis.

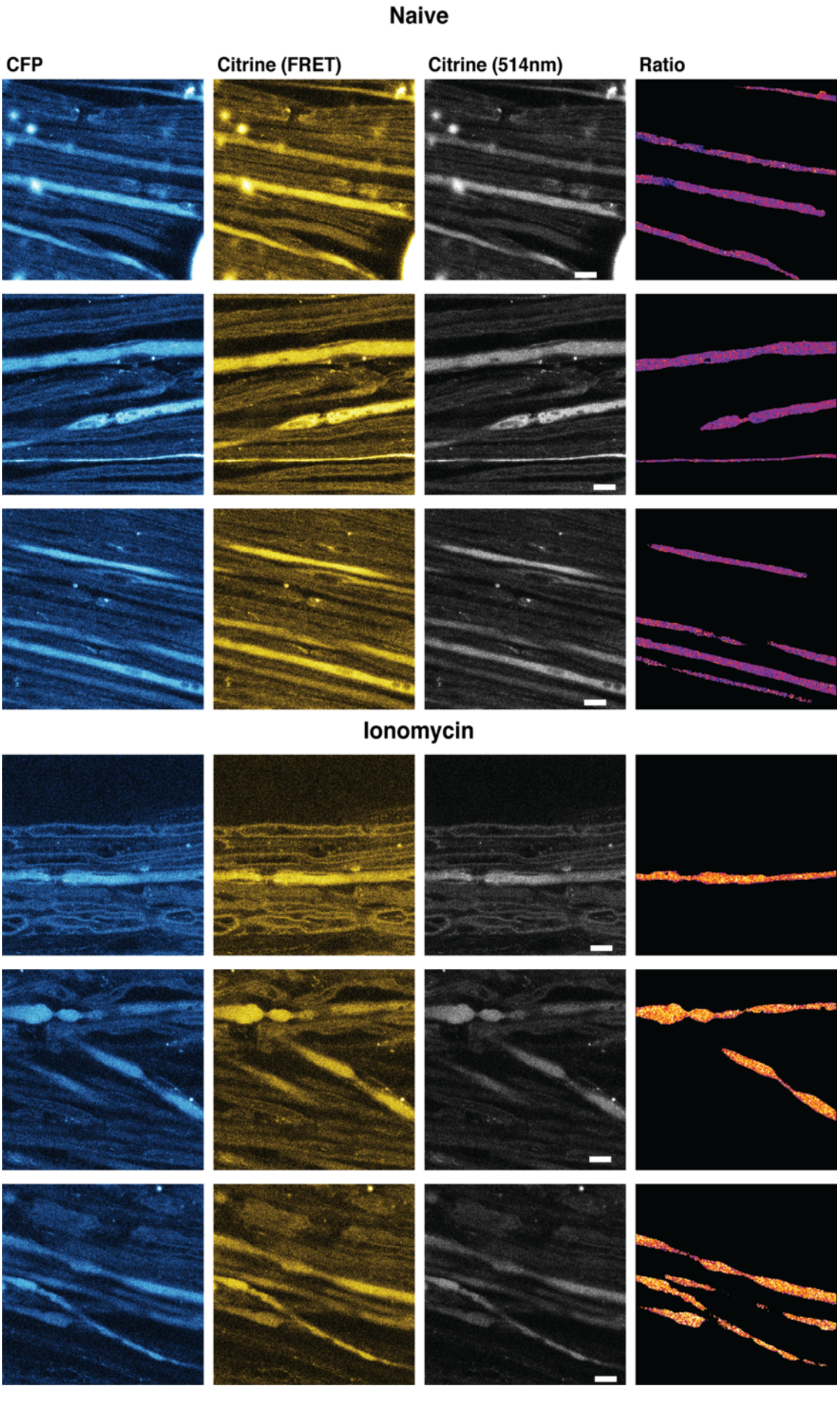
Naive
CFP
Citrine (FRET)
Citrine (514nm)
Ratio
Ionomycin

Figure 6.4: **Representative examples of Tn-XXL expressing axons before and after application of ionomycin**. The first three columns contain raw data. Images on the right show processed data with false colours indicating the Citrine / CFP ratio ("hotter" = higher). Scale bars indicate 10µm.

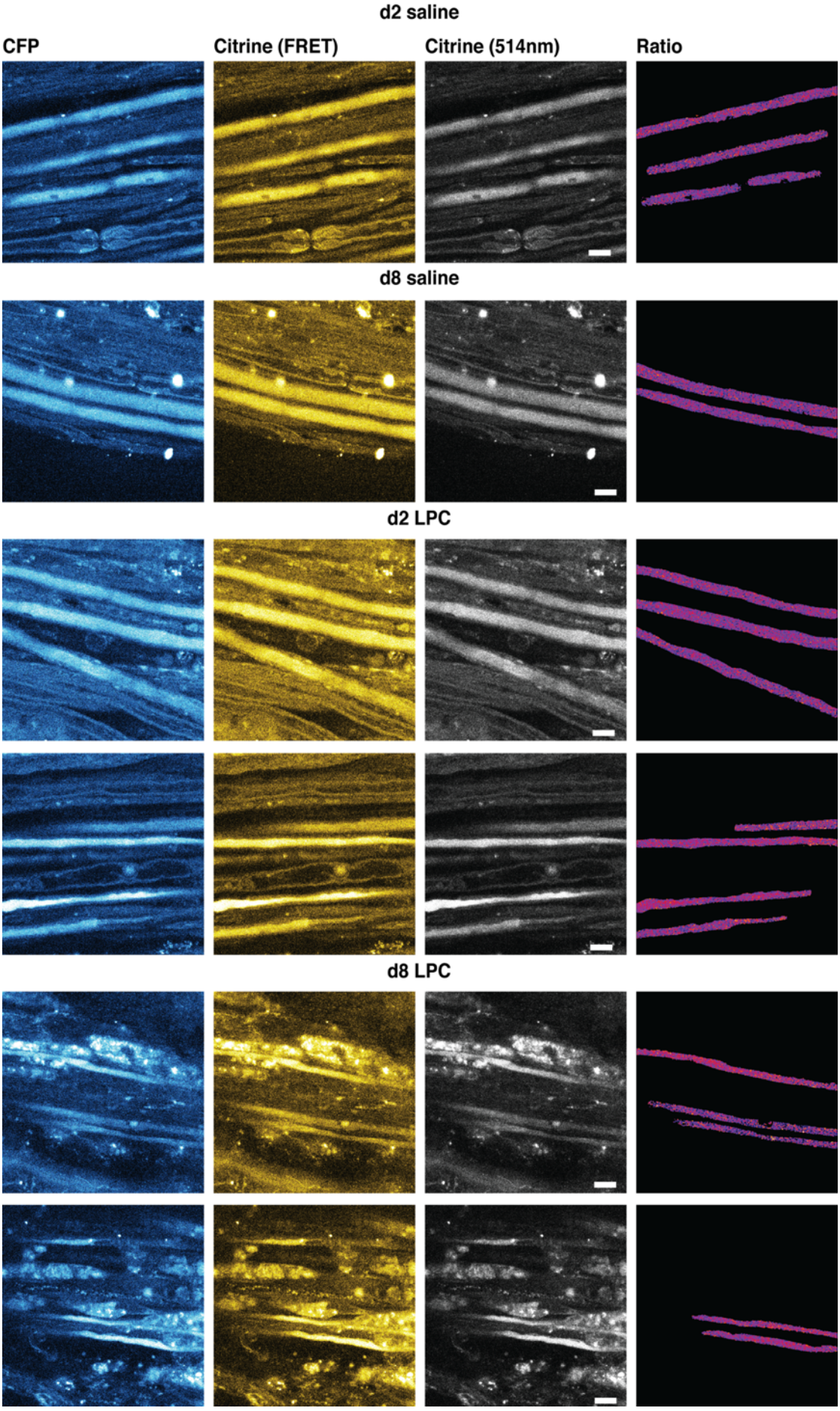
d2 saline
CFP
Citrine (FRET)
Citrine (514nm)
Ratio
d8 saline
d2 LPC
d8 LPC

Figure 6.5: **Representative examples of demyelinated and control treated Tn-XXL expressing axons**. The first three columns contain raw data. Images on the right show processed data with false colours indicating the Citrine / CFP ratio ("hotter" = higher). Note the difference in myelin debris on days 2 and 8. Scale bars indicate 10µm.

DISCUSSION

Originally planned as a more comprehensive series of experiments covering all time points investigated in chapter 4, the investigation of intra-axonal calcium was significantly hampered by the spotty expression of the indicator. More than one in three animals showed little to no expression of Tn-XXL. Thy1.2, the promotor under which the transgene is expressed, is known to cause mosaic expression in a varying number of cells (Caroni 1997; Feng et al. 2000), however, there was a significant difference from the much more reliable Thy1.2 controlled expression of CFP in Mito-S mice.

Regardless, it was possible to successfully image calcium in peripheral axons. The proportion of fluorescence ratios measured in untreated axons and axons flooded with extracellular calcium was found to be about 1.65x or 65%. This is significantly lower than the difference of 2.7x which the creators of Tn-XXL reported under optimal conditions (*in vitro*, cultured kidney fibroblasts) (Direnberger 2011) and also lower than the ratio of approximately 2 found by Siffrin and colleagues in the cerebellum *in vivo* (Siffrin et al. 2015)[8]. This difference in performance can potentially be explained by the fact that the 405nm laser (the most suitable wavelength available to us) is suboptimal for the excitation of Tn-XXL and may lead to a lower signal to background ratio compared with excitation with a wavelength of 430nm or 850nm in a two photon system as used by Siffrin et al. Nevertheless, significant increases in calcium signal were found in demyelinated axons both on day 2 and day 8 after treatment, even after potentially dead

[8] Somewhat peculiarly, both (Siffrin et al. 2015) and (Luchtman et al. 2016) calculate $\Delta R/R$ based on an intensity modulated ratio image. It is not addressed what implications this has for the interpretation of their results.

axons were removed from the analysis. No significant difference was found between the two days suggesting a consistently increased calcium level during the first week of demyelination.

In order to further interpret these changes, it would be desirable to translate the change in fluorescence to a change in intracellular calcium. However, such a conversion is difficult to achieve in practise. The median increase in fluorescence ratio due to demyelination (regardless of time point) was 7% absolute or 10% of the total range between a control axon and an axon flooded with extracellular Ca^{2+}. Calibration curves for Tn-XXL obtained in both drosophila and mice *in vivo* suggest that the relative change in fluorescence over baseline $\Delta R/R$ and the actual concentration of free calcium are approximately linearly related over the physiological range (Mank et al. 2008; Geiger et al. 2012). This suggests that the increase in calcium may be around 135nM or $1/10^{th}$ of the concentration difference between the intracellular and extracellular space (assuming 1.4mM extracellular Ca^{2+} and 50nM intracellular Ca^{2+}). While a rather rough estimate, this value is below the transient 250nM increase due to a single action potential reported in the dendrites of hippocampal pyramidal cells (Maravall et al. 2000).

A different approach is to compare the changes observed here to other publications using Tn-XXL. Birkenstock, Siffrin et al investigated the effects of glutamate excitotoxicity on axonal Ca^{2+} by applying 100mM of glutamate directly to cerebellar axons (Luchtman et al. 2016). They report a mean increase in fluorescence ratio of 21% at a max change of about 100% induced by ionomycin (Siffrin et al. 2015). Williams et al used Tn-XXL mice to investigate axonal Ca^{2+} in spinal cord injury (Williams et al. 2014). They classified axons as injured if they showed an increase in $\Delta R/R$ of $>50\%$ after spinal cord contusion and while the total range is not stated, data from dying axons suggest that the maximum increase may be around 200%. Finally, Mank et al used Tn-XXL to measure physiological stimuli in the mouse optical cortex and reported a peak increase of $7.4 \pm 5.6\%$ at a maximum increase of about 150% (Mank et al. 2008). While difficult to interpret due to differences in image acquisition and analysis, taken together these publications may suggest that the increase in calcium observed here may be in the high physiological range, below the ones observed in spinal cord injury or excitotoxicity but significantly above

baseline levels. This seems realistic considering that calcium is a strong cell death signal and axons would not be expected to survive long under conditions of very high calcium (Coleman 2005; Stirling & Stys 2010). On the other hand, the elevated calcium may be sufficient to explain some of the mitochondrial effects. The Ca^{2+} level necessary to anchor mitochondria near synapses, for example, is believed to be somewhere above 100µM and below 600µM (MacAskill et al. 2010). Similarly, the disruption of mitochondrial transport in a model of ALS has been explained by elevated levels of axonal Ca^{2+} (Mórotz et al. 2012).

No difference in intra-axonal calcium was observed between demyelinated axons on day 2 and day 8. While the mitochondrial transport deficit was observed at both time points, the increase in membrane potential was only seen on days 2 and 4. This could indicate that the increase in $\Delta\psi m$ is caused by something other than calcium. Alternatively, it is possible that even if the levels of Ca^{2+} in the axoplasm are similar, the ones inside the mitochondria might not be. There is no published data about whether the Tn-XXL sensor can enter mitochondria - the original publication just indicates that it does not seem to enter neuronal nuclei (Direnberger 2011). However, whereas a publication describing mitochondrial calcium in muscle fibres using the Ca^{2+} indicator *yellow cameleon 2* showed mitochondria which clearly stood out from the intracellular space (Rudolf et al. 2004) due to their increased fluorescence, no such pattern could be seen here even though the level of magnification used was the same as in the mitochondrial experiments. Hence it seems reasonable to assume that Tn-XXL based estimations of Ca^{2+} are dominated by intra-axonal but extra-mitochondrial calcium. The influence of calcium of mitochondrial respiration is mediated by receptors both inside and outside the mitochondrial matrix (Bhosale et al. 2015). If larger mitochondria are indeed better at buffering calcium (see Chapter 1) it is possible that the increase in mitochondrial size may counteract the increase in membrane potential.

Ultimately, it would be desirable to measure intracellular calcium at a point in time when mitochondrial transport is restored (e.g. day 20) – an experiment which I was not able to conduct due to time constraints. Nevertheless, the data presented above strongly

suggests that calcium is elevated during early demyelination, and therefore likely to contribute to the observed reduction in mitochondrial transport.

This leaves the question how exactly demyelination might cause the increase in intracellular calcium. As mentioned in the introduction, the accumulation of calcium channel subunits has been reported in demyelinated axons in EAE (Kornek et al. 2001). The subunits were fully integrated into the cell membrane and analysis of immunostained sections suggested that their number was greatest in early demyelination (day 11) and reduced to near-normal levels after remyelination. The authors also reported an increase in β-amyloid precursor protein in the affected axons which is a widely used marker of disturbed axonal transport. Similarly, the acid sensing Ca^{2+} channel ASIC1 was found to be upregulated in EAE 15 days after immunisation (Vergo et al. 2011). The caveat in both cases is that EAE is highly inflammatory which makes it difficult to conclude whether the inclusion of said channels is a consequence of demyelination or inflammation. Furthermore, it seems unlikely that the inclusion of ion channels into the cell membrane could occur quickly enough to explain the increased calcium levels observed on day 2.

The increase in intra-axonal calcium could also be secondary to an increase in intracellular sodium. Calcium is usually removed from the axon via the sodium-calcium exchanger. In situations of high intracellular Na^{+}, however, this ion transporter has been shown to operate in reverse, shuttling Ca^{2+} into the axon (Lehning et al. 1996). In myelinated axons, regions of sodium entry and the Na^{+}/Ca^{2+} exchanger are mostly separated with sodium channels located at the nodes and Na^{+}/Ca^{2+} exchangers at the internodes and the paranode. In demyelination, however, sodium channels redistribute along the axon, bringing Na^{+} channels and Na^{+}/Ca^{2+} exchangers closer together (Waxman et al. 2004). Close proximity of NaV1.6 channels and Na^{+}/Ca^{2+} exchangers in particular has been suggested to cause calcium entry into the axon, without requiring a reduction in ATP levels (Craner et al. 2004). Furthermore, redistribution of sodium channels was shown to occur in the first days after lysolecithin-mediated demyelination in the PNS (Novakovic et al. 1996). However, whilst this redistribution likely puts axons at risk of higher calcium entry upon return of conduction, it is less clear whether redistribution without conduction would be sufficient to disturb calcium homeostasis.

A third potential pathway for calcium entry into demyelinated axons are ion channels and signalling machinery which are normally protected underneath the myelin sheath. Zhang et al recently described L-type calcium channels underneath the myelin sheath of murine peripheral motor axons which are usually silent but can be exposed through acute LPC application or stretch-based myelin injury (Zhang & David 2016). Furthermore, a series of nano-complexes including receptors for glutamate and potentially other transmitters have been described in the internodal axon membrane of central and peripheral axons (Ouardouz et al. 2009; Stirling & Stys 2010; Christensen et al. 2016). In contrast to the ion channels mentioned above, these complexes do not cause calcium influx from outside the axon but rather provoke calcium release from internal calcium stores (notably the *axoplasmic reticulum*). Usually shielded by the myelin sheath, these complexes could get activated as they are exposed in demyelination, causing an almost immediate increase in intracellular calcium (see Stirling & Stys 2010 for a review).

In summary, even though the precise mechanism by which demyelination causes an increase in intracellular calcium is not known, several candidates have been identified. Overall, a moderate increase in intra-axonal calcium seems like the most likely explanation for the mitochondrial effects described in chapter 4.

CHAPTER 7: CONCLUSION

KEY FINDINGS

The aim of this thesis has been to understand more clearly the changes to mitochondrial function and dynamics caused by demyelination. In particular, I set out to add to the already substantial body of research by shining a light on mitochondrial dynamics and function at multiple time points during the development of the demyelinating lesion, covering different states of myelination, activity, and axonal energy demand.

The research presented here confirms many of the previously published findings such as the increase in mitochondrial size and density in demyelinated axons (Mutsaers & Carroll 1998; Hogan et al. 2009; Zambonin et al. 2011; Campbell & Mahad 2011), or the initial conduction block in demyelinated axons followed by a period of altered (and likely micro-saltatory) conduction (Smith & Hall 1980; Felts et al. 1997). I add to these findings by showing that mitochondrial transport is significantly reduced during early demyelination while mitochondrial membrane potential is increased. Furthermore, I show that these effects are unlikely to be explained by continuous conduction of action potentials, spatial constraints, or conduction block and instead may be a consequence of impaired mitochondrial Ca^{2+} homeostasis.

A central assumption which motivated this investigation is that mitochondrial transport is essential for a neuron's function and survival (e.g. Rugarli & Langer 2012). As mentioned in chapters 1 and 3, there is ample evidence for this, both from studies of models of neurological diseases and from knockout models in which mitochondrial transport is directly impaired. The findings presented here also support this idea: despite its high cost, bi-directional transport of dozens of mitochondria per minute was observed in virtually all naïve or sham-treated axons. I also found a slight difference in membrane potential between anterogradely and retrogradely moving mitochondria which is in line with the theory that mitochondrial transport helps to rejuvenate the mitochondrial pool by facilitating exchange of mitochondrial proteins and DNA (e.g. Miller & Sheetz 2004; Twig et al. 2008).

The reduction in mitochondrial transport observed here is thus an important, and currently unreported, consequence of demyelination. During the short period between lysolecithin-mediated demyelination and subsequent remyelination, this reduction did not appear to have any negative consequences for the axon: damaged axons were rare and their number did not increase with time. In fact, it seems likely that the accumulation of mitochondria helps protect the axon from the observed increase in Ca^{2+}, which is in line with a study by Ohno *et al.* showing that knock-out of the mitochondrial anchoring protein syntaphilin increases axonal loss in demyelination (Ohno et al. 2014). It is, however, interesting to speculate what the long-term consequences of this change might be. In diseases such as multiple sclerosis or Charcot-Marie-Tooth disease, demyelination is known to last for long periods of time and sometimes becomes chronic. Often, it is followed by axonal demise long after the initial demyelinating attack (reviewed in Trapp & Nave 2008). Similarly, mice treated with cuprizone, a copper chelator which causes slightly longer-lasting demyelination than lysolecithin, were found to recover initially and undergo successful remyelination but then experience a second phase of axonal loss (Manrique-Hoyos et al. 2012). In contrast to multiple sclerosis, which is a strongly inflammatory disease, the authors of the cuprizone study report only low levels of inflammation, suggesting that the observed degeneration is a direct consequence of demyelination. But the strongest evidence for detrimental consequences of mitochondrial accumulation caused by demyelination comes from a study by Joshi *et al.* (Joshi et al. 2015). Like Ohno and colleagues, Joshi *et al.* knocked out the calcium-controlled mitochondrial anchoring protein syntaphilin, likely ameliorating the impairment of mitochondrial transport observed here. However, instead of inducting strong but short-lived demyelination the authors tested the effects of syntaphilin knockout in chronically dysmyelinating *Shiverer* mice. In this model, preventing the accumulation of mitochondria prolonged the animal's lifespans. While they did not investigate mitochondrial movement directly, the authors speculated that demyelination might reduce mitochondrial exchange and renewal which, in the long run, causes the demise of axons. Recently, a similar detrimental effect of syntaphilin was also shown in axotomy

in vitro, and increasing anterograde transport through enhanced expression of Miro-1 was demonstrated to facilitate regeneration (Zhou et al. 2016).

In summary, there is reason to believe that the reduction of mitochondrial transport caused by demyelination is detrimental to the axon's health in the long term. This could be the case because limited transport leads to limited exchange of mitochondrial proteins and DNA which in turn permits the spread of mitochondrial dysfunction. Alternatively, the axon might simply run out of mitochondria. As discussed above, mitophagy likely occurs locally in the axon. This means that in order to keep their total number stable, new mitochondria have to be supplied from the soma at a constant rate. If the supply of new mitochondria is restricted by demyelination, the axon could become depleted of mitochondria downstream of the demyelinating lesion. Such depletion has been demonstrated in a chronic form of EAE after three weeks of impaired mitochondrial transport (Sorbara et al. 2014, supplementary materials). It also may be increased by axonal activity. Axons in sensory nerves such as the saphenous nerve investigated here are innervated at the distal end so that the distal part of the axon might still be active, even if axonal conduction is blocked more proximally. Work from our lab suggests that in response to high workload, saphenous nerve axons upregulate mitochondrial supply to their terminals (Sajic et al. 2013) – a physiological response which may fail if mitochondrial transport is disrupted by demyelination.

Any detrimental effects of demyelination on mitochondria may be further amplified by the increase in mitochondrial membrane potential observed here. Both the production of ATP and superoxide increase with mitochondrial membrane potential and in their resting state are balanced such that mitochondria only reach a small fraction of their maximal ROS production (Nicholls & Ferguson 2013, chapter 9). However, the rate of superoxide production increases significantly if mitochondria sit idle (Murphy 2009). Since mitochondria were found to exhibit increased membrane potentials at an early time point during demyelination at which conduction was almost certainly blocked, it seems possible that they were also producing superoxide at a higher than usual rate, damaging mitochondrial proteins and DNA in the process.

The second half of this thesis has been dedicated to investigating a number of potential mechanisms through which demyelination might lead to the observed decrease in mitochondrial transport and increase in membrane potential. The accumulation of mitochondria in demyelinated axons is often explained through a putative increase in energy demand caused by a continuous form of conduction (e.g. Campbell et al. 2012). However, at least in the particular model studied here the time course of events does not agree with this theory as both the decrease in mitochondrial transport and the peak of mitochondrial density preceded the likely return of conduction. Similarly, conduction block itself had no discernible effect on mitochondrial function and whilst it has been suggested that spatial constraints can limit mitochondrial trafficking, data from both naïve animals and early demyelination suggest that spatial constraints do not play a significant role here.

Instead, I found axonal calcium to be elevated during the first week of demyelination. Importantly, the observed increase was significant but not so extreme as to be catastrophic. As laid out in chapters 1 and 6, calcium is a powerful regulator of mitochondrial dynamics and in some conditions can also cause increases in mitochondrial membrane potential. It also directly controls the activity of the anchoring protein syntaphilin, tying the study at hand to the work by Ohno and Joshi (Ohno et al. 2014; Joshi et al. 2015). The mechanism by which demyelination might lead to an increase in intra-cellular calcium is not clear, but several promising candidates have been identified, including the addition and redistribution of ion channels and the exposure of signalling complexes previously protected under the myelin sheath (see discussion of chapter 6).

Overall, the findings presented here suggest a new interpretation of the well-known accumulation of mitochondria in demyelinated axons. They suggest that rather than respond to increased energy demand due to continuous conduction of action potentials along the membrane of the demyelinated axon, mitochondria may react to an early and pathological increase in intracellular calcium. Note that this is fully compatible with the idea that mitochondrial accumulation and hyperfusion protect the axon, at least in the short term. However, it suggests that this initial protection comes at a price, namely, decreased availability of mitochondria and impaired mitochondrial maintenance. It seems

feasible that this mechanism contributes to the axonal degeneration following long-term demyelination in diseases such as Charcot-Marie-Tooth disease and multiple sclerosis, even in the absence of inflammation. Importantly, however, if mitochondrial accumulation is caused by a change in axonal calcium rather than axonal energy demand, this also may open up new treatment opportunities: if the source of calcium entry into the axon can be identified, it may be possible to block it pharmacologically, thereby eliminating most of the need for increasing mitochondrial density in the affected parts of the axon.

LIMITATIONS AND FUTURE DIRECTIONS

Like any scientific endeavour, the work presented here leaves many questions unanswered. Perhaps the most glaring omission is the lack of a control experiment using a different way to induce demyelination. Whilst it seems unlikely to me that effects on intra-axonal calcium and mitochondrial dynamics which last for more than a week should be artefacts of lysolecithin treatment rather than consequences of demyelination, I feel that replicating these changes in a different model would significantly strengthen my conclusions. I unsuccessfully attempted to use ethidium bromide as demyelinating toxin (see Appendix C), but because of its effect on mitochondrial DNA the interpretation of this approach would have been difficult even if the experiment had been successful. An interesting alternative would be to apply the tools developed here to one of the many available animal models of Charcot-Marie-Tooth disease (Fledrich et al. 2012).

Secondly, it cannot be ruled out that axons experience a transitory increase in energy demand early in demyelination, for example due to repair processes or increased difficulty to keep up their membrane potential. Over the last years, new tools have been developed which allow measurement of the ATP/ADP ratio in intact cells, either indirectly via magnesium (Leyssens et al. 1996) or directly using novel FRET based sensors (Imamura et al. 2009). These tools could be very useful for understanding the relationship between demyelination, energy demand, and mitochondrial dynamics.

Furthermore, time restrictions and limited transgene expression meant that some interesting experiments around intra-axonal calcium were left undone. For example, I would have liked to obtain calcium measurements from axons after successful remyelination to see if the return to normal mitochondrial transport coincides with a return to baseline levels of Ca^{2+}. Furthermore, if calcium is indeed responsible for the changes in mitochondrial function and dynamics, applying a membrane-permeable calcium chelator such as EGTA to the lesion should reverse them (Ohno et al. 2011). I believe that this experiment would be particularly useful to address the caveats of measuring TMRM given the varying thickness of myelin surrounding the axons of interest (see discussion of chapter 4).

As discussed in chapter 6, it is not clear how calcium enters the axon after demyelination. Measuring axonal calcium during the application of lysolecithin might provide a first clue as it would allow to distinguish between calcium entry mechanisms which are immediate (e.g. the exposure of channels and receptors usually protected by the myelin sheats, see Zhang & David 2016) and mechanisms which take more time such as the integration of calcium channels into the axon membrane or the redistribution of sodium channels.

Finally, I believe that some of the most interesting questions raised by this piece of work concern not demyelination but rather the mitochondrial life cycle in healthy neurons. As discussed in chapter 3, I found very little evidence of mitochondrial fission and fusion in the adult mouse *in vivo*. Given the length of the saphenous nerve, a low rate of exchange between mitochondria might be necessary to ensure that "fresh" material reaches the axon terminals at all. However, given that much of our theory of mitochondrial maintenance is based on the assumption that the mitochondrial pool is frequently replenished through fission and fusion (e.g. Mouli et al. 2009; Liesa & Shirihai 2013) and since it is becoming apparent both here and elsewhere that *in vitro* experiments overestimate both mitochondrial transport and fission / fusion (e.g. Takihara et al. 2015) it seems vital to better understand mitochondrial interactions in neurons. One fruitful experiment might be to label the mitochondrial population at one point of the nerve (e.g. with a permanent MitoTracker dye or via light activate-able gene constructs) and observe the interaction

of moving anterogradely and retrogradely moving mitochondria with stationary mitochondria on either side of the treatment site.

APPENDIX

APPENDIX A: PERFORMING STATISTICAL TESTS ON NESTED DATA

This thesis is concerned with biological entities at fundamentally different levels. On the lowest level, properties of individual mitochondria such as size or membrane potential are measured. On the next level above this, properties of individual axons such as mitochondria transported per unit time or mitochondrial density are measured. Finally, every axon belongs to an animal and multiple axons (and their mitochondria) therefore share the same confounding factors such as variations in treatment, quality of surgery, depth of anaesthesia or body temperature of the animal. This raises the question how to perform statistical analysis on the results of experiments properly.

Historically, two major approaches have been used to tackle similar problems. Perhaps most common is the so called naïve (Snijders & Bosker 2011) or pooled (Kreft & de Leeuw 1998) approach in which each cell or axon is treated as an independent observation, irrespective of which animal / cell culture it stems from. Perhaps because of its simplicity, the naive approach is common in the mitochondrial literature (Nikić et al. 2011; Sajic et al. 2013; Sorbara et al. 2014; Ohno et al. 2014). Underlying it is the assumption that the macro level (e.g. the animal) has no significant effect on the micro level (the axon). This assumption, while rarely tested explicitly, is critical since even small intra-class correlations can lead to drastic underestimation of Type 1 errors (Dorman 2008).

Alternatively, data are sometimes aggregated to a single value per macro unit (e.g. mean transport per animal). Whilst certainly more conservative, this kind of analysis also leads to a shift of meaning the micro level (axons) to the macro level (the animal). This shift can have important consequences when trying to make observations about the micro level as demonstrated by the so called Robinson Effect or Ecological Fallacy (Robinson 1950).

Robinson showed that a correlation between two factors on the macro level can be very different from the equivalent correlation on the micro level. As an example of this, consider the hypothetical case of measuring axonal mitochondrial transport in two mice of very different age. Suppose that the axons in the younger mouse show significantly more transport compared with the older animal (Milde et al. 2015), and that the axon diameter in the older mouse is larger than in the younger animal. It is possible to construct a scenario in which the correlation between axon diameter and transport is reversed depending on the level of observation. Because of cases like these it is generally accepted that aggregation should not be used to make conclusions about micro level effects (Kreft & de Leeuw 1998 for further discussion; see also Snijders & Bosker 2011).

A third option is to choose a multilevel approach which considers differences on both the micro and the macro level. Such analyses are increasingly common in the social sciences (Field et al. 2012) and in clinical studies (Twisk 2006) and generally fall in one of two categories: random effects ANOVAs (Sahai & Ageel 2012; Krzywinski et al. 2014) and hierarchical linear models (HLM) (Kreft & de Leeuw 1998; Twisk 2006; Snijders & Bosker 2011). Both approaches have in common that they take the variation on the macro level (e.g. between animals with the same treatment) into account when comparing micro level instances. In many cases, random effects ANOVAs and HLMs can be applied to the same problems (Logan 2010)[9]. However, the use of random effects ANOVA usually requires balanced group designs, whereas HLM do not, making the latter a more versatile tool.

Hierarchical linear models can be seen as an extension of general multiple regression models in that they contain multiple error terms (and optionally varying slopes) for different levels of the model. In its simplest form, the *random intercept model*, the general equation for linear models

$$Y_i = \beta_0 + \beta_1 X_{1,i} + \varepsilon_i$$

becomes

[9] In fact, using hierarchical linear models with residual maximum likelihood (REML) methods for equal group sizes is equivalent to using ANOVA estimators (Snijders & Bosker 2011, chapter 3.2.1).

$$Y_{ij} = (\beta_0 + \mu_{0j}) + \beta_1 X_{ij} + \varepsilon_{ij}$$

with j indicating the level over which the intercept varies. This way, the model can capture the offsets which apply to the axons of a particular animal, for example due variations in anaesthesia, as well as the effect of a treatment which applies to axons across multiple animals. The parameters β and μ of an HLM are determined using either maximum likelihood (ML) or restricted maximum likelihood (REML) estimation. There appears to be no consensus about which method is superior. Snijders and Bosker recommend the use of REML when dealing with <50 groups (Snijders & Bosker 2011, chapters 4.7 and 6.1) while Twisk suggests that ML may be a superior tool for estimating fixed effects (Twisk 2006). Both, however, agree that in practise the differences between the two tend to be small.

What makes HLM particularly powerful is that in estimating the parameters of the model, the information of a single group is combined with the information of all other groups; a process which is sometimes described as "borrowing strength". For example, in order to untangle how much of the difference between treated and untreated axons on day 8 post treatment is due to the treatment and how much is due to differences in animal baseline, HLM can borrow strength by using the variance between animals at other time points to assign an individual intercept to every animal and thereafter arrive at an estimate of the treatment effect. Multilevel models thus present a good way to deal with nested, partially dependent observations (Field et al. 2012).

In order to find out whether the multilevel linear modelling approach is applicable in this study, I followed the approach laid out in (Field et al. 2012) and constructed both a naïve linear model using the generalized least squares method (`gls`) in R and a hierarchical linear model with a random intercept dependent on the animal using `nlme`. I then compared the fit of both models using the Akaike Information Criterion (AIC) and -2log-likelihood. HLM proved the superior approach to modelling most effects studied in this thesis and hence is used to determine significance throughout this study. Maximum likelihood estimation is used to estimate the model parameters since it offers the option to compare the fit of the HLM to that of a naive model (Field et al. 2012) and since it

was used in most of the text books available to me. I believe that this is a more honest approach to significance testing which avoids the inflation of Type 1 error rates that occurs when dependent observations are assumed to be independent (Dorman 2008). Unfortunately, multiple experiments in this study (particularly those described in chapters 2, 3 and 4) were originally designed with the naïve approach in mind and thus assuming a larger statistical power than I would attribute to them now. While many of the observed effects are still statistically significant, I would prefer to have conducted the experiments described in these chapters using a larger number of animals.

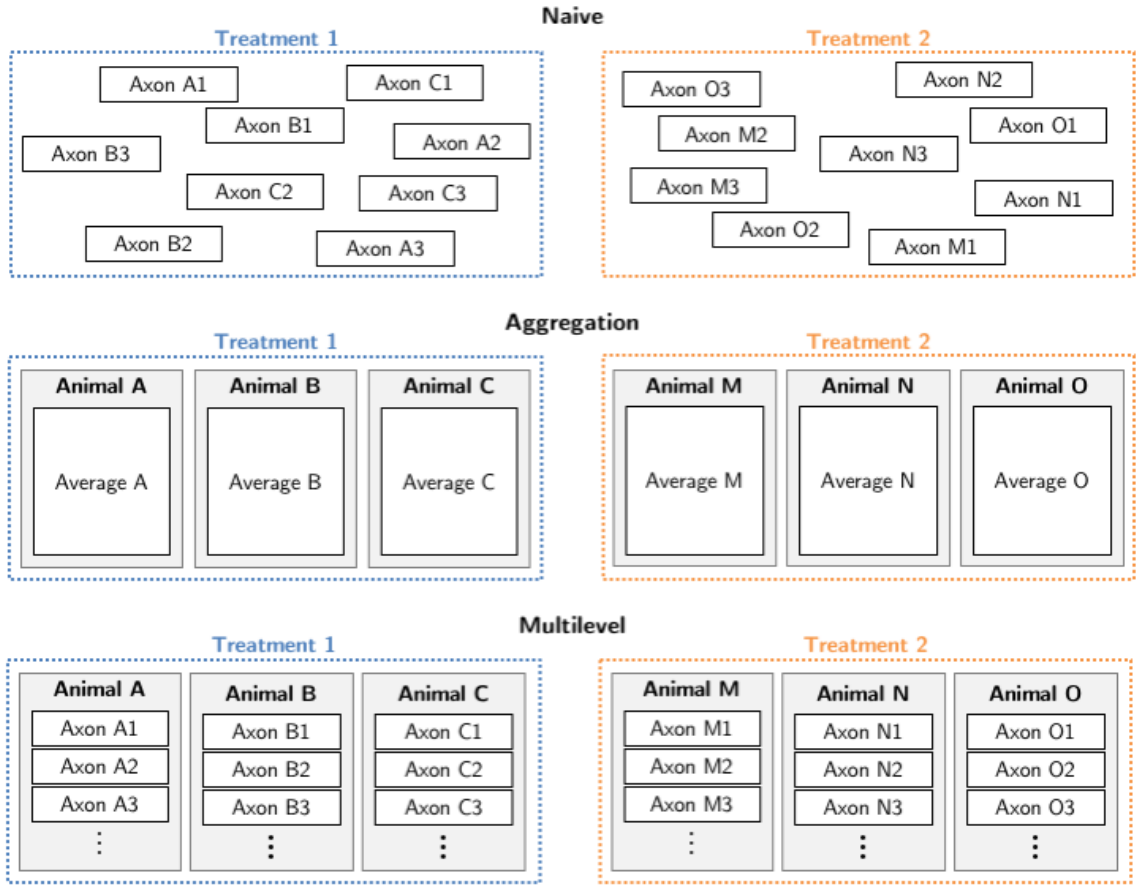

Figure A.1: **Three ways of analysing nested results**. See text for details

APPENDIX B: OVERVIEW OF EXCITATION AND DETECTION SETTINGS

Microscope	Dye	Excitation	Detection
LSM Pascal 5.0	TMRM	543nm	$>$ 585nm
	CFP	458nm	475nm - 525nm
	Fluoromyelin Green	488nm	505nm - 550nm
LSM 710	TMRM	561nm	565nm - 730nm
	CFP	458nm	465nm - 550nm
	Myelin reflection	488nm, 561nm, 633nm	485nm - 491nm, 558nm - 564nm, 630nm - 636nm
	TnXXL (ratiometric)	405nm	460nm - 510nm, 520nm - 570nm
	TnXXL (citrine)	514nm	515nm - 650nm

APPENDIX C: ETHIDIUM BROMIDE CONTROLS

All mitochondrial and axonal changes described in chapters 2, 4, and 6 followed the application of lysolecithin (LPC). There are reasons to believe that they were caused by demyelination rather than direct action of LPC such as the long duration of the effects (days) compared to the estimated time it takes for LPC to be broken down *in vivo* (minutes), or studies showing that LPC applied to unmyelinated axons *in vitro* does not affect mitochondrial dynamics (see introduction and discussion of chapter 2 and discussion of chapter 4). Nevertheless, it would be desirable to confirm these findings using other means of demyelination. As mentioned in chapter 2, ethidium bromide (EB) is another demyelinating toxin with a well-understood time-course and physiology (Black et al. 1991; Felts & Smith 1996; Felts et al. 1997). The major drawback of EB is that it drastically reduces the amount of mitochondrial DNA through DNA chelation (Leibowitz 1971; Desjardins et al. 1985; Hayashi et al. 1990) which makes it less suitable for the study of mitochondria. On the other hand, axons in EB lesions in rats have been reported to survive at even higher rates than axons in LPC lesions (Woodruff & Franklin 1999), suggesting that the loss of mtDNA is not catastrophic. Thus I decided to repeat some of the experiments presented earlier with EB as the demyelinating agent. I argued that while EB would likely have a direct effect on mitochondrial function, replicating the increase in intracellular calcium or the decrease in mitochondrial transport in EB treated, demyelinated axons would nevertheless provide evidence that these effects were direct consequences of demyelination.

In order to induce demyelination using EB a similar procedure as described in chapter2 was used. However, instead of applying the compound directly, a sterile piece of flexible tubing was lowered onto the nerve and held in place using light pressure. The inside of the tube was filled with EB solution while sterile saline was applied outside. This way, the exposure of surrounding tissue and particularly the skin to EB was minimized. In total, 19 male Mito-S mice were treated with different doses of EB (ranging from 0.05% to 1% in sterile saline) over either 20 or 45 minutes. In addition, the perineureum of the saphenous nerve of three animals was pierced with a fine tungsten needle to facilitate the

uptake of EB into the nerve. Since EB takes longer to induce demyelination than LPC (Felts et al. 1997; Woodruff & Franklin 1999), animals were imaged between 3 and 13 days after application.

Ethidium bromide is a yellow fluorescent molecule which made it possible to confirm that the compound was successfully taken up into the nerve and into cell nuclei in particular (see Figure C.1 A). However, even though all 19 animals showed signs of EB having entered through the perineureum, the resulting demyelination was, in my hands at least, unpredictable (see Table C.1). The nerves of some animals showed little or no signs of demyelination even at high doses while in others virtually all visible axons appeared dead and filled with fragmented and depolarised mitochondria (see Figure C.1). Additionally, the saphenous nerve and the tissues surrounding it showed signs of severe inflammation including clusters of mobile macrophages. While this observation disagrees with earlier reports based on rats, there is at least one report of severe and chronic inflammation cause by EB injection into the spinal cord of mice (Kuypers et al. 2013).

Even though mitochondria in some demyelinated axons increased in density and showed signs of hyperfusion similar to those observed after LPC treatment, I ultimately decided to abort this series of experiments. It seems that topical application of EB, while it causes some of the toxin to enter the nerve, is not suitable for consistent induction of demyelination.

As discussed in chapter 2, other means of causing demyelination such as the targeted expression of diphtheria toxin receptors in myelinating cells followed by the injection of small doses of the toxin (Buch et al. 2005; Locatelli et al. 2012) could be used to instead of ethidium bromide and would likely be more suitable for the control experiment attempted here.

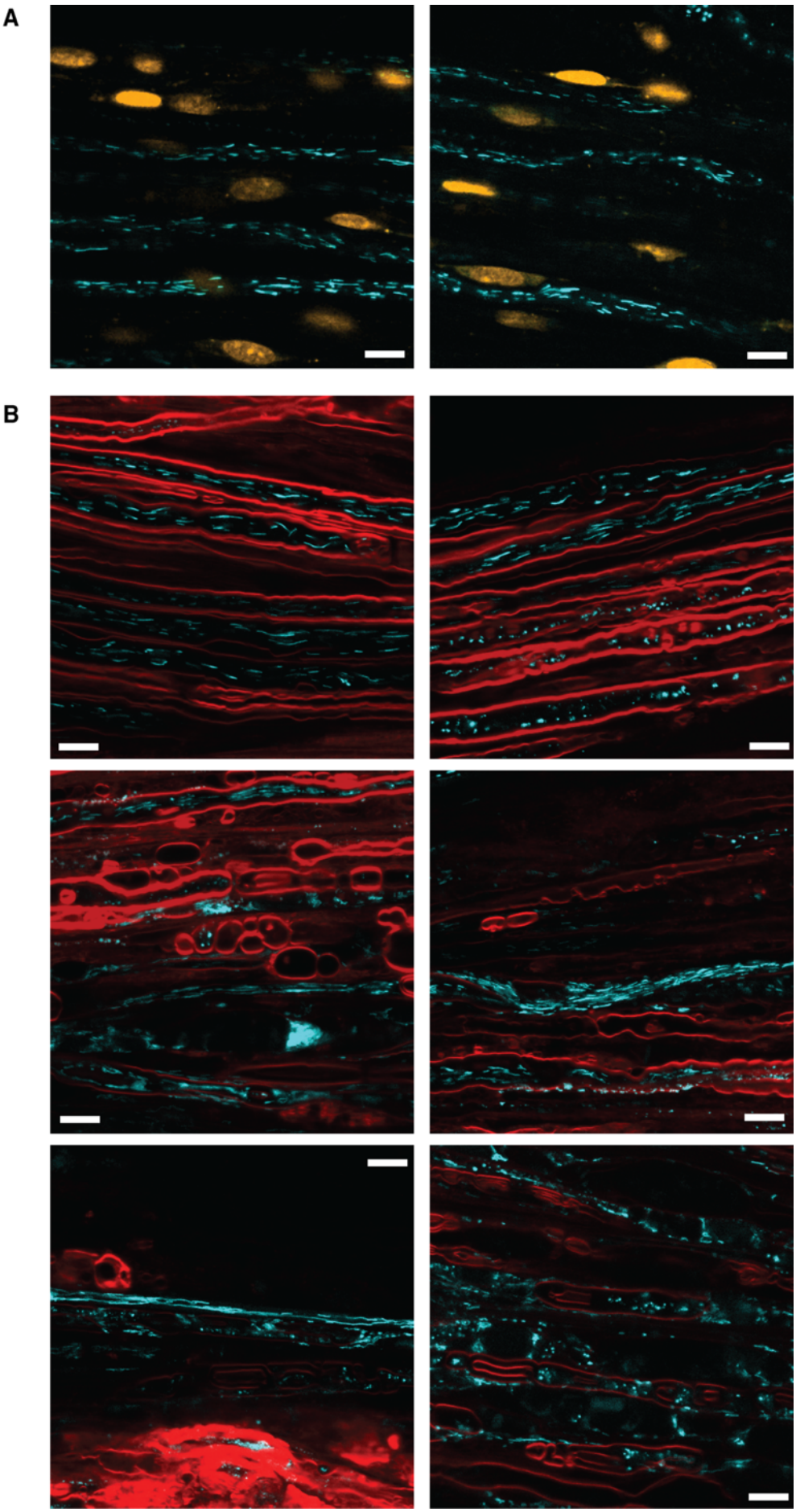
A
B

Figure C.1: **Saphenous nerves from different mice after the application of ethidium bromide**. **A**: After topical application, EB fluorescence can be seen in cell nuclei in the saphenous nerve. **B**: Consequences of EB application ranged from no obvious signs of demyelination and fragmented mitochondria in axons with only slightly disturbed myelin through demyelinated axons with increased mitochondrial content and hyperfusion to destruction of all visible axons. Genetically encoded, mitochondrially-targeted CFP in blue; Fluoromyelin Red in red; scale bars indicate 10μm.

animal	dose [%]	application time	perineureum punctures	day of imaging	outcome
1	0.05	20	no	3	no signs of demyelination
2	0.02	20	no	3	no signs of demyelination
3	0.02	20	no	7	no signs of demyelination
4	0.05	20	no	7	no signs of demyelination
5	0.05	20	yes	7	little demyelination, a lot of axonal damage
6	0.02	20	yes	7	some demyelination, a lot of axon damage
7	0.1	20	no	7	no signs of demyelination
8	0.1	45	no	7	little demyelination
9	1	20	no	7	deformed myelin, no full demyelination, axon damage
10	0.1	20	yes	7	little demyelination, a lot of axon damage
11	1	45	no	7	unacceptable inflammation - animal culled
12	1	45	no	13	widespread demyelination and destruction of axons
13	0.1	45	no	13	little demyelination
14	0.2	20	no	13	no signs of demyelination
15	0.5	20	no	13	virtually complete demyelination
16	0.4	20	no	13	virtually no demyelination
17	0.3	20	no	13	no signs of demyelination
18	0.5	20	no	10	widespread axon damage
19	0.5	20	no	10	some myelin disruption, little demyelination, a lot of axonal damage

Table C.1: **Different doses and application times of ethidium bromide and their effects on myelin and axons.**

BIBLIOGRAPHY

Abramov, A.Y. & Duchen, M.R., 2008. Mechanisms underlying the loss of mitochondrial membrane potential in glutamate excitotoxicity. *Biochimica et Biophysica Acta - Bioenergetics*, 1777(7–8), pp.953–964.

Agronskaia, a V, Tertoolen, L. & Gerritsen, H.C., 2004. Fast fluorescence lifetime imaging of calcium in living cells. *Journal of biomedical optics*, 9(6), pp.1230–7.

Alberts, B. et al., 2008. *Molecular biology of the cell, 5th edition*,

Alberts, B., 2008. *Molecular Biology of the Cell: Reference Edition, Volume 1*, Garland Science.

Ames, a, 2000. CNS energy metabolism as related to function. *Brain research. Brain research reviews*, 34(1–2), pp.42–68.

Amiri, M. & Hollenbeck, P.J., 2008. Mitochondrial biogenesis in the axons of vertebrate peripheral neurons. *Developmental neurobiology*, 68(11), pp.1348–61.

Andrews, S., Gilley, J. & Coleman, M.P., 2010. Difference Tracker: ImageJ plugins for fully automated analysis of multiple axonal transport parameters. *Journal of neuroscience methods*, 193(2), pp.281–7.

Arbuthnott, E.R., Boyd, I. a & Kalu, K.U., 1980. Ultrastructural dimensions of myelinated peripheral nerve fibres in the cat and their relation to conduction velocity. *The Journal of physiology*, 308(1980), pp.125–57.

Arganda-Carreras, I. et al., 2006. Consistent and Elastic Registration of Histological Sections using Vector-Spline Regularization. *Cancer Imaging*, 4241(6024), pp.85–95.

Arnold, B. et al., 2011. Integrating multiple aspects of mitochondrial dynamics in neurons: age-related differences and dynamic changes in a chronic rotenone model. *Neurobiology of disease*, 41(1), pp.189–200.

Ashrafi, G. et al., 2014. Mitophagy of damaged mitochondria occurs locally in distal

neuronal axons and requires PINK1 and Parkin. *The Journal of cell biology*, 206(5), pp.655–70.

Attwell, D. & Laughlin, S.B., 2001. An energy budget for signaling in the grey matter of the brain. *Journal of cerebral blood flow and metabolism : official journal of the International Society of Cerebral Blood Flow and Metabolism*, 21(10), pp.1133–45.

Baas, P.W., Black, M.M. & Banker, G.A., 1989. Changes in microtubule polarity orientation during the development of hippocampal neurons in culture. *The Journal of cell biology*, 109(6 Pt 1), pp.3085–94.

Baines, C.P. et al., 2005. Loss of cyclophilin D reveals a critical role for mitochondrial permeability transition in cell death. *Nature*, 434(7033), pp.658–62.

Balaratnasingam, C. et al., 2010. Time-dependent effects of focal retinal ischemia on axonal cytoskeleton proteins. *Investigative ophthalmology & visual science*, 51(6), pp.3019–28.

Baloh, R.H. et al., 2007. Altered axonal mitochondrial transport in the pathogenesis of Charcot-Marie-Tooth disease from mitofusin 2 mutations. *The Journal of neuroscience : the official journal of the Society for Neuroscience*, 27(2), pp.422–30.

Barreto-Chang, O.L. & Dolmetsch, R.E., 2009. Calcium imaging of cortical neurons using Fura-2 AM. *Journal of visualized experiments : JoVE*, (23).

Barron, M.J. et al., 2004. The distributions of mitochondria and sodium channels reflect the specific energy requirements and conduction properties of the human optic nerve head. *The British journal of ophthalmology*, 88(2), pp.286–90.

Barsukova, A. et al., 2011. Activation of the mitochondrial permeability transition pore modulates Ca2+ responses to physiological stimuli in adult neurons. *The European journal of neuroscience*, 33(5), pp.831–42.

Bassa, B. V et al., 1999. Lysophosphatidylcholine activates mesangial cell PKC and MAP kinase by PLCgamma-1 and tyrosine kinase-Ras pathways. *The American journal of physiology*, 277(3 Pt 2), pp.F328-37.

Baughman, J.M. et al., 2011. Integrative genomics identifies MCU as an essential component of the mitochondrial calcium uniporter. *Nature*, 476(7360), pp.341–345.

Bedard, K. & Krause, K., 2007. The NOX family of ROS-generating NADPH oxidases: physiology and pathophysiology. *Physiological reviews*, 87(1), pp.245–313.

Beltran-Parrazal, L. et al., 2006. Mitochondrial transport in processes of cortical neurons is independent of intracellular calcium. *American journal of physiology. Cell physiology*, 291(6), pp.C1193-7.

Berg, J., Hung, Y.P. & Yellen, G., 2009. A genetically encoded fluorescent reporter of ATP:ADP ratio. *Nature methods*, 6(2), pp.161–6.

Bhosale, G. et al., 2015. Calcium signaling as a mediator of cell energy demand and a trigger to cell death. *Annals of the New York Academy of Sciences*, 1350(1), pp.107–116.

Bieber, A.J. et al., 2002. Human antibodies accelerate the rate of remyelination following lysolecithin-induced demyelination in mice. *Glia*, 37(3), pp.241–9.

Billups, B. & Forsythe, I.D., 2002. Presynaptic mitochondrial calcium sequestration influences transmission at mammalian central synapses. *The Journal of neuroscience : the official journal of the Society for Neuroscience*, 22(14), pp.5840–7.

Bilsland, L.G. et al., 2010. Deficits in axonal transport precede ALS symptoms in vivo. *Proceedings of the National Academy of Sciences of the United States of America*, 107(47), pp.20523–8.

Birgbauer, E., Rao, T.S. & Webb, M., 2004. Lysolecithin induces demyelination in vitro in a cerebellar slice culture system. *Journal of neuroscience research*, 78(2), pp.157–66.

Black, J.A. et al., 1991. Distribution of sodium channels in chronically demyelinated spinal cord axons: immuno-ultrastructural localization and electrophysiological observations. *Brain research*, 544(1), pp.59–70.

Black, J. a, Waxman, S.G. & Smith, K.J., 2006. Remyelination of dorsal column axons by endogenous Schwann cells restores the normal pattern of Nav1.6 and Kv1.2 at nodes of Ranvier. *Brain : a journal of neurology*, 129(Pt 5), pp.1319–29.

Blackman, S.S.S., 2004. Multiple hypothesis tracking for multiple target tracking. *Aerospace and Electronic Systems Magazine, IEEE*, 19(1), pp.5–18.

Blakemore, W.F., 1982. Ethidium bromide induced demyelination in the spinal cord of the cat. *Neuropathology and applied neurobiology*, 8(5), pp.365–75.

Blakemore, W.F., 1973. Remyelination of the superior cerebellar peduncle in the mouse following demyelination induced by feeding cuprizone. *Journal of the neurological sciences*, 20(1), pp.73–83.

van der Bliek, A.M., Shen, Q. & Kawajiri, S., 2013. Mechanisms of mitochondrial fission and fusion. *Cold Spring Harbor perspectives in biology*, 5(6).

Bolaños, J.P., Almeida, A. & Moncada, S., 2010. Glycolysis: a bioenergetic or a survival pathway? *Trends in biochemical sciences*, 35(3), pp.145–9.

Bostock, H. & Sears, T. a, 1978. The internodal axon membrane: electrical excitability and continuous conduction in segmental demyelination. *The Journal of physiology*, 280, pp.273–301.

Bouhy, D. & Timmerman, V., 2013. Animal models and therapeutic prospects for Charcot-Marie-Tooth disease. *Annals of neurology*, 74(3), pp.391–6.

Brand, M.D. & Nicholls, D.G., 2011. Assessing mitochondrial dysfunction in cells. *The Biochemical journal*, 435(2), pp.297–312.

Breckwoldt, M.O. et al., 2014. Multiparametric optical analysis of mitochondrial redox signals during neuronal physiology and pathology in vivo. *Nature medicine*, 20(5), pp.555–60.

Brickley, K. & Stephenson, F.A., 2011. Trafficking kinesin protein (TRAK)-mediated transport of mitochondria in axons of hippocampal neurons. *The Journal of*

biological chemistry, 286(20), pp.18079–92.

Brookes, P.S., Bolaños, J.P. & Heales, S.J., 1999. The assumption that nitric oxide inhibits mitochondrial ATP synthesis is correct. *FEBS letters*, 446(2–3), pp.261–3.

Bros, H. et al., 2015. Assessing Mitochondrial Movement Within Neurons: Manual Versus Automated Tracking Methods. *Traffic*, pp.1–12.

Buch, T. et al., 2005. A Cre-inducible diphtheria toxin receptor mediates cell lineage ablation after toxin administration. *Nature methods*, 2(6), pp.419–26.

Burté, F. et al., 2014. Disturbed mitochondrial dynamics and neurodegenerative disorders. *Nature Reviews Neurology*, 11(1), pp.11–24.

Cai, Q. et al., 2012. Spatial parkin translocation and degradation of damaged mitochondria via mitophagy in live cortical neurons. *Current biology : CB*, 22(6), pp.545–52.

Cai, Q., Gerwin, C. & Sheng, Z.-H., 2005. Syntabulin-mediated anterograde transport of mitochondria along neuronal processes. *The Journal of cell biology*, 170(6), pp.959–69.

Calvo, S. et al., 2006. Systematic identification of human mitochondrial disease genes through integrative genomics. *Nature genetics*, 38(5), pp.576–82.

Campbell, G.R. et al., 2012. Mitochondrial changes within axons in multiple sclerosis: an update. *Current opinion in neurology*, 25(3), pp.221–30.

Campbell, G.R. et al., 2011. Mitochondrial DNA deletions and neurodegeneration in multiple sclerosis. *Annals of neurology*, 69(3), pp.481–92.

Campbell, G.R. & Mahad, D.J., 2011. Mitochondria as crucial players in demyelinated axons: lessons from neuropathology and experimental demyelination. *Autoimmune diseases*, 2011, p.262847.

Caroni, P., 1997. Overexpression of growth-associated proteins in the neurons of adult transgenic mice. *Journal of neuroscience methods*, 71(1), pp.3–9.

Carter, D. & Lisney, S., 1987. The numbers of unmyelinated and myelinated axons in normal and regenerated rat saphenous nerves. *Journal of the Neurological Sciences*, 80(2–3), pp.163–171.

Chacon, E. et al., 1994. Distribution of electrical potential, pH, free Ca2+, and volume inside cultured adult rabbit cardiac myocytes during chemical hypoxia: a multiparameter digitized confocal microscopic study. *Biophysical journal*, 66(4), pp.942–52.

Chan, G. et al., 2012. Quantitative morphometry of perifoveal capillary networks in the human retina. *Investigative ophthalmology & visual science*, 53(9), pp.5502–14.

Chang, J.C. et al., 2012. Single molecule analysis of serotonin transporter regulation using antagonist-conjugated quantum dots reveals restricted, p38 MAPK-dependent mobilization underlying uptake activation. *The Journal of neuroscience : the official journal of the Society for Neuroscience*, 32(26), pp.8919–29.

Che, D.L., Chowdary, P.D. & Cui, B., 2016. A close look at axonal transport: Cargos slow down when crossing stationary organelles. *Neuroscience Letters*, 610, pp.110–116.

Chen, H. et al., 2003. Mitofusins Mfn1 and Mfn2 coordinately regulate mitochondrial fusion and are essential for embryonic development. *The Journal of cell biology*, 160(2), pp.189–200.

Chen, T.W. et al., 2013. Ultrasensitive fluorescent proteins for imaging neuronal activity. *Nature*, 499(7458), pp.295–300.

Chen, Y. & Sheng, Z.-H., 2013. Kinesin-1-syntaphilin coupling mediates activity-dependent regulation of axonal mitochondrial transport. *The Journal of cell biology*, 202(2), pp.351–64.

Chenouard, N. et al., 2010. Curvelet analysis of kymograph for tracking bi-directional particles in fluorescence microscopy images. *Proceedings - International Conference on Image Processing, ICIP*, 126(Pt 1), pp.3657–3660.

Chenouard, N. et al., 2014. Objective comparison of particle tracking methods. *Nature methods*, 11(3), pp.281–290.

Chetta, J. & Shah, S.B., 2011. A novel algorithm to generate kymographs from dynamic axons for the quantitative analysis of axonal transport. *Journal of neuroscience methods*, 199(2), pp.230–40.

Chinnery, P.F. & Hudson, G., 2013. Mitochondrial genetics. *British medical bulletin*, 106, pp.135–59.

Chinopoulos, C. et al., 2009. A novel kinetic assay of mitochondrial ATP-ADP exchange rate mediated by the ANT. *Biophysical journal*, 96(6), pp.2490–504.

Chinopoulos, C. et al., 2010. Forward operation of adenine nucleotide translocase during F0F1-ATPase reversal: critical role of matrix substrate-level phosphorylation. *FASEB journal : official publication of the Federation of American Societies for Experimental Biology*, 24(7), pp.2405–16.

Chinopoulos, C., 2011. Mitochondrial consumption of cytosolic ATP: not so fast. *FEBS letters*, 585(9), pp.1255–9.

Chisholm, K. et al., 2016. Mitochondrial Function and Dynamics Imaged In Vivo. In K. A. Reeve et al., eds. *Mitochondrial Dysfunction in Neurodegenerative Disorders*. Cham: Springer International Publishing, pp. 329–345.

Cho, K. et al., 2007. Association of the kinesin-binding domain of RanBP2 to KIF5B and KIF5C determines mitochondria localization and function. *Traffic (Copenhagen, Denmark)*, 8(12), pp.1722–35.

Chomiak, T. & Hu, B., 2009. What is the optimal value of the g-ratio for myelinated fibers in the rat CNS? A theoretical approach. *PloS one*, 4(11), p.e7754.

Christensen, P.C. et al., 2016. Functional ionotropic glutamate receptors on peripheral axons and myelin. *Muscle and Nerve*, 54(3), pp.451–459.

Clegg, J.S., 1984. Properties and metabolism of the aqueous cytoplasm and its

boundaries. *The American journal of physiology*, 246(2 Pt 2), pp.R133-51.

Coleman, M., 2005. Axon degeneration mechanisms: commonality amid diversity. *Nature reviews. Neuroscience*, 6(11), pp.889–98.

Craner, M.J. et al., 2003. Abnormal sodium channel distribution in optic nerve axons in a model of inflammatory demyelination. *Brain : a journal of neurology*, 126(Pt 7), pp.1552–1561.

Craner, M.J. et al., 2004. Co-localization of sodium channel Nav1.6 and the sodium-calcium exchanger at sites of axonal injury in the spinal cord in EAE. *Brain : a journal of neurology*, 127(Pt 2), pp.294–303.

Cross, a H. et al., 1998. Peroxynitrite formation within the central nervous system in active multiple sclerosis. *Journal of neuroimmunology*, 88(1–2), pp.45–56.

Davie, C.A. et al., 1995. Persistent functional deficit in multiple sclerosis and autosomal dominant cerebellar ataxia is associated with axon loss. *Brain : a journal of neurology*, 118 (Pt 6, pp.1583–92.

Davies, A.L. et al., 2013. Neurological deficits caused by tissue hypoxia in neuroinflammatory disease. *Annals of Neurology*, 74(6), pp.815–825.

Davies, A.L. et al., 2013. Neurological deficits caused by tissue hypoxia in neuroinflammatory disease. *Annals of neurology*, 74(6), pp.815–25.

Davis, C. -h. O. et al., 2014. Transcellular degradation of axonal mitochondria. *Proceedings of the National Academy of Sciences*, 111(26), pp.9633–9638.

Debanne, D. et al., 2011. Axon physiology. *Physiological reviews*, 91(2), pp.555–602.

Deluca, H.F. & Engstrom, G.W., 1961. Calcium uptake by rat kidney mitochondria. *Proceedings of the National Academy of Sciences of the United States of America*, 47, pp.1744–50.

Desjardins, P., Frost, E. & Morais, R., 1985. Ethidium bromide-induced loss of mitochondrial DNA from primary chicken embryo fibroblasts. *Molecular and cellular*

biology, 5(5), pp.1163–9.

Diaz, G. et al., 2000. Homogeneous longitudinal profiles and synchronous fluctuations of mitochondrial transmembrane potential. *FEBS Letters*, 475(3), pp.218–224.

Direnberger, S. et al., 2012. Biocompatibility of a genetically encoded calcium indicator in a transgenic mouse model. *Nature Communications*, 3, p.1031.

Direnberger, S., 2011. *Investigating Expression , Function and Biocompatibility of the Genetically Encoded Calcium Indicator Tn-Xxl in Transgenic Mice*. Ludwig-Maximilians-Universität München.

Dorman, J.P., 2008. The effect of clustering on statistical tests: an illustration using classroom environment data. *Educational Psychology*, 28(5), pp.583–595.

Elson, J.L. et al., 2001. Random intracellular drift explains the clonal expansion of mitochondrial DNA mutations with age. *American journal of human genetics*, 68(3), pp.802–6.

Erecińska, M. et al., 1993. Relations between intracellular ions and energy metabolism under acidotic conditions: a study with nigericin in synaptosomes, neurons, and C6 glioma cells. *Journal of neurochemistry*, 61(4), pp.1356–68.

Erecińska, M. & Dagani, F., 1990. Relationships between the neuronal sodium/potassium pump and energy metabolism. Effects of K+, Na+, and adenosine triphosphate in isolated brain synaptosomes. *The Journal of general physiology*, 95(4), pp.591–616.

Ernster, L. & Schatz, G., 1981. Mitochondria: a historical review. *The Journal of cell biology*, 91(3 Pt 2), p.227s–255s.

Faisal, a A. & Laughlin, S.B., 2007. Stochastic simulations on the reliability of action potential propagation in thin axons. *PLoS computational biology*, 3(5), p.e79.

Felts, P. a, Baker, T. a & Smith, K.J., 1997. Conduction in segmentally demyelinated mammalian central axons. *The Journal of neuroscience : the official journal of the Society for Neuroscience*, 17(19), pp.7267–77.

Felts, P. a & Smith, K.J., 1996. Changes in the distribution of a calcium-dependent ATPase during demyelination and remyelination in the central nervous system. *Journal of neurocytology*, 25(3), pp.171–80.

Feng, G. et al., 2000. Imaging Neuronal Subsets in Transgenic Mice Expressing Multiple Spectral Variants of GFP. *Neuron*, 28(1), pp.41–51.

Field, A., Miles, J. & Field, Z., 2012. *Discovering Statistics Using R*, SAGE Publications.

Figge, M.T. et al., 2012. Deceleration of fusion-fission cycles improves mitochondrial quality control during aging. *PLoS computational biology*, 8(6), p.e1002576.

Fink, C., Morgan, F. & Loew, L.M., 1998. Intracellular fluorescent probe concentrations by confocal microscopy. *Biophysical journal*, 75(4), pp.1648–58.

Fledrich, R., Stassart, R.M. & Sereda, M.W., 2012. Murine therapeutic models for Charcot-Marie-Tooth (CMT) disease. *British medical bulletin*, 102(1), pp.89–113.

Fluegge, D. et al., 2012. Mitochondrial Ca2+ mobilization is a key element in olfactory signaling. *Nature Neuroscience*, 15(5), pp.754–762.

Frostick, S.P., Yin, Q. & Kemp, G.J., 1998. Schwann cells, neurotrophic factors, and peripheral nerve regeneration. *Microsurgery*, 18(7), pp.397–405.

Fujita, T. et al., 2007. Axonal guidance protein FEZ1 associates with tubulin and kinesin motor protein to transport mitochondria in neurites of NGF-stimulated PC12 cells. *Biochemical and biophysical research communications*, 361(3), pp.605–10.

Fukui, H. & Moraes, C.T., 2009. Mechanisms of formation and accumulation of mitochondrial DNA deletions in aging neurons. *Human molecular genetics*, 18(6), pp.1028–36.

Fukumitsu, K. et al., 2016. Mitochondrial fission protein Drp1 regulates mitochondrial transport and dendritic arborization in cerebellar Purkinje cells. *Molecular and Cellular Neuroscience*, 71, pp.56–65.

Garbern, J.Y. et al., 2002. Patients lacking the major CNS myelin protein, proteolipid

protein 1, develop length-dependent axonal degeneration in the absence of demyelination and inflammation. *Brain : a journal of neurology*, 125(Pt 3), pp.551–61.

Geiger, A. et al., 2012. Correlating calcium binding, Förster resonance energy transfer, and conformational change in the biosensor TN-XXL. *Biophysical journal*, 102(10), pp.2401–10.

George, E.B., Glass, J.D. & Griffin, J.W., 1995. Axotomy-induced axonal degeneration is mediated by calcium influx through ion-specific channels. *The Journal of neuroscience : the official journal of the Society for Neuroscience*, 15(October), pp.6445–6452.

Gerencser, A. a et al., 2012. Quantitative measurement of mitochondrial membrane potential in cultured cells: calcium-induced de- and hyperpolarization of neuronal mitochondria. *The Journal of physiology*, 590(Pt 12), pp.2845–71.

Glancy, B. & Balaban, R.S., 2012. Role of mitochondrial Ca2+ in the regulation of cellular energetics. *Biochemistry*, 51(14), pp.2959–73.

Gomes, L.C., Di Benedetto, G. & Scorrano, L., 2011. During autophagy mitochondria elongate, are spared from degradation and sustain cell viability. *Nature cell biology*, 13(5), pp.589–98.

Gonzalez, S. et al., 2015. In vivo time-lapse imaging of mitochondria in healthy and diseased peripheral myelin sheath. *Mitochondrion*, 23, pp.32–41.

Gregson, N. a & Hall, S.M., 1973. A quantitative analysis of the effects of the intraneural injection of lysophosphatidyl choline. *Journal of cell science*, 13(1), pp.257–77.

de Grey, A.D.N.J.N.J., 2009. How is mutant mitochondrial DNA clonally amplified? Much new evidence, still no answers. *Rejuvenation research*, 12(3), pp.217–9.

Grienberger, C. & Konnerth, A., 2012. Imaging calcium in neurons. *Neuron*, 73(5), pp.862–85.

Griffin, J.W. et al., 1990. Schwann cell proliferation following lysolecithin-induced demyelination. *Journal of neurocytology*, 19(3), pp.367–84.

Griffiths, I. et al., 1998. Axonal Swellings and Degeneration in Mice Lacking the Major Proteolipid of Myelin. *Science*, 280(5369), pp.1610–1613.

Haghnia, M. et al., 2007. Dynactin is required for coordinated bidirectional motility, but not for dynein membrane attachment. *Molecular biology of the cell*, 18(6), pp.2081–9.

Halestrap, A.P., Woodfield, K.Y. & Connern, C.P., 1997. Oxidative stress, thiol reagents, and membrane potential modulate the mitochondrial permeability transition by affecting nucleotide binding to the adenine nucleotide translocase. *The Journal of biological chemistry*, 272(6), pp.3346–54.

Hall, S.M., 1973. Some aspects of remyelination after demyelination produced by the intraneural injection of lysophosphatidyl choline. *Journal of cell science*, 13(2), pp.461–77.

Hall, S.M. & Gregson, N. a, 1971. The in vivo and ultrastructural effects of injection of lysophosphatidyl choline into myelinated peripheral nerve fibres of the adult mouse. *Journal of cell science*, 9(3), pp.769–89.

Haney, C.R. et al., 2008. Immobilization Using Dental Material Casts Facilitates Accurate Serial and Multimodality Small Animal Imaging. *Concepts in magnetic resonance. Part B, Magnetic resonance engineering*, 33B(2), pp.138–144.

Harris, J.J. & Attwell, D., 2012. The Energetics of CNS White Matter. *The Journal of Neuroscience*, 32(1), pp.356–371.

Hartline, D.K. & Colman, D.R., 2007. Rapid Conduction and the Evolution of Giant Axons and Myelinated Fibers. *Current Biology*, 17(1), pp.29–35.

Hasan, M.T. et al., 2004. Functional fluorescent Ca2+ indicator proteins in transgenic mice under TET control. *PLoS biology*, 2(6), p.e163.

Hatefi, Y. et al., 1962. Studies on the electron transfer system. XLII. Reconstitution of the electron transfer system. *The Journal of biological chemistry*, 237, pp.2661–9.

Haworth, R.A. & Hunter, D.R., 1979. The Ca2+-induced membrane transition in mitochondria. II. Nature of the Ca2+ trigger site. *Archives of biochemistry and biophysics*, 195(2), pp.460–7.

Hayashi, J. et al., 1990. Effects of ethidium bromide treatment of mouse cells on expression and assembly of nuclear-coded subunits of complexes involved in the oxidative phosphorylation. *Biochemical and biophysical research communications*, 167(1), pp.216–21.

Helmchen, F., 2011. Calibration of fluorescent calcium indicators. *Cold Spring Harbor protocols*, 2011(8), pp.923–30.

Hogan, V. et al., 2009. Increase in mitochondrial density within axons and supporting cells in response to demyelination in the Plp1 mouse model. *Journal of neuroscience research*, 87(2), pp.452–9.

Hogeboom, G.H., Schneider, W.C. & Pallade, G.E., 1948. Cytochemical studies of mammalian tissues; isolation of intact mitochondria from rat liver; some biochemical properties of mitochondria and submicroscopic particulate material. *The Journal of biological chemistry*, 172(2), pp.619–35.

Hoitzing, H., Johnston, I.G. & Jones, N.S., 2015. What is the function of mitochondrial networks? A theoretical assessment of hypotheses and proposal for future research. *BioEssays*, 37(6), pp.687–700.

Hom, J. et al., 2012. Regulation of mitochondrial fission by intracellular Ca2+ in rat ventricular myocytes. *Biochimica et biophysica acta*, 1797(6–7), pp.913–21.

Hom, J.R. et al., 2007. Thapsigargin induces biphasic fragmentation of mitochondria through calcium-mediated mitochondrial fission and apoptosis. *Journal of cellular physiology*, 212(2), pp.498–508.

van Horssen, J., Witte, M.E. & Ciccarelli, O., 2012. The role of mitochondria in axonal

degeneration and tissue repair in MS. *Multiple sclerosis (Houndmills, Basingstoke, England)*, 18(8), pp.1058–67.

Howarth, C., Gleeson, P. & Attwell, D., 2012. Updated energy budgets for neural computation in the neocortex and cerebellum. *Journal of cerebral blood flow and metabolism : official journal of the International Society of Cerebral Blood Flow and Metabolism*, 32(7), pp.1222–32.

Huang, T.-J., Verkhratsky, A. & Fernyhough, P., 2005. Insulin enhances mitochondrial inner membrane potential and increases ATP levels through phosphoinositide 3-kinase in adult sensory neurons. *Molecular and cellular neurosciences*, 28(1), pp.42–54.

Hughes, D.W. et al., 1982. Binding of myelin basic protein to phospholipid micelles. *The Journal of biological chemistry*, 257(9), pp.4698–700.

Hunter, D.R. & Haworth, R.A., 1979. The Ca2+-induced membrane transition in mitochondria. III. Transitional Ca2+ release. *Archives of biochemistry and biophysics*, 195(2), pp.468–77.

Imamura, H. et al., 2009. Visualization of ATP levels inside single living cells with fluorescence resonance energy transfer-based genetically encoded indicators. *Proceedings of the National Academy of Sciences of the United States of America*, 106(37), pp.15651–6.

Irvine, K.-A. & Blakemore, W.F., 2006. Age increases axon loss associated with primary demyelination in cuprizone-induced demyelination in C57BL/6 mice. *Journal of neuroimmunology*, 175(1–2), pp.69–76.

Irvine, K.A. & Blakemore, W.F., 2008. Remyelination protects axons from demyelination-associated axon degeneration. *Brain*, 131(6), pp.1464–1477.

Itoh, H. et al., 2004. Mechanically driven ATP synthesis by F1-ATPase. *Nature*, 427(6973), pp.465–8.

Jackson, V.M. et al., 2001. Characterization of action potential-evoked calcium transients

in mouse postganglionic sympathetic axon bundles. *Journal of Physiology*, 537(1), pp.3–16.

Janakaloti Narayanareddy, B.R. et al., 2014. A biophysical analysis of mitochondrial movement: differences between transport in neuronal cell bodies versus processes. *Traffic (Copenhagen, Denmark)*.

Jaqaman, K. et al., 2011. Cytoskeletal control of CD36 diffusion promotes its receptor and signaling function. *Cell*, 146(4), pp.593–606.

Jaqaman, K. et al., 2008. Robust single-particle tracking in live-cell time-lapse sequences. *Nature methods*, 5(8), pp.695–702.

Jaqaman, K. & Danuser, G., 2009. Computational image analysis of cellular dynamics: a case study based on particle tracking. *Cold Spring Harbor protocols*, 2009(12), p.pdb.top65.

Jares-Erijman, E. a & Jovin, T.M., 2003. FRET imaging. *Nature biotechnology*, 21(11), pp.1387–1395.

Jean, I. et al., 2002. Axonal lesions and PDGF-enhanced remyelination in the rat corpus callosum after lysolecithin demyelination. *Neuroreport*, 13(5), pp.627–31.

Jendrach, M. et al., 2005. Morpho-dynamic changes of mitochondria during ageing of human endothelial cells. *Mechanisms of Ageing and Development*, 126, pp.813–821.

Jing, Q. et al., 2000. Lysophosphatidylcholine activates p38 and p42/44 mitogen-activated protein kinases in monocytic THP-1 cells, but only p38 activation is involved in its stimulated chemotaxis. *Circulation research*, 87(1), pp.52–9.

Jones, D.P., 1986. Intracellular diffusion gradients of O2 and ATP. *The American journal of physiology*, 250(5 Pt 1), pp.C663-75.

Joshi, D.C. et al., 2015. Deletion of Mitochondrial Anchoring Protects Dysmyelinating Shiverer: Implications for Progressive MS. *Journal of Neuroscience*, 35(13), pp.5293–5306.

Jung, H., Yoon, B.C. & Holt, C.E., 2012. Axonal mRNA localization and local protein synthesis in nervous system assembly, maintenance and repair. *Nature reviews. Neuroscience*, 13(5), pp.308–24.

Kang, J.-S. et al., 2008. Docking of axonal mitochondria by syntaphilin controls their mobility and affects short-term facilitation. *Cell*, 132(1), pp.137–48.

Kaplan, B.B. et al., 2009. Axonal protein synthesis and the regulation of local mitochondrial function. *Results and problems in cell differentiation*, 48, pp.225–42.

Kapoor, R. et al., 2003. Blockers of sodium and calcium entry protect axons from nitric oxide-mediated degeneration. *Annals of neurology*, 53(2), pp.174–80.

Kapoor, R., Li, Y.G. & Smith, K.J., 1997. Slow sodium-dependent potential oscillations contribute to ectopic firing in mammalian demyelinated axons. *Brain*, 120(4), pp.647–652.

Kawamata, H. et al., 2010. A kinetic assay of mitochondrial ADP–ATP exchange rate in permeabilized cells. *Analytical Biochemistry*, 407(1), pp.52–57.

Kazak, L., Reyes, A. & Holt, I.J., 2012. Minimizing the damage: repair pathways keep mitochondrial DNA intact. *Nature reviews. Molecular cell biology*, 13(10), pp.659–71.

Keilin, D. & King, T.E., 1958. Reconstitution of the succinic oxidase system from soluble succinic dehydrogenase and a particulate cytochrome system preparation. *Nature*, 181(4622), pp.1520–2.

Kennedy, E.P. & Lehninger, A.L., 1949. Oxidation of fatty acids and tricarboxylic acid cycle intermediates by isolated rat liver mitochondria. *The Journal of biological chemistry*, 179(2), pp.957–72.

Kiryu-Seo, S. et al., 2010. Demyelination increases axonal stationary mitochondrial size and the speed of axonal mitochondrial transport. *The Journal of neuroscience : the official journal of the Society for Neuroscience*, 30(19), pp.6658–66.

Klausberger, T. et al., 2003. Brain-state- and cell-type-specific firing of hippocampal interneurons in vivo. *Nature*, 421(February), pp.844–848.

Kornek, B. et al., 2001. Distribution of a calcium channel subunit in dystrophic axons in multiple sclerosis and experimental autoimmune encephalomyelitis. *Brain : a journal of neurology*, 124(Pt 6), pp.1114–24.

Kornek, B. et al., 2000. Multiple Sclerosis and Chronic Autoimmune Encephalomyelitis. *The American Journal of Pathology*, 157(1), pp.267–276.

Koutsopoulos, O.S. et al., 2010. Human Miltons associate with mitochondria and induce microtubule-dependent remodeling of mitochondrial networks. *Biochimica et Biophysica Acta - Molecular Cell Research*, 1803(5), pp.564–574.

Krajewski, K.M. et al., 2000. Neurological dysfunction and axonal degeneration in Charcot-Marie-Tooth disease type 1A. *Brain : a journal of neurology*, 123 (Pt 7, pp.1516–27.

Kreft, I.G.G. & de Leeuw, J., 1998. *Introducing Multilevel Modeling*, Sage Publications (CA).

Krishnan, K.J. et al., 2008. What causes mitochondrial DNA deletions in human cells? *Nature genetics*, 40(3), pp.275–9.

Krzywinski, M., Altman, N. & Blainey, P., 2014. Points of Significance: Nested designs. *Nature Methods*, 11(10), pp.977–978.

Kuypers, N.J. et al., 2013. Functional consequences of ethidium bromide demyelination of the mouse ventral spinal cord. *Experimental neurology*, 247, pp.615–22.

Lassmann, H. & van Horssen, J., 2011. The molecular basis of neurodegeneration in multiple sclerosis. *FEBS letters*, 585(23), pp.3715–23.

Lassmann, H., van Horssen, J. & Mahad, D., 2012. Progressive multiple sclerosis: pathology and pathogenesis. *Nature reviews. Neurology.*

Lee, D. et al., 2007. Target cell-specific involvement of presynaptic mitochondria in post-

tetanic potentiation at hippocampal mossy fiber synapses. *The Journal of neuroscience : the official journal of the Society for Neuroscience*, 27(50), pp.13603–13.

Lee, S. et al., 2012. Mitofusin 2 is necessary for striatal axonal projections of midbrain dopamine neurons. *Human Molecular Genetics*, 21(22), pp.4827–4835.

Lefcheck, J.S., 2015. piecewiseSEM: Piecewise structural equation modeling in R for ecology, evolution, and systematics. *Methods in Ecology and Evolution*, pp.573–579.

Legros, F. et al., 2002. Mitochondrial fusion in human cells is efficient, requires the inner membrane potential, and is mediated by mitofusins. *Molecular biology of the cell*, 13(12), pp.4343–54.

Lehning, E.J. et al., 1996. Mechanisms of injury-induced calcium entry into peripheral nerve myelinated axons: role of reverse sodium-calcium exchange. *Journal of neurochemistry*, 66(2), pp.493–500.

Leibowitz, R.D., 1971. The effect of ethidium bromide on mitochondrial DNA synthesis and mitochondrial DNA structure in HeLa cells. *The Journal of cell biology*, 51(1), pp.116–22.

Lewis, T.L. et al., 2016. Progressive Decrease of Mitochondrial Motility during Maturation of Cortical Axons In Vitro and In Vivo. *Current biology : CB*, 26(19), pp.2602–2608.

Leyssens, a et al., 1996. The relationship between mitochondrial state, ATP hydrolysis, [Mg2+]i and [Ca2+]i studied in isolated rat cardiomyocytes. *The Journal of physiology*, 496 (Pt 1, pp.111–128.

Li, Z. et al., 2004. The importance of dendritic mitochondria in the morphogenesis and plasticity of spines and synapses. *Cell*, 119(6), pp.873–87.

Liesa, M. & Shirihai, O.S., 2013. Mitochondrial dynamics in the regulation of nutrient utilization and energy expenditure. *Cell metabolism*, 17(4), pp.491–506.

Liu, T.Y. et al., 2015. Cis and trans interactions between atlastin molecules during membrane fusion. *Proceedings of the National Academy of Sciences of the United States of America*, 112(15), pp.E1851-60.

Liu, X. et al., 2009. Mitochondrial "kiss-and-run": interplay between mitochondrial motility and fusion-fission dynamics. *The EMBO journal*, 28(20), pp.3074–3089.

Livet, J. et al., 2007. Transgenic strategies for combinatorial expression of fluorescent proteins in the nervous system. *Nature*, 450(7166), pp.56–62.

Llorente-Folch, I. et al., 2015. The regulation of neuronal mitochondrial metabolism by calcium. *J Physiol The Journal of Physiology Neuroscience S J Physiol*, 59316(59316), pp.3447–3462.

Locatelli, G. et al., 2012. Primary oligodendrocyte death does not elicit anti-CNS immunity. *Nature neuroscience*, 15(4), pp.543–50.

Logan, M., 2010. *Biostatistical Design and Analysis Using R: A Practical Guide*, Wiley.

Lovas, J.R. & Wang, X., 2013. The meaning of mitochondrial movement to a neuron's life. *Biochimica et biophysica acta*, 1833(1), pp.184–94.

Low, P.A. et al., 1983. Structural specificity in demyelination induced by lysophospholipids. *Biochimica et biophysica acta*, 754(3), pp.298–304.

Luchtman, D. et al., 2016. In vivo and in vitro effects of multiple sclerosis immunomodulatory therapeutics on glutamatergic excitotoxicity. *Journal of Neurochemistry*, 136(5), pp.971–980.

Ma, H. & O'Farrell, P.H., 2015. Selections that isolate recombinant mitochondrial genomes in animals. *eLife*, 4(AUGUST2015), pp.1–16.

Macaskill, A.F. et al., 2009. Miro1 is a calcium sensor for glutamate receptor-dependent localization of mitochondria at synapses. *Neuron*, 61(4), pp.541–55.

MacAskill, A.F. et al., 2009. GTPase dependent recruitment of Grif-1 by Miro1 regulates mitochondrial trafficking in hippocampal neurons. *Molecular and cellular*

neurosciences, 40(3), pp.301–12.

MacAskill, A.F., Atkin, T. a & Kittler, J.T., 2010. Mitochondrial trafficking and the provision of energy and calcium buffering at excitatory synapses. *The European journal of neuroscience*, 32(2), pp.231–40.

Malka, F. et al., 2005. Separate fusion of outer and inner mitochondrial membranes. *EMBO reports*, 6(9), pp.853–9.

Mank, M. et al., 2008. A genetically encoded calcium indicator for chronic in vivo two-photon imaging. *Nature methods*, 5(9), pp.805–811.

Manrique-Hoyos, N. et al., 2012. Late motor decline after accomplished remyelination: impact for progressive multiple sclerosis. *Annals of neurology*, 71(2), pp.227–44.

Mar, F.M. et al., 2014. CNS axons globally increase axonal transport after peripheral conditioning. *The Journal of neuroscience : the official journal of the Society for Neuroscience*, 34(17), pp.5965–70.

Maravall, M. et al., 2000. Estimating intracellular calcium concentrations and buffering without wavelength ratioing. *Biophysical journal*, 78(5), pp.2655–67.

Martin, L.J. et al., 2011. The mitochondrial permeability transition pore regulates nitric oxide-mediated apoptosis of neurons induced by target deprivation. *The Journal of neuroscience : the official journal of the Society for Neuroscience*, 31(1), pp.359–70.

Masaike, T. et al., 2008. Cooperative three-step motions in catalytic subunits of F(1)-ATPase correlate with 80 degrees and 40 degrees substep rotations. *Nature structural & molecular biology*, 15(12), pp.1326–33.

Matsushima, G.K. & Morell, P., 2001. The neurotoxicant, cuprizone, as a model to study demyelination and remyelination in the central nervous system. *Brain pathology (Zurich, Switzerland)*, 11(1), pp.107–16.

Milde, S. et al., 2015. Axonal transport declines with age in two distinct phases separated by a period of relative stability. *Neurobiology of Aging*, 36(2), pp.971–981.

Miller, K.E. & Sheetz, M.P., 2004. Axonal mitochondrial transport and potential are correlated. *Journal of cell science*, 117(Pt 13), pp.2791–804.

Mironov, S.L., 2007. ADP regulates movements of mitochondria in neurons. *Biophysical journal*, 92(8), pp.2944–52.

Misgeld, T. et al., 2007. Imaging axonal transport of mitochondria in vivo. *Nature methods*, 4(7), pp.559–61.

Misko, A. et al., 2010. Mitofusin 2 is necessary for transport of axonal mitochondria and interacts with the Miro/Milton complex. *The Journal of neuroscience : the official journal of the Society for Neuroscience*, 30(12), pp.4232–40.

Molden, S., Moldestad, O. & Storm, J.F., 2013. Estimating extracellular spike waveforms from CA1 pyramidal cells with multichannel electrodes. *PloS one*, 8(12), p.e82141.

Moldestad, O. et al., 2009. Tracheotomy improves experiment success rate in mice during urethane anesthesia and stereotaxic surgery. *Journal of neuroscience methods*, 176(2), pp.57–62.

Monsma, P.C. & Brown, A., 2012. FluoroMyelin™ Red is a bright, photostable and non-toxic fluorescent stain for live imaging of myelin. *Journal of neuroscience methods*, 209(2), pp.344–50.

Mórotz, G.M. et al., 2012. Amyotrophic lateral sclerosis-associated mutant VAPBP56S perturbs calcium homeostasis to disrupt axonal transport of mitochondria. *Human molecular genetics*, 21(9), pp.1979–88.

Mouli, P.K., Twig, G. & Shirihai, O.S., 2009. Frequency and selectivity of mitochondrial fusion are key to its quality maintenance function. *Biophysical journal*, 96(9), pp.3509–18.

Mukherjee, A. et al., 2011. Automated kymograph analysis for profiling axonal transport of secretory granules. *Medical image analysis*, 15(3), pp.354–67.

Murinson, B.B. & Griffin, J.W., 2004. C-fiber structure varies with location in peripheral

nerve. *Journal of neuropathology and experimental neurology*, 63(3), pp.246–254.

Murphy, M.P., 2009. How mitochondria produce reactive oxygen species. *The Biochemical journal*, 417(1), pp.1–13.

Mutsaers, S.E. & Carroll, W.M., 1998. Focal accumulation of intra-axonal mitochondria in demyelination of the cat optic nerve. *Acta neuropathologica*, 96(2), pp.139–43.

Nakagawa, S. & Schielzeth, H., 2013. A general and simple method for obtaining R 2 from generalized linear mixed-effects models R. B. O'Hara, ed. *Methods in Ecology and Evolution*, 4(2), pp.133–142.

Nakagawa, T. et al., 2005. Cyclophilin D-dependent mitochondrial permeability transition regulates some necrotic but not apoptotic cell death. *Nature*, 434(7033), pp.652–8.

Narayanareddy, B.R.J. et al., 2014. A biophysical analysis of mitochondrial movement: differences between transport in neuronal cell bodies versus processes. *Traffic (Copenhagen, Denmark)*, 15(7), pp.762–71.

Nave, K.-A., 2010. Myelination and the trophic support of long axons. *Nature reviews. Neuroscience*, 11(4), pp.275–83.

Neishabouri, A. & Faisal, a A., 2014. Axonal noise as a source of synaptic variability. *PLoS computational biology*, 10(5), p.e1003615.

Neufeld-Cohen, A. et al., 2016. Circadian control of oscillations in mitochondrial rate-limiting enzymes and nutrient utilization by PERIOD proteins. *Proceedings of the National Academy of Sciences of the United States of America*, 113(12), pp.E1673-82.

Nicholls, D.G., 2012. Fluorescence measurement of mitochondrial membrane potential changes in cultured cells. C. M. Palmeira & A. J. Moreno, eds. *Methods in molecular biology (Clifton, N.J.)*, 810, pp.119–33.

Nicholls, D.G., 2005. Mitochondria and calcium signaling. *Cell calcium*, 38(3–4), pp.311–

7.

Nicholls, D.G., 2006. Simultaneous monitoring of ionophore- and inhibitor-mediated plasma and mitochondrial membrane potential changes in cultured neurons. *The Journal of biological chemistry*, 281(21), pp.14864–74.

Nicholls, D.G. & Ferguson, S., 2013. *Bioenergetics, 4th Edition*, Elsevier Science.

Nicholls, D.G. & Ward, M.W., 2000. Mitochondrial membrane potential and neuronal glutamate excitotoxicity: mortality and millivolts. *Trends in neurosciences*, 23(4), pp.166–74.

Niesner, R., Siffrin, V. & Zipp, F., 2013. Two-photon imaging of immune cells in neural tissue. *Cold Spring Harbor protocols*, 2013(3).

Nikić, I. et al., 2011. A reversible form of axon damage in experimental autoimmune encephalomyelitis and multiple sclerosis. *Nature medicine*, 17(4), pp.495–9.

Novakovic, S.D. et al., 1996. Clusters of axonal Na+ channels adjacent to remyelinating Schwann cells. *Journal of neurocytology*, 25(6), pp.403–12.

O'Reilly, C.M. et al., 2003. Quantitative analysis of spontaneous mitochondrial depolarizations. *Biophysical journal*, 85(5), pp.3350–7.

Obashi, K. & Okabe, S., 2013. Regulation of mitochondrial dynamics and distribution by synapse position and neuronal activity in the axon. *The European journal of neuroscience*, 38(3), pp.2350–63.

Ohno, N. et al., 2014. Mitochondrial immobilization mediated by syntaphilin facilitates survival of demyelinated axons. *Proceedings of the National Academy of Sciences of the United States of America*, pp.1–6.

Ohno, N. et al., 2011. Myelination and axonal electrical activity modulate the distribution and motility of mitochondria at CNS nodes of Ranvier. *The Journal of neuroscience : the official journal of the Society for Neuroscience*, 31(20), pp.7249–58.

Okuno, D., Iino, R. & Noji, H., 2011. Rotation and structure of FoF1-ATP synthase. *Journal of biochemistry*, 149(6), pp.655–64.

Ouardouz, M. et al., 2009. Glutamate receptors on myelinated spinal cord axons: I. GluR6 kainate receptors. *Annals of neurology*, 65(2), pp.151–9.

Pacher, P., Beckman, J.S. & Liaudet, L., 2007. Nitric oxide and peroxynitrite in health and disease. *Physiological reviews*, 87(1), pp.315–424.

Palty, R. et al., 2010. NCLX is an essential component of mitochondrial Na+/Ca2+ exchange. *Proceedings of the National Academy of Sciences of the United States of America*, 107(1), pp.436–41.

Pan, X. et al., 2013. The physiological role of mitochondrial calcium revealed by mice lacking the mitochondrial calcium uniporter. *Nature cell biology*, 15(12), pp.1464–72.

Pareyson, D., Scaioli, V. & Laurà, M., 2006. Clinical and electrophysiological aspects of Charcot-Marie-Tooth disease. *Neuromolecular medicine*, 8(1–2), pp.3–22.

Paul, G., Cardinale, J. & Sbalzarini, I.F., 2013. Coupling image restoration and segmentation: A generalized linear model/bregman perspective. *International Journal of Computer Vision*, 104(1), pp.69–93.

Payne, B. a I. et al., 2011. Mitochondrial aging is accelerated by anti-retroviral therapy through the clonal expansion of mtDNA mutations. *Nature genetics*, 43(8), pp.806–10.

Peek, C.B. et al., 2013. Circadian clock NAD+ cycle drives mitochondrial oxidative metabolism in mice. *Science (New York, N.Y.)*, 342(6158), p.1243417.

Pereira, A.J. & Maiato, H., 2010. Improved kymography tools and its applications to mitosis. *Methods (San Diego, Calif.)*, 51(2), pp.214–9.

Persson, A.-K. et al., 2013. Sodium channels contribute to degeneration of dorsal root ganglion neurites induced by mitochondrial dysfunction in an in vitro model of

axonal injury. *The Journal of neuroscience : the official journal of the Society for Neuroscience*, 33(49), pp.19250–61.

Petty, H.R., 2007. Fluorescence microscopy: established and emerging methods, experimental strategies, and applications in immunology. *Microscopy research and technique*, 70(8), pp.687–709.

Pilling, A.D. et al., 2006. Kinesin-1 and Dynein are the primary motors for fast transport of mitochondria in Drosophila motor axons. *Molecular biology of the cell*, 17(4), pp.2057–68.

Plebanek, M.P. et al., 2015. Nanoparticle Targeting and Cholesterol Flux Through Scavenger Receptor Type B-1 Inhibits Cellular Exosome Uptake. *Scientific reports*, 5, p.15724.

Preibisch, S. et al., 2010. Software for bead-based registration of selective plane illumination microscopy data. *Nature methods*, 7(6), pp.418–9.

Raine, C.S., Wiśniewski, H. & Prineas, J., 1969. An ultrastructural study of experimental demyelination and remyelination. II. Chronic experimental allergic encephalomyelitis in the peripheral nervous system. *Laboratory investigation; a journal of technical methods and pathology*, 21(4), pp.316–27.

Rangaraju, V., Calloway, N. & Ryan, T.A., 2014. Activity-driven local ATP synthesis is required for synaptic function. *Cell*, 156(4), pp.825–35.

Rasband, M.N. et al., 1998. Potassium channel distribution, clustering, and function in remyelinating rat axons. *The Journal of neuroscience : the official journal of the Society for Neuroscience*, 18(1), pp.36–47.

Redford, E.J., Kapoor, R. & Smith, K.J., 1997. Nitric oxide donors reversibly block axonal conduction: demyelinated axons are especially susceptible. *Brain : a journal of neurology*, 120 (Pt 1(12), pp.2149–57.

Redpath, C.J. et al., 2013. Mitochondrial hyperfusion during oxidative stress is coupled to a dysregulation in calcium handling within a C2C12 cell model. *PloS one*, 8(7),

p.e69165.

Reid, D.B., 1979. An algorithm for tracking multiple targets. *Automatic Control, IEEE Transactions on*, 24(6), pp.843–854.

Reuter, M. et al., 2014. BRCA2 diffuses as oligomeric clusters with RAD51 and changes mobility after DNA damage in live cells. *The Journal of cell biology*, 207(5), pp.599–613.

Rintoul, G.L. et al., 2006. Nitric oxide inhibits mitochondrial movement in forebrain neurons associated with disruption of mitochondrial membrane potential. *Journal of neurochemistry*, 97(3), pp.800–6.

Rizk, A. et al., 2014. Segmentation and quantification of subcellular structures in fluorescence microscopy images using Squassh. *Nature protocols*, 9(3), pp.586–96.

Rizzuto, R. et al., 2012. Mitochondria as sensors and regulators of calcium signalling. *Nature Reviews Molecular Cell Biology*, 13(9), pp.566–578.

Robinson, W.S., 1950. Ecological correlations and the behavior of individuals. *American Sociological Review*.

Rolfe, D.F. & Brown, G.C.C., 1997. Cellular energy utilization and molecular origin of standard metabolic rate in mammals. *Physiological Reviews*, 77(3), p.731.

Rolland, S.G. et al., 2013. Impaired complex IV activity in response to loss of LRPPRC function can be compensated by mitochondrial hyperfusion. *Proceedings of the National Academy of Sciences of the United States of America*, 110, pp.E2967-76.

Romanelli, E. et al., 2013. Cellular, subcellular and functional in vivo labeling of the spinal cord using vital dyes. *Nature protocols*, 8(3), pp.481–90.

Rondelez, Y. et al., 2005. Highly coupled ATP synthesis by F1-ATPase single molecules. *Nature*, 433(7027), pp.773–7.

Rudick, R.A. et al., 1999. Use of the brain parenchymal fraction to measure whole brain atrophy in relapsing-remitting MS. Multiple Sclerosis Collaborative Research Group.

Neurology, 53(8), pp.1698–704.

Rudolf, R. et al., 2004. In vivo monitoring of Ca(2+) uptake into mitochondria of mouse skeletal muscle during contraction. *The Journal of cell biology*, 166(4), pp.527–36.

Rugarli, E.I. & Langer, T., 2012. Mitochondrial quality control: a matter of life and death for neurons. *The EMBO journal*, 31(6), pp.1336–49.

Rushton, W.A.H., 1951. A theory of the effects of fibre size in medullated nerve. *The Journal of physiology*, 115(1), pp.101–22.

Sahai, H. & Ageel, M.I., 2012. *The Analysis of Variance: Fixed, Random and Mixed Models*, Birkh{ä}user Boston.

Sajic, M. et al., 2013. Impulse Conduction Increases Mitochondrial Transport in Adult Mammalian Peripheral Nerves In Vivo B. A. Barres, ed. *PLoS Biology*, 11(12), p.e1001754.

Saotome, M. et al., 2008. Bidirectional Ca2+-dependent control of mitochondrial dynamics by the Miro GTPase. *Proceedings of the National Academy of Sciences of the United States of America*, 105(52), pp.20728–33.

Saxton, W.M. & Hollenbeck, P.J., 2012. The axonal transport of mitochondria. *Journal of cell science*, 125(Pt 9), pp.2095–104.

Scaduto, R.C. & Grotyohann, L.W., 1999. Measurement of mitochondrial membrane potential using fluorescent rhodamine derivatives. *Biophysical journal*, 76(1 Pt 1), pp.469–477.

Schain, A.J., Hill, R. a & Grutzendler, J., 2014. Label-free in vivo imaging of myelinated axons in health and disease with spectral confocal reflectance microscopy. *Nature Medicine*, (April 2013), pp.1–8.

Schindelin, J. et al., 2012. Fiji: an open-source platform for biological-image analysis. *Nature methods*, 9(7), pp.676–82.

Scholz, A., 2002. Mechanisms of (local) anaesthetics on voltage-gated sodium and other

ion channels. *British journal of anaesthesia*, 89(1), pp.52–61.

Senning, E.N. & Gordon, S.E., 2015. Activity and Ca^{2+} regulate the mobility of TRPV1 channels in the plasma membrane of sensory neurons. *eLife*, 4, p.e03819.

Sheng, Z.-H., 2014. Mitochondrial trafficking and anchoring in neurons: New insight and implications. *The Journal of Cell Biology*, 204(7), pp.1087–1098.

Shrager, P., 1989. Sodium channels in single demyelinated mammalian axons. *Brain Research*, 483(1), pp.149–154.

Shutt, T. et al., 2012. The intracellular redox state is a core determinant of mitochondrial fusion. *EMBO reports*, 13(10), pp.909–15.

Siekevitz, P., 1957. Powerhouse of the Cell. *Scientific American*, 197(1), pp.131–144.

Siffrin, V. et al., 2015. FRET based ratiometric Ca2+ imaging to investigate immune-mediated neuronal and axonal damage processes in experimental autoimmune encephalomyelitis. *Journal of Neuroscience Methods*, pp.1–8.

Smit-Rigter, L. et al., 2016. Mitochondrial Dynamics in Visual Cortex Are Limited In Vivo and Not Affected by Axonal Structural Plasticity. *Current biology : CB*, 26(19), pp.2609–2616.

Smith, K.J., 1980. A sensitive method for the detection and quantification of conduction deficits in nerve. *Journal of the neurological sciences*, 48(2), pp.191–9.

Smith, K.J. et al., 2001. Electrically active axons degenerate when exposed to nitric oxide. *Annals of neurology*, 49(4), pp.470–6.

Smith, K.J., Blakemore, W.F. & McDonald, W.I., 1979. Central remyelination restores secure conduction. *Nature*, 280(5721), pp.395–6.

Smith, K.J., Bostock, H. & Hall, S.M., 1982. Saltatory conduction precedes remyelination in axons demyelinated with lysophosphatidyl choline. *Journal of the Neurological Sciences*, 54(1), pp.13–31.

Smith, K.J. & Hall, S.M., 1980. Nerve conduction during peripheral demyelination and remyelination. *Journal of the neurological sciences*, 48(2), pp.201–19.

Smith, K.J. & Hall, S.M., 1988. Peripheral demyelination and remyelination initiated by the calcium-selective ionophore ionomycin: in vivo observations. *Journal of the neurological sciences*, 83(1), pp.37–53.

Smith, K.J. & McDonald, W.I., 1980. Spontaneous and mechanically evoked activity due to central demyelinating lesion. *Nature*, 286(5769), pp.154–5.

Smith, R., 1982. 1H-nuclear magnetic resonance study of the association of the basic protein of central nervous system myelin with lysophosphatidylcholine. *Biophysical chemistry*, 16(4), pp.347–54.

Snijders, T.A.B. & Bosker, R.J., 2011. *Multilevel Analysis: An Introduction to Basic and Advanced Multilevel Modeling*, SAGE Publications.

Song, Z. et al., 2007. OPA1 processing controls mitochondrial fusion and is regulated by mRNA splicing, membrane potential, and Yme1L. *Journal of Cell Biology*, 178(5), pp.749–755.

Sorbara, C.D. et al., 2014. Pervasive axonal transport deficits in multiple sclerosis models. *Neuron*, 84(6), pp.1183–90.

van Spronsen, M. et al., 2013. TRAK/Milton motor-adaptor proteins steer mitochondrial trafficking to axons and dendrites. *Neuron*, 77(3), pp.485–502.

Starkov, A. a & Fiskum, G., 2003. Regulation of brain mitochondrial H 2 O 2 production by membrane potential and NAD(P)H redox state. *J. Neurochem*, 86, pp.1101–1107.

De Stefani, D. et al., 2011. A forty-kilodalton protein of the inner membrane is the mitochondrial calcium uniporter. *Nature*, 476(7360), pp.336–40.

De Stefano, N. et al., 1998. Axonal damage correlates with disability in patients with relapsing-remitting multiple sclerosis. Results of a longitudinal magnetic resonance

spectroscopy study. *Brain : a journal of neurology*, 121 (Pt 8, pp.1469–77.

Stirling, D.P. & Stys, P.K., 2010. Mechanisms of axonal injury: internodal nanocomplexes and calcium deregulation. *Trends in Molecular Medicine*, 16(4), pp.160–170.

Stucky, C.L. et al., 2002. GFR alpha2/neurturin signalling regulates noxious heat transduction in isolectin B4-binding mouse sensory neurons. *Journal of Physiology*, 545(1), pp.43–50.

Symersky, J. et al., 2012. Oligomycin frames a common drug-binding site in the ATP synthase. *Proceedings of the National Academy of Sciences of the United States of America*, 109(35), pp.13961–5.

Takihara, Y. et al., 2015. In vivo imaging of axonal transport of mitochondria in the diseased and aged mammalian CNS. *Proceedings of the National Academy of Sciences*, 112(33), pp.10515–10520.

Tam, Z.Y. et al., 2013. Mathematical modeling of the role of mitochondrial fusion and fission in mitochondrial DNA maintenance. *PloS one*, 8(10), p.e76230.

Tanaka, Y. et al., 1998. Targeted disruption of mouse conventional kinesin heavy chain, kif5B, results in abnormal perinuclear clustering of mitochondria. *Cell*, 93(7), pp.1147–58.

Tian, L. et al., 2009. Imaging neural activity in worms, flies and mice with improved GCaMP calcium indicators. *Nature methods*, 6(12), pp.875–81.

Tinel, H. et al., 1999. Active mitochondria surrounding the pancreatic acinar granule region prevent spreading of inositol trisphosphate-evoked local cytosolic Ca(2+) signals. *The EMBO journal*, 18(18), pp.4999–5008.

Tondera, D. et al., 2009. SLP-2 is required for stress-induced mitochondrial hyperfusion. *The EMBO journal*, 28(11), pp.1589–600.

Traka, M. et al., 2010. A genetic mouse model of adult-onset, pervasive central nervous system demyelination with robust remyelination. *Brain*, 133(10), pp.3017–3029.

Traka, M. et al., 2016. Oligodendrocyte death results in immune-mediated CNS demyelination. *Nature neuroscience*, 19(1), pp.65–74.

Trapp, B.D. et al., 1998. Axonal transection in the lesions of multiple sclerosis. *The New England journal of medicine*, 338(5), pp.278–85.

Trapp, B.D. & Nave, K.-A., 2008. Multiple sclerosis: an immune or neurodegenerative disorder? *Annual review of neuroscience*, 31, pp.247–69.

Trapp, B.D. & Stys, P.K., 2009. Virtual hypoxia and chronic necrosis of demyelinated axons in multiple sclerosis. *Lancet neurology*, 8(3), pp.280–91.

Twig, G. et al., 2008. Fission and selective fusion govern mitochondrial segregation and elimination by autophagy. *The EMBO journal*, 27(2), pp.433–446.

Twisk, J.W.R., 2006. *Applied Multilevel Analysis: A Practical Guide for Medical Researchers*, Cambridge University Press.

Vallat, J.-M., Mathis, S. & Funalot, B., 2013. The various Charcot-Marie-Tooth diseases. *Current opinion in neurology*, 26(5), pp.473–80.

Vasington, F.D. & Murphy, J. V, 1962. Ca ion uptake by rat kidney mitochondria and its dependence on respiration and phosphorylation. *The Journal of biological chemistry*, 237, pp.2670–7.

Vergo, S. et al., 2011. Acid-sensing ion channel 1 is involved in both axonal injury and demyelination in multiple sclerosis and its animal model. *Brain : a journal of neurology*, 134(Pt 2), pp.571–84.

De Vos, K.J. et al., 2007. Familial amyotrophic lateral sclerosis-linked SOD1 mutants perturb fast axonal transport to reduce axonal mitochondria content. *Human Molecular Genetics*, 16(22), pp.2720–2728.

Walker, J.E., 2012. The ATP synthase: The understood, the uncertain and the unknown. *Biochimica et Biophysica Acta (BBA) - Bioenergetics*, 1817, p.S1.

Wallace, V.C.J. et al., 2003. Focal lysolecithin-induced demyelination of peripheral

afferents results in neuropathic pain behavior that is attenuated by cannabinoids. *The Journal of neuroscience : the official journal of the Society for Neuroscience*, 23(8), pp.3221–33.

Wang, S. et al., 2012. Multi-patterned dynamics of mitochondrial fission and fusion in a living cell. *PloS one*, 7(5), p.e19879.

Wang, X. & Schwarz, T.L., 2009. The mechanism of Ca2+ -dependent regulation of kinesin-mediated mitochondrial motility. *Cell*, 136(1), pp.163–74.

Waxman, S.G., 2008. Mechanisms of disease: sodium channels and neuroprotection in multiple sclerosis-current status. *Nature clinical practice. Neurology*, 4(3), pp.159–69.

Waxman, S.G., Craner, M.J. & Black, J.A., 2004. Na + channel expression along axons in multiple sclerosis and its models. *Trends in Pharmacological Sciences*, 25(11), pp.584–591.

Wilkins, A. et al., 2003. Oligodendrocytes promote neuronal survival and axonal length by distinct intracellular mechanisms: a novel role for oligodendrocyte-derived glial cell line-derived neurotrophic factor. *The Journal of neuroscience : the official journal of the Society for Neuroscience*, 23(12), pp.4967–74.

Wilkins, A., Chandran, S. & Compston, A., 2001. A role for oligodendrocyte-derived IGF-1 in trophic support of cortical neurons. *Glia*, 36(1), pp.48–57.

Williams, G.S. et al., 2013. Mitochondrial calcium uptake. *Proc Natl Acad Sci U S A*, 110(26), pp.10479–10486.

Williams, P.R. et al., 2014. A recoverable state of axon injury persists for hours after spinal cord contusion in vivo. *Nature Communications*, 5, p.5683.

Witte, M.E. et al., 2013. Mitochondrial dysfunction contributes to neurodegeneration in multiple sclerosis. *Trends in molecular medicine*, pp.1–9.

Woodruff, R.H. & Franklin, R.J.M., 1999. Demyelination and remyelination of the caudal

cerebellar peduncle of adult rats following stereotaxic injections of lysolecithin, ethidium bromide, and complement/anti-galactocerebroside: a comparative study. *Glia*, 25(3), pp.216–28.

Wortman, J.C. et al., 2014. Axonal transport: how high microtubule density can compensate for boundary effects in small-caliber axons. *Biophysical journal*, 106(4), pp.813–23.

Wu, B., Chen, J. & Singer, R.H., 2014. Background free imaging of single mRNAs in live cells using split fluorescent proteins. *Scientific reports*, 4, p.3615.

Xu, Y., 2002. Sphingosylphosphorylcholine and lysophosphatidylcholine: G protein-coupled receptors and receptor-mediated signal transduction. *Biochimica et biophysica acta*, 1582(1–3), pp.81–8.

Yajima, K. & Suzuki, K., 1979. Ultrastructural changes of oligodendroglia and myelin sheaths induced by ethidium bromide. *Neuropathology and applied neurobiology*, 5(1), pp.49–62.

Yu, D.Y. et al., 2013. Retinal ganglion cells: Energetics, compartmentation, axonal transport, cytoskeletons and vulnerability. *Progress in Retinal and Eye Research*, 36, pp.217–246.

Zala, D. et al., 2013. Vesicular Glycolysis Provides On-Board Energy for Fast Axonal Transport. *Cell*, 152(3), pp.479–491.

Zambonin, J.L. et al., 2011. Increased mitochondrial content in remyelinated axons: implications for multiple sclerosis. *Brain : a journal of neurology*, 134(Pt 7), pp.1901–13.

Zhang et al., 2010. Activity-dependent regulation of mitochondrial motility by calcium and Na/K-ATPase at nodes of Ranvier of myelinated nerves. *The Journal of neuroscience : the official journal of the Society for Neuroscience*, 30(10), pp.3555–66.

Zhang, K. et al., 2011. Automated image analysis for tracking cargo transport in axons.

Microscopy research and technique, 74(7), pp.605–13.

Zhang, Z. & David, G., 2016. Stimulation-induced Ca(2+) influx at nodes of Ranvier in mouse peripheral motor axons. *The Journal of physiology*, 594(1), pp.39–57.

Zhao, C. et al., 2001. Charcot-Marie-Tooth disease type 2A caused by mutation in a microtubule motor KIF1Bbeta. *Cell*, 105(5), pp.587–97.

Zhou, B. et al., 2016. Facilitation of axon regeneration by enhancing mitochondrial transport and rescuing energy deficits. *Journal of Cell Biology*, 214(1), pp.103–119.